

AFWAL-TR-88-4062

ADA 197816

RESEARCH ON MECHANICAL PROPERTIES  
FOR ENGINE LIFE PREDICTION



M. KHOBAIB  
N. E. ASHBAUGH  
G. A. HARTMAN  
T. WEERASOORIYA  
D. C. MAXWELL  
R. C. GOODMAN

UNIVERSITY OF DAYTON  
RESEARCH INSTITUTE  
300 COLLEGE PARK DRIVE  
DAYTON, OHIO 45469

MAY 1988

FINAL REPORT FOR PERIOD COVERING AUGUST 1984 THROUGH SEPTEMBER 1987

APPROVED FOR PUBLIC RELEASE; DISTRIBUTION UNLIMITED

MATERIALS LABORATORY  
AIR FORCE WRIGHT AERONAUTICAL LABORATORIES  
AIR FORCE SYSTEMS COMMAND  
WRIGHT-PATTERSON AIR FORCE BASE, OHIO 45433-6533

BEST AVAILABLE COPY

20040225110

## NOTICE

When Government drawings, specifications, or other data are used for any purpose other than in connection with a definitely Government-related procurement, the United States Government incurs no responsibility or any obligation whatsoever. The fact that the Government may have formulated or in any way supplied the said drawings, specifications, or other data, is not to be regarded by implication, or otherwise in any manner construed, as licensing the holder, or any other person or corporation; or as conveying any rights or permission to manufacture, use, or sell any patented invention that may in any way be related thereto.

This report has been reviewed by the Office of Public Affairs (ASD/PA) and is releasable to the National Technical Information Service (NTIS). At NTIS, it will be available to the general public, including foreign nations.

This technical report has been reviewed and is approved for publication.

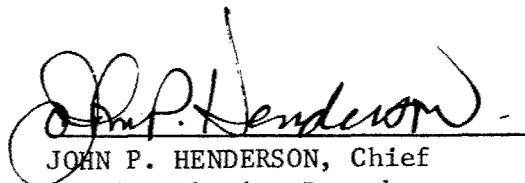


THEODORE NICHOLAS  
Metals Behavior Branch  
Metals and Ceramics Division



ALLAN W. GUNDERSON  
Metals Behavior Branch  
Metals and Ceramics Division

FOR THE COMMANDER



JOHN P. HENDERSON, Chief  
Metals Behavior Branch  
Metals and Ceramics Division

If your address has changed, if you wish to be removed from our mailing list, or if the addressee is no longer employed by your organization please notify AFWAL/MLLN, W-PAFB, OH 45433- 6533 to help us maintain a current mailing list.

Copies of this report should not be returned unless is required by security considerations, contractual obligations, or notice on a specific document.

Unclassified

SECURITY CLASSIFICATION OF THIS PAGE

## REPORT DOCUMENTATION PAGE

1a. REPORT SECURITY CLASSIFICATION Unclassified			1b. RESTRICTIVE MARKINGS	
2a. SECURITY CLASSIFICATION AUTHORITY			3. DISTRIBUTION/AVAILABILITY OF REPORT Approved for public release; distribution unlimited.	
2b. DECLASSIFICATION/DOWNGRADING SCHEDULE				
4. PERFORMING ORGANIZATION REPORT NUMBER(S) UDR-TR-88-08			5. MONITORING ORGANIZATION REPORT NUMBER(S) AFWAL-TR-88- 4062	
6a. NAME OF PERFORMING ORGANIZATION University of Dayton Research Institute		6b. OFFICE SYMBOL (If applicable)	7a. NAME OF MONITORING ORGANIZATION Materials Laboratory (AFWAL/MLLN) Air Force Wright Aeronautical Laboratories	
6c. ADDRESS (City, State and ZIP Code) 300 College Park Drive Dayton, Ohio 45469			7b. ADDRESS (City, State and ZIP Code) Wright-Patterson AFB, Ohio 45433-6533	
8a. NAME OF FUNDING/SPONSORING ORGANIZATION		8b. OFFICE SYMBOL (If applicable)	9. PROCUREMENT INSTRUMENT IDENTIFICATION NUMBER F33615-84-C-5051	
8c. ADDRESS (City, State and ZIP Code)			10. SOURCE OF FUNDING NOS.	
			PROGRAM ELEMENT NO.	PROJECT NO.
			61102F	2302
			TASK NO.	WORK UNIT NO.
			P1	18
11. TITLE (Include Security Classification) Research on Mechanical Properties for Engine Life Prediction				
12. PERSONAL AUTHOR(S) M. Khobaiib, N.E. Ashbaugh, G.A. Hartman, T. Weerasooriya, D.C. Maxwell, R.C. Goodman				
13a. TYPE OF REPORT Final		13b. TIME COVERED FROM 8/84 TO 09/87		14. DATE OF REPORT (Yr., Mo., Day) MAY 1988
				15. PAGE COUNT 120
16. SUPPLEMENTARY NOTATION				
17. COSATI CODES			18. SUBJECT TERMS (Continue on reverse if necessary and identify by block number)	
FIELD	GROUP	SUB. GR.		
11	06		Laser inteferometer system, compliance, fatigue crack	
01	03		closure, surface crack, fatigue crack growth,	
19. ABSTRACT (Continue on reverse if necessary and identify by block number)				
<p>Analytical and experimental investigations have been performed to determine crack growth behavior of turbine engine disk and blade alloys under various loading conditions typical of service environments. Tests were performed at elevated temperature in vacuum also to evaluate the baseline crack growth behavior. Substructural analysis of creep rupture specimens were conducted to understand the basic mechanism of time-dependent elevated temperature deformation. The work performed can be divided into three categories -- development of experimental techniques, material characterization techniques, and data maintenance and test support activities.</p> <p>The capability of the IDG laser system to monitor extended gage length was analyzed and found feasible. New grips and specimens have been designed and fabricated for high temperature composite testing. Enhancements to existing systems for crack length and displacement measurements were made. A number of computer automation applications are also discussed.</p>				
20. DISTRIBUTION/AVAILABILITY OF ABSTRACT UNCLASSIFIED/UNLIMITED <input checked="" type="checkbox"/> SAME AS RPT. <input type="checkbox"/> DTIC USERS <input type="checkbox"/>			21. ABSTRACT SECURITY CLASSIFICATION Unclassified	
22a. NAME OF RESPONSIBLE INDIVIDUAL Theodore Nicholas		22b. TELEPHONE NUMBER (Include Area Code) (513) 255-1347		22c. OFFICE SYMBOL AFWAL/MLLN

DD FORM 1473, 83 APR

EDITION OF 1 JAN 73 IS OBSOLETE.

Unclassified

SECURITY CLASSIFICATION OF THIS PAGE

BLOCK 18 (Concluded)

environmental interaction, notches, creep crack growth, creep rupture, stacking faults, hot corrosion, test automation, nickel-based superalloys, ceramic composites, single crystal material.

BLOCK 19 (Concluded)

Fatigue crack closure, fatigue and creep crack growth, and creep rupture and hot corrosion tests were conducted. The experimental techniques and results of these tests are presented.

## FOREWORD

The work described in this report was performed at the Metals Behavior Branch, Metals and Ceramics Division, Materials Laboratory, Air Force Wright Aeronautical Laboratories (AFWAL/MLLN) under Contract No. F33615-84-C-5051, "Research on Mechanical Properties for Engine Life Prediction." The contract was administered under the direction of AFWAL by Dr. Theodore Nicholas (MLLN). The program was conducted by the Structural Integrity Division, University of Dayton Research Institute, Dayton, Ohio with Dr. Noel E. Ashbaugh acting as the Principal Investigator.

The investigations were conducted by Drs. Noel E. Ashbaugh, M. Khobaib, Tusit Weerasooriya, A. M. Rajendran, and Messers. George Hartman, and Joseph Kroupa. Generation of the data was accomplished in part by Messers. Richard Goodman, David Maxwell, George Ahrens, David Johnson, William Goddard, Joey Cook, and Mrs. Susan Ramsey. Assistance in data reduction, computer programming, fabrication of fixtures, and assembling mechanical and electrical components was provided by Messers. Paul Enderle, Jeffrey Hanrahan, and Richard Kleismit, and Miss Patricia Bornhorst and Mrs. Mary Papp and Mrs. Jill Johnson. Miss Debbie Garner was responsible for the typing of this document. This work was conducted during the period 1 August 1984 to 30 September 1987.

# TABLE OF CONTENTS

<u>SECTION</u>		<u>PAGE</u>
1	INTRODUCTION	1
2	EXPERIMENTAL DEVELOPMENTS	2
2.1	MEASUREMENT TECHNIQUES	2
2.1.1	<u>Linear Array Laser Interferometer (LALI)</u>	2
2.1.2	<u>Extended Gage Length for the IDG Laser System</u>	2
2.1.3	<u>Back-Face Strain Compliance for SE(T) Specimen</u>	3
2.1.4	<u>DC Potential Application to TMF Crack Growth Testing</u>	3
2.1.5	<u>DC Potential for Creep Crack Length Determination</u>	4
2.1.6	<u>Specimen Illumination for Crack Length Measurement Above 1100°C</u>	4
2.1.7	<u>Ceramic Composite Testing</u>	5
2.1.7.1	Elevated Temperature Furnaces	6
2.1.7.1.1	1100-1200°C Furnaces	6
2.1.7.1.2	1650°C Furnace	7
2.1.7.2	High Temperature Grips	7
2.1.7.3	Four-Point Bend Fixture	8
2.1.8	<u>Crack Length Expression as a Function of Compliance for Middle Cracked Tension Specimen</u>	8
2.2	TEST SYSTEM AUTOMATION	13
2.2.1	<u>Development of IDG Short Crack Testing System</u>	14
2.2.2	<u>Automated Closure Load Determination</u>	18
2.2.3	<u>IBM AT System</u>	20
2.2.4	<u>Improvements to the C20 HCF/LCF System</u>	21

## TABLE OF CONTENTS (Continued)

<u>SECTION</u>		<u>PAGE</u>
	2.2.4.1 Software Development for the C20 Test Machine	21
	2.2.4.2 Hardware Improvements to the C20 System	22
	2.2.5 <u>C10 System Improvements</u>	25
	2.2.6 <u>Installation of VIC-20 on Major/Minor Test System</u>	25
	2.2.7 <u>IBM System CS9000 Installation on Vacuum Test System</u>	25
	2.2.8 <u>Software Enhancements</u>	26
	2.2.8.1 Software Enhancements on IBM System CS9000	26
	2.2.8.2 Software Enhancements for PC Test Control System	29
2.3	REPAIR AND IMPROVEMENT OF THE MAJOR/MINOR TEST SYSTEM	30
	2.3.1 <u>Armature Failure</u>	30
	2.3.2 <u>Water Cooling System</u>	30
	2.3.3 <u>Upgrading Control Equipment</u>	31
	2.3.4 <u>Computer Interface</u>	31
3	MATERIAL CHARACTERIZATION TESTS	32
3.1	CRACK CLOSURE	32
	3.1.1 <u>Effects of Load History and Specimen Geometry on Fatigue Crack Closure Measurements</u>	32
	3.1.2 <u>Effect of Closure on the Crack Growth of Surface Cracks in a High Strength Titanium Alloy</u>	33
	3.1.3 <u>Crack Closure Measurement Through Fractography</u>	34
3.2	FATIGUE CRACK GROWTH TESTING	38
	3.2.1 <u>TMF Baseline Testing</u>	38
	3.2.2 <u>HCF/LCF Initiation on IN718</u>	38

## TABLE OF CONTENTS (Continued)

<u>SECTION</u>		<u>PAGE</u>
3.2.3	<u>HCF/LCF Initiation in N4+</u>	39
3.2.4	<u>HCF/LCF Initiation in Hastalloy X</u>	39
3.2.5	<u>Fatigue Crack Growth Behavior of IN718</u>	40
3.2.6	<u>Fatigue Crack Growth at High Load Ratios in the Time-Dependent Regime</u>	42
3.2.7	<u>Variable R Tests at Constant <math>K_{max}</math> for Inconel 718</u>	43
3.2.8	<u>Modeling of IN718 Crack Growth Behavior</u>	45
3.2.9	<u>Threshold Evaluation of IN718</u>	48
3.2.10	<u>Effect of Overloads on Alloy IN718</u>	51
3.2.11	<u>Fracture Surface Analysis of IN718 Tested Under TMF Conditions</u>	51
3.2.12	<u>Surface Flaw/Short Crack in Ti Alloys</u>	52
3.2.13	<u>Crack Growth from Notches</u>	53
3.3	CRACK GROWTH BEHAVIOR OF SINGLE CRYSTALLINE MATERIAL	54
3.3.1	<u>Fatigue Crack Growth in Alloy N4</u>	58
3.3.2	<u>Fatigue Crack Growth of Alloy N4 in Vacuum</u>	59
3.3.3	<u>Creep Crack Growth (CCG) of Alloy N4 in Laboratory Air</u>	59
3.3.4	<u>Creep Crack Growth of Alloy N4 in Vacuum</u>	61
3.3.5	<u>Fracture Surface Analysis of Creep Crack Growth Specimens</u>	61
3.4	CREEP RUPTURE TESTS	68
3.4.1	<u>Creep Rupture Tests of Bare and Coated Alloy N4 in Air</u>	68
3.4.2	<u>Microstructure Evaluations of Creep Rupture in Single Crystalline Material</u>	68

## TABLE OF CONTENTS (Continued)

<u>SECTION</u>		<u>PAGE</u>
	3.4.3 <u>Creep Rupture Tests of Alloy N4</u>	68
	3.4.4 <u>Substructural Analysis of Creep Tested Specimens at 870°C</u>	69
	3.4.5 <u>Development of Substructure at 760°C, 870°C, 980°C, and 1093°C</u>	80
3.5	HOT CORROSION TESTS	85
	3.5.1 <u>Effect of Hot Corrosion on Creep Rupture Life of IN718</u>	85
	3.5.2 <u>Effect of Hot Corrosion on Creep Rupture Life of Rene' 77 and Rene' 80</u>	88
	3.5.3 <u>Effects of Stress and Stress History on Environmental Attack in Rene' 80</u>	88
	3.5.4 <u>Hot Corrosion in Alloy Rene' 77 and Rene' 80</u>	89
4	ANALYTICAL DEVELOPMENTS	91
	4.1 BACK-FACE STRAIN ON SE(T) GEOMETRY	91
	4.2 ANALYSIS OF DISK-SHAPED COMPACT SPECIMEN	91
	4.3 THREE DIMENSIONAL ANALYSIS OF CURVED CRACK FRONT	93
	4.4 VALIDATION OF BODNER-PARTOM ROUTINES IN SNAP	93
	4.5 COMPLIANCE EXPRESSIONS FOR C(T) SPECIMENS	96
5	DATA MAINTENANCE AND TEST SUPPORT ACTIVITIES	98
	5.1 DATA TRANSMISSION AND STORAGE	98
	5.2 MLLS BRANCH TEST SUPPORT ACTIVITIES	98
	5.3 ELECTRONICS FABRICATION AND REPAIR	99

## TABLE OF CONTENTS (Concluded)

<u>SECTION</u>	<u>PAGE</u>
APPENDIX A - IBM AT SYSTEM	100
REFERENCES	104

## LIST OF ILLUSTRATIONS

<u>FIGURE</u>		<u>PAGE</u>
2.1	High Temperature Grip.	9
2.2	Four-Point Bend Fixture.	10
2.3	Center-Cracked Tension Specimen, M(T).	12
2.4	Schematic Illustration of the Principle of Operation of the Interferometric Displacement Gage.	15
2.5	Schematic Illustration of the Computerized Interferometric System.	16
2.6	Typical Load vs Crack-Mouth-Opening-Displacement Data and Differential Data are Shown for a Small Surface Crack Where $2C \approx 50 \text{ } \mu\text{m}$ and $d_o \approx 50 \text{ } \mu\text{m}$ .	17
2.7	Plot of Load Versus Back-Face-Strain (BFS) Data and Closure Load Indication.	19
2.8	Self-Aligning Unit.	24
2.9	Combined Cyclic and Hold-Time Loadings Applied by Automated Control Software.	27
2.10	(a) Modified TF-34 Spectrum, and (b) Simple Overload Spectrum.	28
3.1	Load Sequence for Fractography Based on Crack Closure Evaluation.	35
3.2	Schematic of K-Profile for Closure Test.	36
3.3	Transmission Electron Microscope Photograph Taken from Replica of Fatigued Specimen (X25000).	37
3.4	HCF/LCF Specimen Configuration.	41
3.5	Three Modes of Fatigue Crack Growth Behavior Presented at a Function of (1-R).	44
3.6	$da/dN$ vs $1/T$ Plot at $K_{max} = 40 \text{ MPa}\sqrt{\text{m}}$ Showing the Change in Micro-Mechanism of Crack Growth with Changes in Frequency and Temperature.	46

# LIST OF ILLUSTRATIONS (Continued)

<u>FIGURE</u>		<u>PAGE</u>
3.7	da/dN vs 1/T Plot at $K_{max} = 27.8 \text{ MPa}\sqrt{\text{m}}$ Showing the Change in Micro-Mechanism of Crack Growth with Changes in Frequency and Temperature.	47
3.8	da/dN vs Crack Length Behavior of Cracks Growing from a Notch.	55
3.9	da/dN vs Delta K Behavior of Cracks Growing from a Notch (for Small Load of 3336N).	56
3.10	da/dN vs Delta K Behavior of Cracks Growing from a Notch (for High Load of 5133N).	57
3.11	Crack Layering: (a) Low Magnification Picture Showing Crack Layering Ahead of Crack Tip and (b) Higher Magnification of Crack.	60
3.12	Effect of Crystal Anisotropy on Creep Crack Growth.	62
3.13	Effect of Temperature on the Creep Crack Growth of Rene' N4 Alloy.	63
3.14	Interdendritic Failure.	65
3.15	Fracture Surface of Specimen Tested in Air, Showing Transition Zone.	66
3.16	Fracture Surface of Specimen Tested in Vacuum, Showing a Small Zone of Transdendritic Failure.	67
3.17	Fracture Surface of a Creep Rupture Specimen Showing Crack Initiation from Surface.	70
3.18	Fracture Surface of a Creep Rupture Specimen Showing Shrinkage Pores.	71
3.19	TEM Microstructure of Heat-Treated, Rene' N4 Single Crystal.	72

# LIST OF ILLUSTRATIONS (Continued)

<u>FIGURE</u>		<u>PAGE</u>
3.20	Substructure Developed at 0.15% Creep Strain at 870°C: (a) Tested at 870°C (X33000), and (b) Notice the Dislocation Surrounding Gamma Prime Precipitate (X66000).	73
3.21	Substructure Developed at 0.86% Creep Strain Tested at 870°C: (a) Stacking Faults with Precipitate (X50000), (b) Dislocation Network at the Interface (X50000), and (c) Dislocation Migration into Precipitate (X66000).	75
3.22	Substructure Developed at 2.5% Creep Strain Tested at 870°C: (a) High Density of Stack Fault (X33000), (b) Super Pair Entangled with Stacking Fault (66000), and (c) Precipitate Shear by Super Pair (X66000).	77
3.23	Substructure Developed at >10.0% Creep Strain Tested at 870°C (X66000).	79
3.24	Substructure Developed in the Creep Ruptured Specimen at 1400°F: (a) High Density of Faults and (b) Two Sets of Faults in the Precipitate.	81
3.25	Substructure Developed in Creep-Ruptured Specimen at 870°C: (a) Indication of Microtwin Formation from Stacking Faults, and (b) Two Sets of Intersecting Microtwins.	82
3.26	Substructure Developed in Creep Ruptured Specimen at 870°C: (a) Cell Structure, (b) Network of Super Pair Dislocation, and (c) Super Pair Dislocation in Precipitate.	83
3.27	Substructure Developed in Creep-Ruptured Specimen at 1093°C: (a) Cell Structure, (b) High Magnification of Cell Structure, (c) Cell Development Within Precipitate, and (d) $a/2 \langle 110 \rangle$ Super Pair in Cell Wall.	86

## LIST OF ILLUSTRATIONS (Concluded)

<u>FIGURE</u>		<u>PAGE</u>
4.1	Mesh for Finite Element Analysis of DC(T), a/W = 0.5, Specimen.	92
4.2	Finite Element Model of a Tensile Strip Specimen.	94
4.3	Loading Cycle.	94
4.4	Comparison Between the SNAP and the Direct Solutions for the Cyclic Loading Response.	97
A1	Block Diagram of the Automated Test Station.	101

# LIST OF TABLES

<u>TABLE</u>		<u>PAGE</u>
3.1	CONSTANTS AND INDIVIDUAL FUNCTIONS OF THE MODEL FOR EACH CRACK GROWTH REGION FOR A CONSTANT TEMPERATURE, T	49
3.2	TEMPERATURE-DEPENDENT FUNCTION FOR EACH CRACK GROWTH REGION	50
4.1	PARAMETERS FOR THE BODNER-PARTOM CONSTITUTIVE EQUATIONS (REFERENCE 25)	95

## SECTION 1

### INTRODUCTION

This program emphasized the experimental determination of advanced mechanical properties that characterize the crack growth behavior of typical turbine engine disk and blade alloys under a broad range of conditions representative of those encountered in service. The information, obtained under this program, will guide the development of life prediction methodologies which are based on the concept of damage tolerance as a design philosophy. The experimental investigations addressed materials and environments typical of those encountered in service and concentrated on those areas where current life prediction schemes were weakest or totally lacking. The emphasis was on providing experimental data and modeling the fundamental aspects of fatigue behavior in aircraft turbine engine alloys. Innovative ideas were used in the investigations to resolve both existing and anticipated material behavior problems.

The research effort was subdivided into five interrelated research tasks:

- Experimental Procedures and Test Developments
- Experimental Crack Growth Characteristics
- Mechanical Analysis and Parameter Evaluation
- Model Development and Data Analysis
- Basic Mechanical Properties.

These tasks formed an umbrella that covers many investigations which supported major advances in the development of models for life predictions of engine related component cracking problems. The following sections discuss work in progress and work completed on these tasks.

## SECTION 2

### EXPERIMENTAL DEVELOPMENTS

#### 2.1 MEASUREMENT TECHNIQUES

A number of measurement techniques related to material testing were improved or developed during the contract period. Most of these techniques were directed toward crack length determination under various environmental conditions. These techniques are strongly influenced by the accuracy and resolution requirements for the data.

##### 2.1.1 Linear Array Laser Interferometer (LALI)

An enhanced laser interferometer for small scale displacement measurements was developed. The system was modeled after an interferometric displacement measurement system developed by Sharpe [1] (see subsection 2.2.1). Sharpe subsequently used rotating mirrors to obtain displacement resolution on the order of 10 nanometers.

This new system replaced the rotating mirrors with solid state linear array image detectors; improved data acquisition speed was obtained through the use of a 32 bit microcomputer and dual channel high speed analog-to-digital convertors. The linear array system has approximately the same resolution as the rotating mirror system. The maximum displacement range is limited as a result of the data storage capacity to approximately 40 microns with a gage length of 50 to 400 microns.

##### 2.1.2 Extended Gage Length for the IDG Laser System

The short gage length (with maximum length approximately 0.4 mm) of the laser interferometer system is ideal for studying crack tip response and other small-scale localized phenomena. Additional applications for non-contact displacement measurement methods, however, require a longer gage length on the order of 10 mm. To accommodate these needs, a task was established to evaluate methods of extending the gage length in

stages to approximately 10.0 mm. The initial evaluations were successful on the optics bench and indicate that special optics and data reduction algorithms need to be developed.

#### **2.1.3 Back-Face Strain Compliance for SE(T) Specimen**

Nonvisual crack length determination for use in crack growth behavior studies can be accomplished with strain measurements on a single edge notched tension, SE(T), specimen. This method of crack length determination is also well suited for use with closed-loop computer-controlled test systems.

A finite element analysis was used to determine the theoretical back-face strain values for various crack length to width ratios from 0.2 to 0.8 and a mathematical relationship of crack length ratios versus back-face strain compliance was developed.

In several preliminary tests, the crack length ratios from 0.2 to 0.4 were calculated from strain compliance and compared to optically measured values. The compliance crack lengths agreed with the optically measured lengths to within  $\pm 0.002$  in. Additional tests provided good agreement at larger crack length ratios.

#### **2.1.4 DC Potential Application to TMF Crack Growth Testing**

A fully automated DC electric potential system for determining crack length under thermal/mechanical test conditions has been developed. H. H. Johnson's [2] formula was used to determine crack length from electric potential for the center crack geometry. The value of an unknown constant in the formula is determined so that the formula yields a crack length obtained from an alternate measurement method (typically optical) for the measured electric potential. The method has been found to provide excellent crack length data under nonisothermal conditions. Crack length measurements exhibited a scatterband of approximately 0.051 mm compared with 0.127 mm typical for optical measurements at elevated temperatures. Comparison of electric potential and optical crack lengths showed less than 0.254 mm

difference over the entire test. Most of the difference was attributed to crack tip tunneling which was not accounted for optically. To achieve good crack length resolution and low data scatter, precautions were taken to eliminate or minimize the errors in the potential measurement due to thermal effects.

#### **2.1.5 DC Potential for Creep Crack Length Determination**

A DC electric potential system was assembled so that crack lengths could be determined in specimens tested at elevated temperatures under constant load. The voltmeter in the system is accessed by a Tektronix 4051 microcomputer so that data can be acquired automatically. Several preliminary tests were conducted on middle cracked tensile M(T) specimens of alloy IN718 at 650°C to evaluate the capabilities of the system. The results were encouraging. Further tests will be conducted to evaluate the accuracy of theoretical calibration relationships between crack lengths and electric potential for M(T) and compact tension C(T) specimens.

#### **2.1.6 Specimen Illumination for Crack Length Measurement Above 1100°C**

A system was evaluated to determine the possibility of improving the visibility of cracks at temperatures above 1100°C (2000°F). The system consisted of a short wavelength monochromatic light source and a selective optical filter chosen to match the wavelength of the source. In this case, an argon laser and a fiber optic probe were used as a movable light source and a metallic coated optical filter with bandpass at 488 nanometers was used on the viewing microscope to eliminate all light at wavelengths other than the laser light. The short wavelength green argon laser was used because the standard HeNe laser light at 632 nanometers is close to the wavelength radiated by the hot specimen.

The system was verified on a creep frame at 1100°C using a cracked M(T) sample. Results from the laser were compared with results from standard equipment to determine the laser's effectiveness. Using the standard equipment, the crack

was nearly invisible; while under the filtered laser light, the crack tip could be seen easily. The laser system worked well under various loading conditions and appears to be a good way to view samples optically at temperatures above 1000°C (1800°F) or where standard techniques are inadequate. In the future, a simple monochromatic light source could be substituted for the laser, thus, reducing the system cost substantially.

#### **2.1.7 Ceramic Composite Testing**

A task was initiated to develop test techniques and equipment which can be used to study the behavior of ceramic composite materials at elevated temperature under nonisothermal conditions. Following are the three main interrelated areas of prime concern in developing the test capability.

1. Sample Gripping - The brittle and anisotropic nature of ceramic composites makes it difficult to design specimens and gripping fixtures which will produce a uniform stress field in the test specimen section. The use of both cool grips (where the grips are not in the furnace hot zone) and hot grips were considered.

2. Displacement Measurement - Because of their low ductility, ceramic composites are sensitive to stress discontinuities. Mechanical extensometers typically require attachments or introduce marks on the surface of the sample at the contact points which can produce premature failure. Specimen access for extensometry and small gage length must also be considered.

3. Sample Heating - Some of the proposed ceramic composite materials have usable strength at temperatures exceeding 1650°C (3000°F). A number of heating techniques are available to attain this temperature; however, very few can be adapted for use in the material-testing context. Specimen access for extensometry and gripping problems impose additional limitations. The details of the furnaces designed to operate at 1100-1650°C are described in paragraph 2.1.7.1.

Preliminary evaluations of gripping methods have led to the development of a flat plate friction grip and a specimen design which appear to meet the testing requirements. Approximately 12 tests have been performed at room temperature on a carbon-carbon composite with good results. Another high temperature grip was designed for use up to 1375°C (2500°F). The details are described later in paragraph 2.1.7.2.

Initially, conventional high-temperature extensometry will be used to measure displacement. As the temperature capability of the test system is increased, a laser interferometric technique will provide displacement measurement capability at temperatures beyond the current mechanical extensometry limits.

A heating system using infrared quartz lamps is being assembled for use in the tests. In this design, since the lamp output is highly directional, the heating energy can be directed at the specimen test section only; this allows the grips to be maintained at a lower temperature. The proposed system will have provisions for access to the specimen for extensometry.

#### **2.1.7.1 Elevated Temperature Furnaces**

With the requirement to test material at higher temperatures, three prototype furnaces were constructed. Two of them were constructed to achieve an operating temperature of 1100-1200°C while the third one was specially designed and fabricated to attain temperatures up to 1650°C in the hot zone.

##### **2.1.7.1.1 1100-1200°C Furnaces**

For simplicity, a previous furnace design was modified. The previous furnace provided operational temperature capability to about 875°C. The first prototype was constructed with a used shell from one of the earlier furnaces, which required no additional mechanical attachments for immediate use. The chief modification was to substitute 1200°C heating elements for the older 875°C elements. Highly efficient ceramic wool insulation was used in the earlier

design, so this was retained. Upon operation, it was noted that the outer skin temperature was approximately 250°C. To maintain 1100°C, the furnace operated on a 90 percent duty cycle.

The second prototype was constructed with a new shell of slightly larger dimensions than the previous design and used the maximum fixture space available in the test frame. A new insulation material which was reported to have much improved insulating properties was used in conjunction with the ceramic wool. Upon operation, the outer skin temperature was approximately 200°C, only a small improvement over the previous model. To maintain 1100°C, this furnace operated on an 80 percent duty cycle.

Wrapping the exterior with approximately 1.5 inches of fiberglass blanket reduced the heat loss significantly and one could easily touch the outer surface safely. While the extra blanket is cumbersome and not completely satisfactory, 1100-1200°C test temperatures can be achieved.

#### **2.1.7.1.2 1650°C Furnace**

This furnace was designed and fabricated to conduct mechanical tests on ceramic materials in air at temperatures up to 1650°C. The outer shell of an old 875°C furnace was used to construct this furnace. Silicon fiberboard was used as the insulating material and was laid inside of the shell to minimize any heat loss. Special silicon carbide rods 16 inches long and 1/2-inch diameter were used as the heating element. The furnace chamber has a heated zone of 3-1/2 inches x 5 inches x 5 inches and has been tested to achieve over 1650°C in the heated zone. The upper and lower holes for the pull rods have yet to be drilled. The design also has provisions for the side viewports.

#### **2.1.7.2 High Temperature Grips**

A special high temperature metallic grip has been designed for testing ceramic and metal matrix composite materials. The temperature capability of this grip is limited to

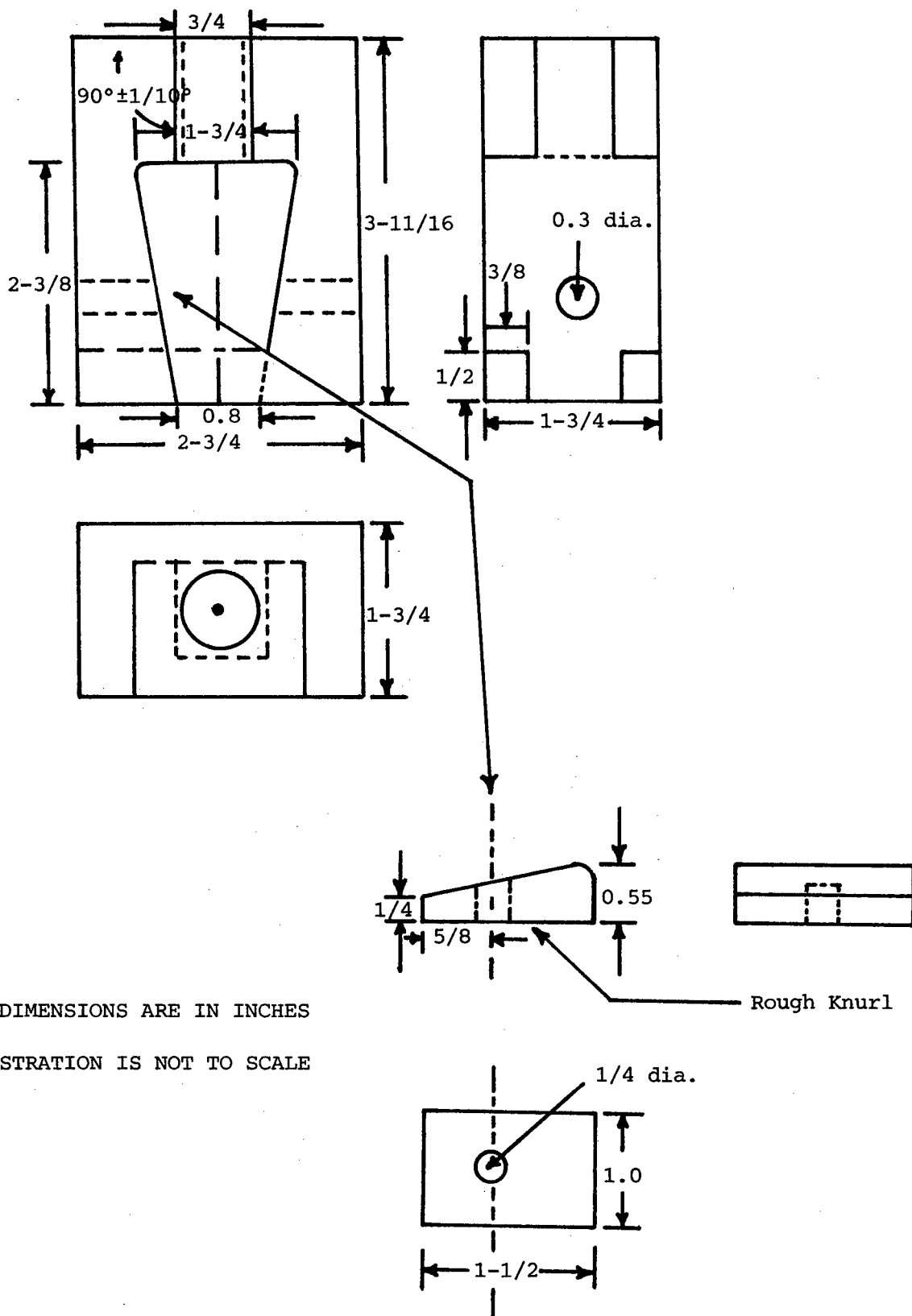
around 1100°C. In this approach, the temperature gradient in the specimen is completely eliminated by the use of high temperature grip material. The grip has been designed to be universally used for tensile, creep, and fatigue testing with flat specimens having pin holes on either side. Figure 2.1 shows a section of the grip. The design (of the grip) takes advantage of the wedge action as well as pin hole, thus minimizing any possible misalignment. Wider and thicker gage sections are permitted due to the use of tab ends as well as multi-grip action. The specimen grip assembly can be aligned at room temperature through the use of strain gages, and this alignment can be maintained during the heating and testing. Preliminary testing of this grip shows promise.

#### **2.1.7.3 Four-Point Bend Fixture**

Four-point bend test is the most commonly used testing technique for measuring the fracture toughness of ceramic materials. Although the toughness value obtained from this method is not as reliable as the values obtained from compact specimens for metallic materials, useful engineering information can be obtained from these tests. Various designs for four-point bend fixtures exist for toughness testing at room temperature, but these cannot be easily adapted for high temperature testing. A modification of a four-point bend fixture design [3] was accomplished to support fracture toughness testing of ceramic material at elevated temperature. The test fixture is fabricated out of SiC plate and the details are shown in Figure 2.2. We plan to use rectangular specimens with chevron notch. The specimen fixture assembly can be heated to the desired temperature in the specially designed furnace discussed in paragraph 2.1.7.2.

#### **2.1.8 Crack Length Expression as a Function of Compliance for Middle Cracked Tension Specimen**

The object of this investigation was to formulate a wide-range solution for crack length of a middle cracked tension specimen,  $M(T)$ , as a function of compliance, displacement



ALL DIMENSIONS ARE IN INCHES

ILLUSTRATION IS NOT TO SCALE

Figure 2.1. High Temperature Grip.



measurement location, and Poisson's ratio. A schematic showing the geometric parameters of an M(T) specimen is given in Figure 2.3. The total crack length is  $2a$  and the nominal distance between the locations for the displacement measurement is  $2y$ .  $W$  is the width of the specimen,  $B$  is the specimen thickness, and  $E$  is Young's modulus. The compliance,  $C$ , is the inverse of the slope of the linear portion of the load versus displacement curve.

The relationship of crack length in terms of the previous defined variables is given by,

$$2a/W = A_1X + A_2X^2 + A_3X^3 + A_4X^4 + A_5X^5 + A_6X^6, \quad (1)$$

where  $A_1 = 1.22350$ ,

$$A_2 = -0.699032,$$

$$A_3 = 3.25584,$$

$$A_4 = -6.65042,$$

$$A_5 = 5.54001,$$

$$A_6 = -1.66989,$$

$$\text{and } X = 1 = \exp \left[ \frac{-\sqrt{(EBC+2y/W)(EBC-2y/W)}}{2.141} \right] \quad (2)$$

A comparison of the results of the polynomial expression in equation (1) to available analytical results suggest that the validity of ranges of this expression are  $0 < 2a/W < 1$  and  $0 < 2y/W < 0.8$  for Poisson's ratio,  $\nu = 0.3$ .

To account for Poisson's ratio, the  $A_i$  coefficients in equation (1) are replaced with  $A'_i$  values,  $i = 1, \dots, 6$ , where

$$A'_1 = A_1 \sqrt{\frac{3.3}{3+\nu}},$$

$$A'_2 = A_2 + A_1 \left[ 1 - \sqrt{\frac{3.3}{3+\nu}} \right],$$

$$A'_3 = A_3, \quad A'_4 = A_4,$$

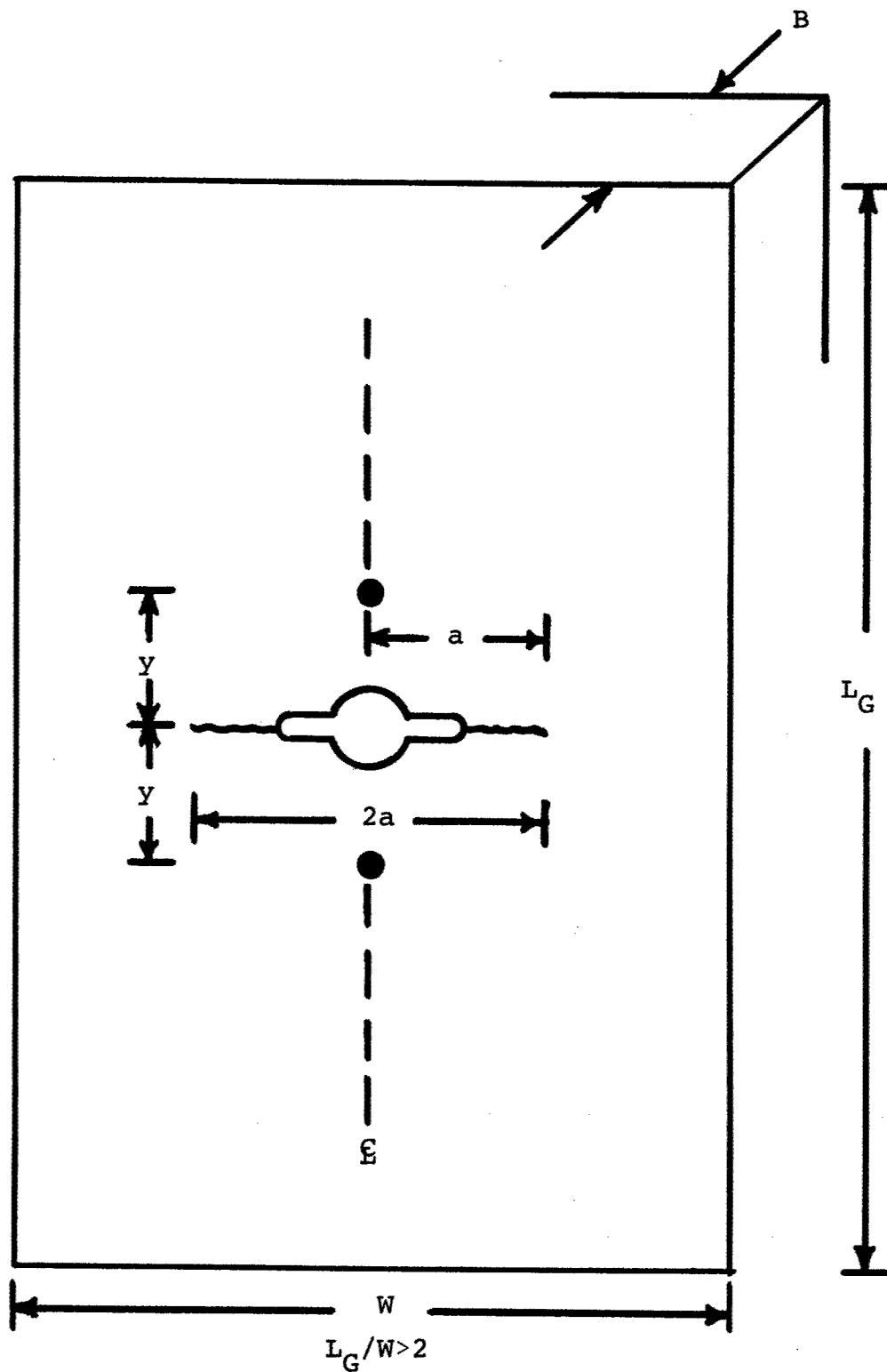


Figure 2.3. Center-Cracked Tension Specimen, M(T).

$$A_5 = A_5,$$

$$A_6 = A_6.$$

The details of the development of this equation is described in Reference 4.

## 2.2 TEST SYSTEM AUTOMATION

A number of test systems within the laboratory were automated. A hardware/software system was developed to determine the real-time numerical fringe position for the laser interferometric displacement gage (IDG) short crack testing system using a PDP 11/24 mini-computer. A new method was developed in conjunction with the automated test software in use on the IBM PC and System 9000 microcomputers to determine the closure load more accurately. Along with these new developments, significant improvements and modifications were made to various test systems to increase their efficiency. Several modifications were also made to the software of the PC test control systems which allowed improved tracking and storage of the load-displacement data.

The efforts in these areas are part of a continuing effort on the part of the University of Dayton Research Institute (UDRI) to maintain the AFWAL/MLLN laboratory at a state-of-the-art level. The Major/Minor (M/M) test system was equipped with a VIC-20 microcomputer to monitor the major and minor loads and high and low temperature interlocks and to interrupt the test when a system failure occurs. Various test and data reduction software were developed for the IBM 9000 microcomputer to aid different projects in the laboratory. The C20 HCF/LCF system was equipped with an IEEE-488 interface to allow the VIC-20 computer to address two HP multimeters and a Wavetek signal generator to increase the accuracy as well as the efficiency of the system.

### 2.2.1 Development of IDG Short Crack Testing System

The determination of short crack mouth opening displacement (CMOD) can be accomplished by using an unique laser interferometric displacement gage (IDG), originally developed by Sharpe et al. [1]. The method utilizes the coherent light of a HeNe laser to make precise measurements of CMOD by monitoring the movement of interference fringes that are formed by laser light impinging on two pyramid indents that are across the crack as shown in Figure 2.4. Movement of the indents is related to the movement of fringes that are formed in space. Counting the fringes that pass a fixed observation point produces relative displacement information for the indents.

Resolution of the system has been increased 100 times by monitoring the fractional movement of the fringes in space. This was accomplished by a system that is shown in Figure 2.5. The system employed servo-controlled rotating mirrors to sweep the fringe patterns across the stationary detectors. This facilitated monitoring the fringe pattern as a function of time.

A software/hardware system was developed to determine the real-time numerical fringe position using a PDP 11/24 mini-computer. The system produced real-time load versus displacement curves with a resolution of nine nanometers. A typical load displacement and differential displacement plot from the system is shown in Figure 2.6. This system has been used in studies of short crack growth, including surface cracks with lengths on the order of 40 nanometers. The system can be used to study the threshold condition as a function of the short crack lengths starting from the cracks with lengths equal to the grain size. The details of the system are described in Reference 5.

In addition to the IDG control software, software was developed to enhance the short crack growth control program on the PDP. The software performs the following tasks:

- Controls a programmable function generator.

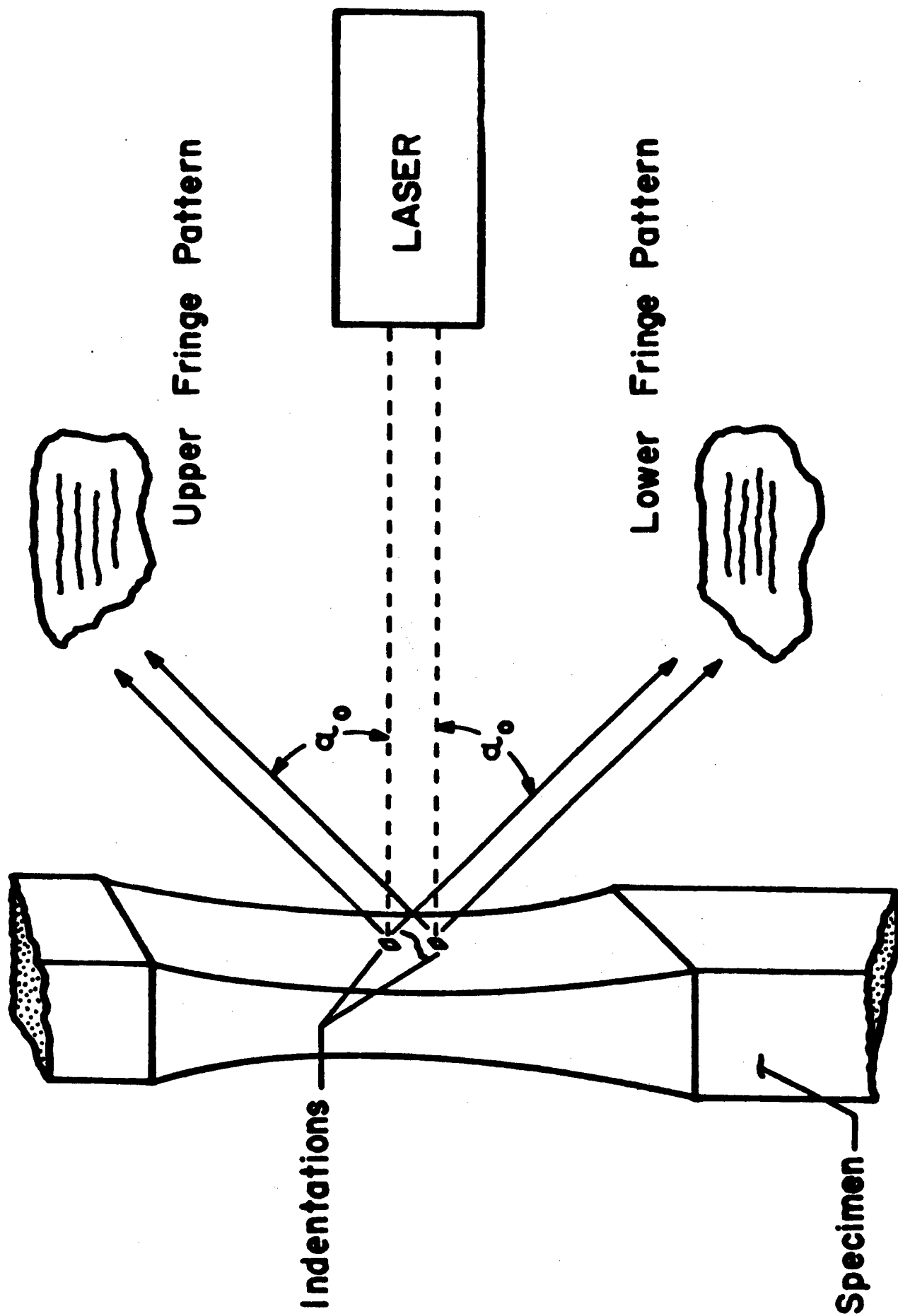


Figure 2.4. Schematic Illustration of the Principle of Operation of the Interferometric Displacement Gage.

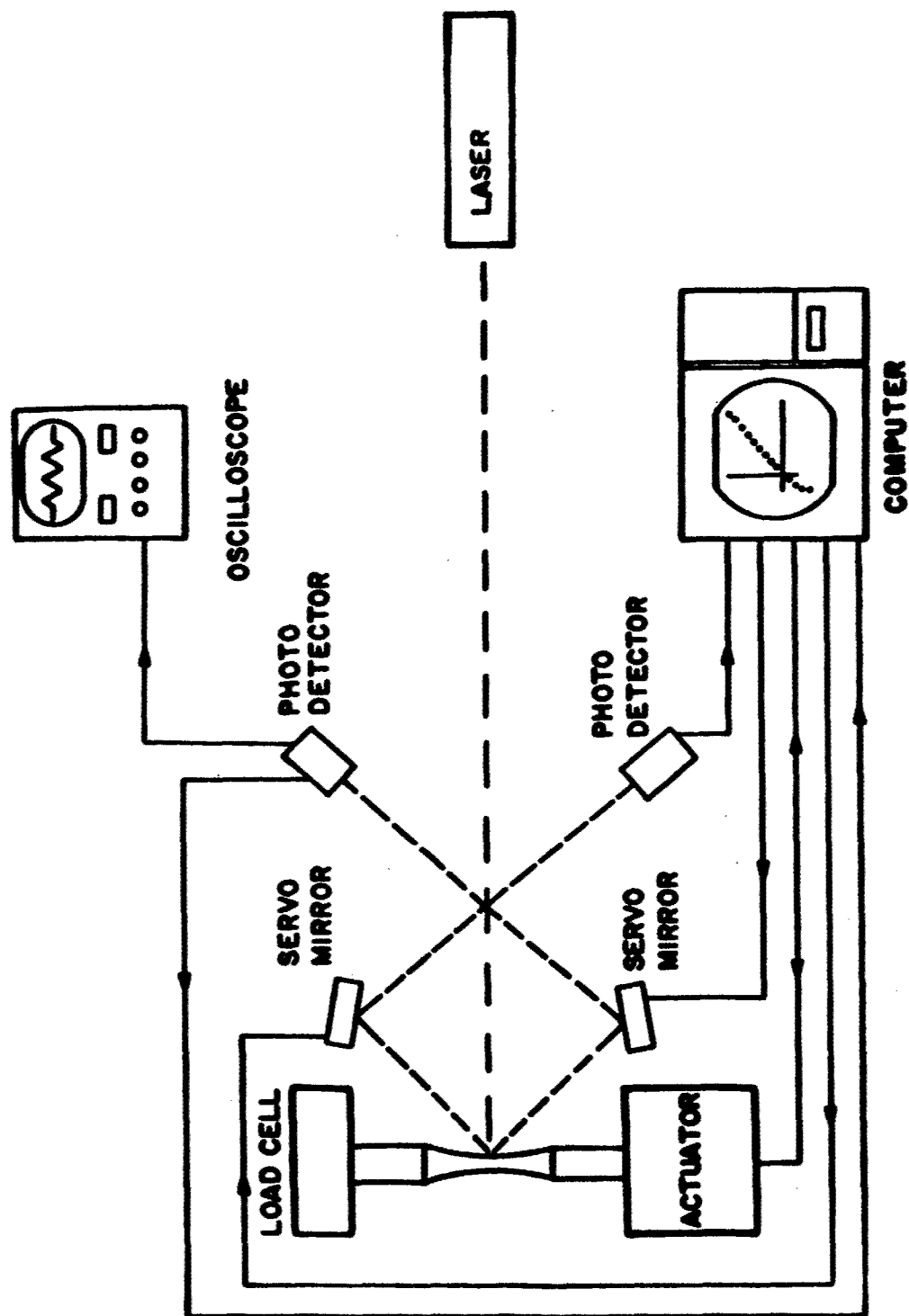


Figure 2.5. Schematic Illustration of the Computerized Interferometric System.

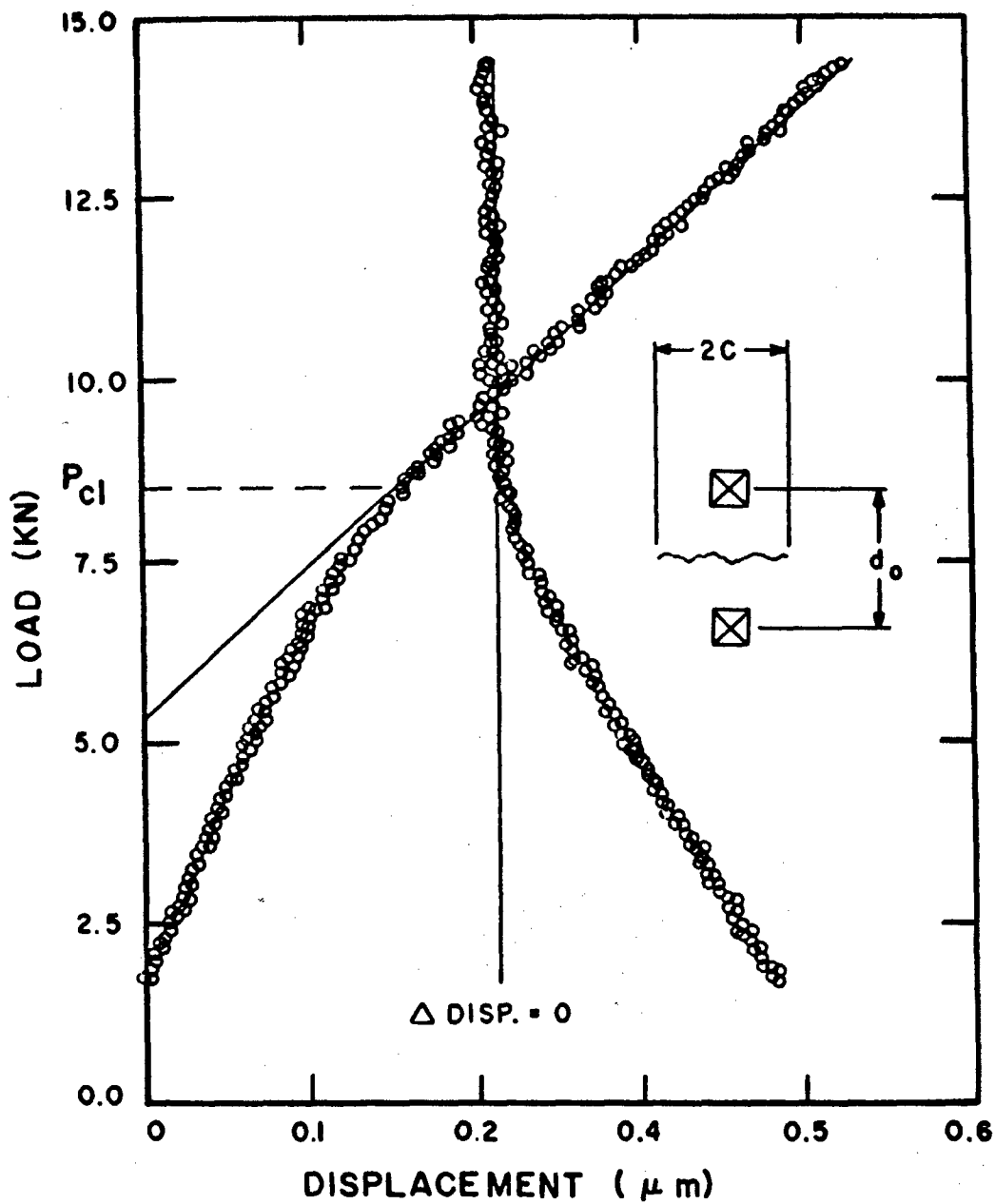


Figure 2.6. Typical Load vs Crack-Mouth-Opening-Displacement Data and Differential Data are Shown for a Small Surface Crack Where  $2C \approx 50 \mu\text{m}$  and  $d_o \approx 50 \mu\text{m}$ .

- Triggers the camera system for automatic surface photographs.
- Stops at selected load for optical viewing.
- Stops at a selected load to allow focusing of the camera/microscope system.
- Communicates with and synchronizes the IDG software with test control functions.

#### **2.2.2 Automated Closure Load Determination**

In the past, closure load has been determined from a manual examination of an autographically plotted load-displacement curve. The load level at which the displacement is estimated to deviate from the linear behavior of the curve is the closure load. A method has been developed to eliminate some subjectivity in the closure load determination. This method is sufficiently well-defined so that software can be developed to analyze digitally acquired load-displacement data.

As part of this technique for closure load determination, linear regression coefficients are computed for the subset of load-displacement data within a window that has been selected by the investigator. The standard deviation of this subset of data for the linear regression is calculated. The limits of an errorband about the regression line is selected as a multiple of the standard deviation. Then, starting with the minimum load, the data is analyzed at increasing load levels to determine the load at which the load-displacement data falls within the established errorband. By adjusting the errorband, the technique can produce unbiased closure load results for a broad range of data.

This technique has been implemented in the software for the IBM 9000 microcomputers in the laboratory. A plot of the output of the software is shown in Figure 2.7 for load versus back-face-strain (BFS) data from a C(T) specimen. In addition to a plot of the original load-BFS data, a second plot is also presented which represents the difference between the acquired

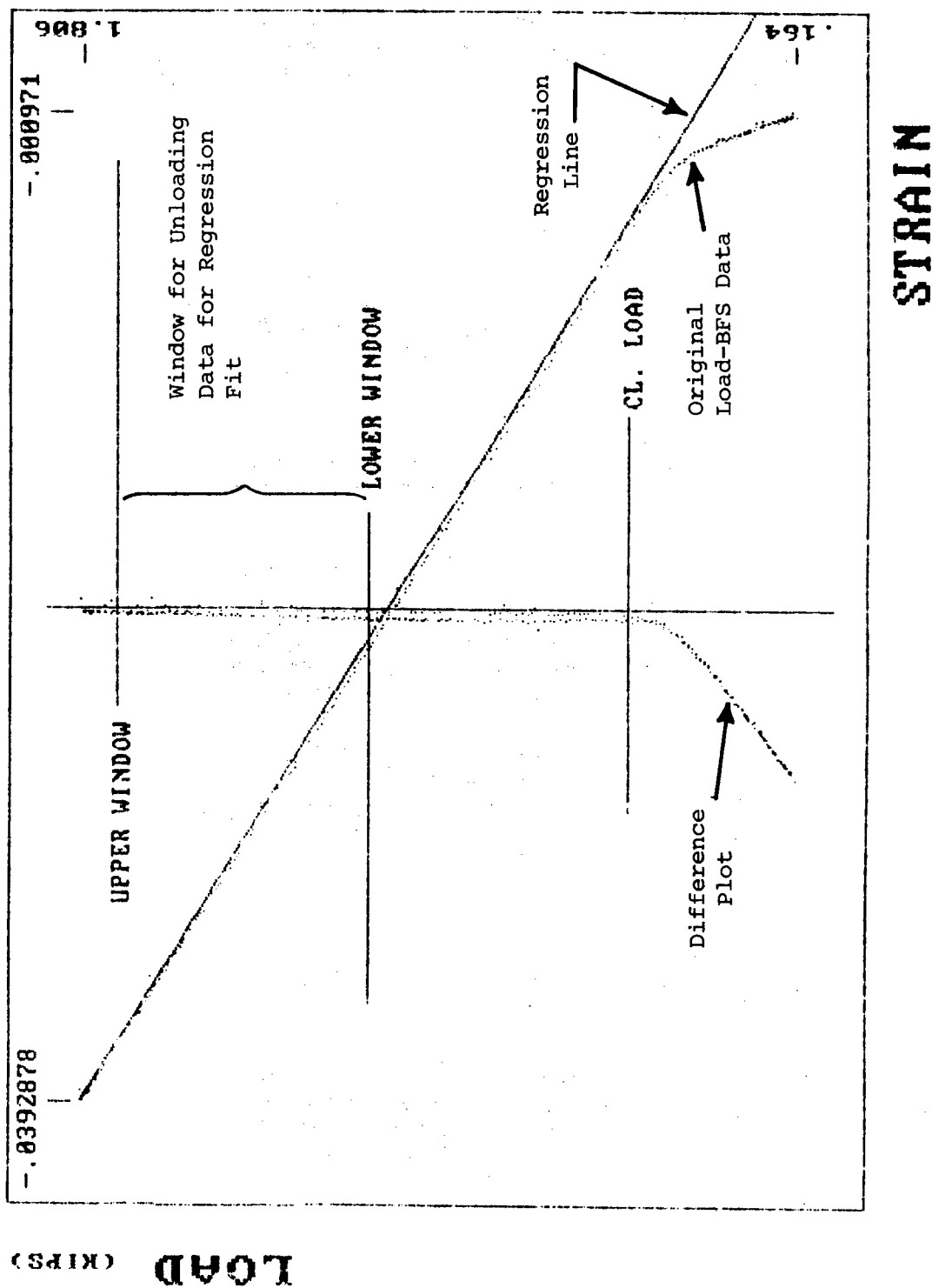


Figure 2.7. Plot of Load Versus Back-Face-Strain (BFS) Data and Closure Load Indication.

displacement data and the displacement calculated from linear regression line at the respective load values of the original data. The difference is multiplied by a factor of three before plotting, to enhance any deviation from the linear behavior. The window for the regression data and closure load level are indicated on the difference plot in Figure 2.7.

The operator must take care to ensure that erroneous load-displacement data are not accepted as accurate. Extensometer movement and pin friction may contribute to anomalies in the hysteresis loop. In these cases, the calculated closure loads may not be appropriate.

### 2.2.3 IBM AT System

A computer control system was developed to study the interaction of frequency, temperature, stress ratio, maximum stress intensity factor, and hold-time on crack growth rate behavior. A description of the test system hardware is given in Appendix A. The software was written in TBASIC language which is similar to Tektronix BASIC but faster than the interpretive BASIC.

Crack length is monitored by either the compliance or the electric potential method. Real-time crack length is used to control the load on the specimen to attain a specified history of stress intensity. Crack closure load is determined by using the similar method described in subsection 2.2.2. However, the closure load in this case, is selected by determining the load at which the displacement data deviates from the least square curve by an amount greater than  $n\sigma$ , where  $\sigma$  is the error of regression and  $n$  is a constant, usually chosen to be three.

The control system can be used to generate data on the effects of frequency, temperature, stress intensity ratio, maximum stress intensity, hold-time, and complex waveshapes on crack growth behavior.

#### **2.2.4 Improvements to the C20 HCF/LCF System**

The C20 system has been equipped with an IEEE-488 interface which allows the VIC-20 computer to address two HP multimeters and a Wavetek signal generator. The use of these multimeters provides the accuracy needed for electric potential measurement and simplifies measurement of the minor load signal. The IEEE controlled signal generator provides more accurate and easier to use minor load control than was provided through the previous interface, to the old Bruel and Kjaer shaker controller. The software developed to increase the efficiency of high cycle/low cycle fatigue testing is covered in paragraph 2.2.4.1, while hardware are covered in paragraph 2.2.4.2.

##### **2.2.4.1 Software Development for the C20 Test Machine**

A program "CTROL" was generated for automated high cycle/low cycle type testing utilizing the shaker test machines. The program provides automated crack growth testing and data recording with the following capabilities:

- DC or AC Electric Potential Crack Length Measurement
- Load Control Options of Constant Stress Intensity, Threshold, or Constant Load
- Data Logging for Major and Minor Loads, Crack Length, Major and Minor Cycles, and Elapsed Time
- X-Y Plotting of Data During the Test
- Load Displacement Measurements for Two Channels of Displacement (Intended for Strain Gage Signals) and Load

CTROL is written in BASIC for the Commodore VIC-20 computer configured as follows:

- IEEE-488 Interface (for Minor Command and Measurement and for DC Potential)

- Three D/A Cards (Command Major Load and X-Y Plotter Drives)
- One A/D Card (Measures Major Load)
- One Relay Driver Card (Plotter Pen Control)
- Disk Drive (Commodore 1541)
- 28K Memory
- Printer and X-Y Plotter.

Because of rapid crack growth possible at higher frequency testing, the main design criteria of the program was optimal data acquisition speed. Upon acquisition, the data is first stored in a RAM array and then at convenient intervals, transferred to the disk and printed. Execution of a complete data acquisition and control loop cycle is achieved in about 5 seconds. The data acquisition interval criteria is based on crack growth increment as well as elapsed time interval.

The task of measuring the high frequency signal of the minor load is conveniently accomplished with a digital voltmeter - an RMS value is measured and converted to peak-to-peak value.

A pop-up menu allows changing any test or data acquisition parameter during a test.

The stored test data may be transferred to the HOST computer by RS232 line using the Commodore computer and software "RS232".

#### **2.2.4.2 Hardware Improvements to the C20 System**

Improvements were made to achieve and maintain good alignment on this machine. First, the load frame was disassembled and mating surfaces were machine ground to closer tolerances. This improved the initial alignment and reduced alignment drift during the test. Secondly, an unique self-alignment unit (AU) has been designed and fabricated for installation in the load train above the load cell. Unlike some commercial available self-aligning grips, this unit provides both

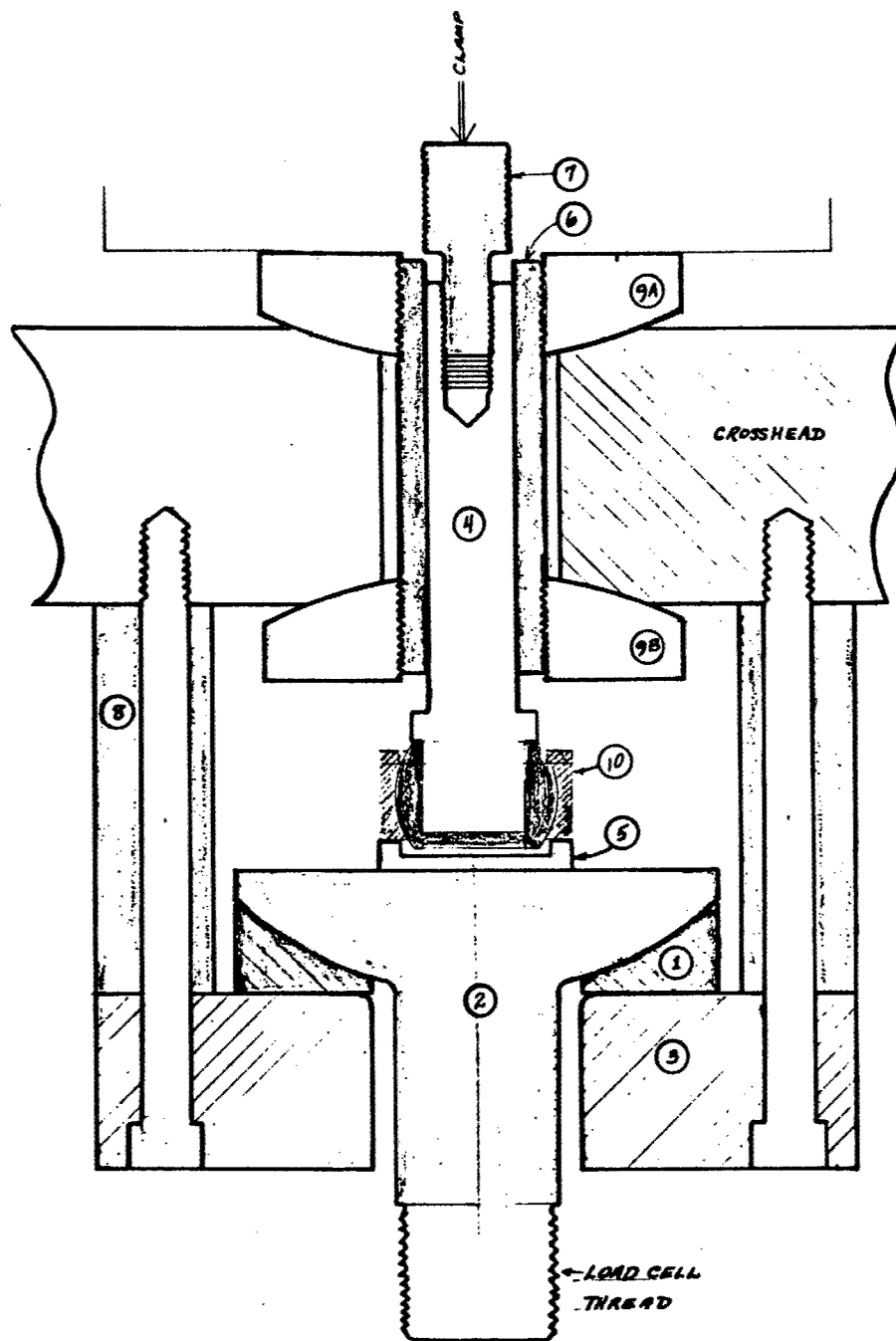
translational and rotational alignment capability. In addition, the AU incorporates air-bearing surfaces to allow low friction alignment seeking. A drawing of the AU is provided in Figure 2.8.

Special interlocks have been provided for the C20 to shut down the system in the event of a water leak in any of the cooling circuits. In addition to a conventional flow sensor device, actual water detector grids are now provided at various locations around the machine to detect leaks. These grids activate the interlock in the presence of as little as one drop of water. This precaution averts the possibility of shaker damage caused by water contamination of the dielectric oil used to cool the shaker circuits.

To allow faster data acquisition, an analog servo-controller has been implemented to control the major load air pressure. In this case, only a D/A command is executed to change a load - the CPU is immediately free while the servo adjusts the slow load change. However, the simple Partlow controller does need to be "tweaked" to provide required accuracy.

Two new power amplifiers, Model SK12/18 and Model SK18/18, were acquired from MB Dynamics of Cleveland, Ohio. The SK12 is equipped for 12 KW power output and is easily expandable up to 18 KW by plugging in 3 KW power modules. The SK18 is equipped to its maximum capability (18 KW) which can drive the Unholtz-Dickie shaker to maximum output. Either amplifier may be used to easily drive the C20 or C10 shakers to maximum output. The original MB T251 amplifier was retained for use with the C10. Reconnection time to switch from one amplifier to another is only 15 minutes.

The usable stroke capacity of the C20 was increased to accommodate the testing of specimens with high ductility. A vacuum pump has been connected to the air chamber which allows the shaker head to be positioned above center prior to the test. The vacuum source also makes possible some



<u>No.</u>	<u>Identification</u>	
1	Air Bearing	C20-AU01
2	Alignment Shaft	C20-AU02
3	Bearing Base	C20-AU03
4	Clamp Shaft	C20-AU04
5	Bearing Adapter	C20-AU05
6	Clamp Tube	C20-AU06
7	Cylinder Link	C20-AU07
8	Spacer	C20-AU08
9A	Curved Nut	C20-AU09
9B	Curved Nut	C20-AU09
10	Commercial Bearing	WRRG-14

Figure 2.8. Self-Aligning Unit.

compressive loading (approximately 1 kip) on the C20. However, only manual control is available for the vacuum at this time.

#### **2.2.5 C10 System Improvements**

The C10 was the prototype shaker-pneumatic test machine developed by UDRI and its load frame was not intended for routine testing. The alignment and crosshead stiffness have been improved, and simple modifications were made to the lower frame which allows easy access for changing and heating the specimen.

The VIC-20 computer, formerly used as a simple timer-control for the C10 system, has been enhanced to measure the loads and display them in convenient engineering units.

#### **2.2.6 Installation of VIC-20 on Major/Minor Test System**

A VIC-20 microcomputer was installed as a temporary test monitoring device on the Major/Minor test frame until an IBM System CS9000 unit is available. A standard stress-life test program is currently being conducted on alloy N4+ at various temperatures and load ratios. The VIC-20 monitors major load, minor load, high temperature, and low temperature interlocks, and interrupts the test in case of any system failure. The unit has been an economical, simple solution to the temporary lack of more sophisticated computer hardware for the system.

#### **2.2.7 IBM System CS9000 Installation on Vacuum Test System**

To provide test control and data acquisition capabilities, an IBM System CS9000 microcomputer has been installed on a servo-hydraulic test frame which contains a vacuum chamber. The system operates with the same test control software as the other IBM CS9000 based systems in the laboratory. However, certain system failures would be catastrophic to the vacuum pump and chamber heating elements, should they remain undetected and uncorrected. Additional interlocks are, therefore, being added to the hardware and logic incorporated in the software to protect the vacuum system in case of mechanical failure.

### **2.2.8     Software Enhancements**

Development of several new control programs and modifications to operational programs were completed. For the TEK 4052, software was developed to impose a combination of cyclic and hold-time loads on C(T) specimens. The loading profiles generated by the software are illustrated in Figure 2.9.

In Figure 2.9a, a number of cycles (M), which is selected by the operator, can be applied to the specimen. Then, a hold-time or dwell period ( $\tau_H$ ), which can be selected by the operator, is applied at the maximum load level. In Figure 2.9b, a single cyclic load is applied periodically within a sustained load. The time ( $\tau_H$ ) between the loading cycle is adjustable and the load magnitude ( $P_H$ ) during the hold-time can be selected by the operator. The load, shown in Figure 2.9b, has been used in the investigation described in paragraph 3.2.10..

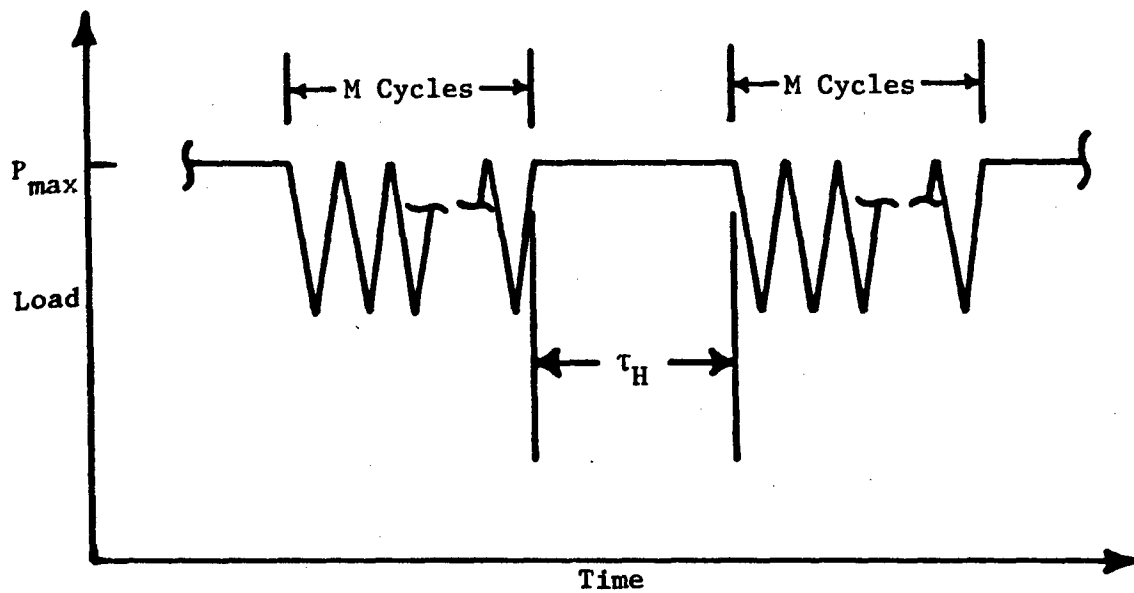
A modified TF-34 spectrum load generation has also been incorporated in the control software used on the TEK 4052. This spectrum, shown in Figure 2.10a, and loading profiles in Figure 2.9 were used to develop a life prediction model [5].

A simple overload spectrum condition, shown in Figure 2.10b, was developed for automated control systems using the IBM PC computers. The number of constant amplitude cycles (M), the load ratio (R), and the overload ratio ( $R_{OL}$ ) can be selected by the operator.

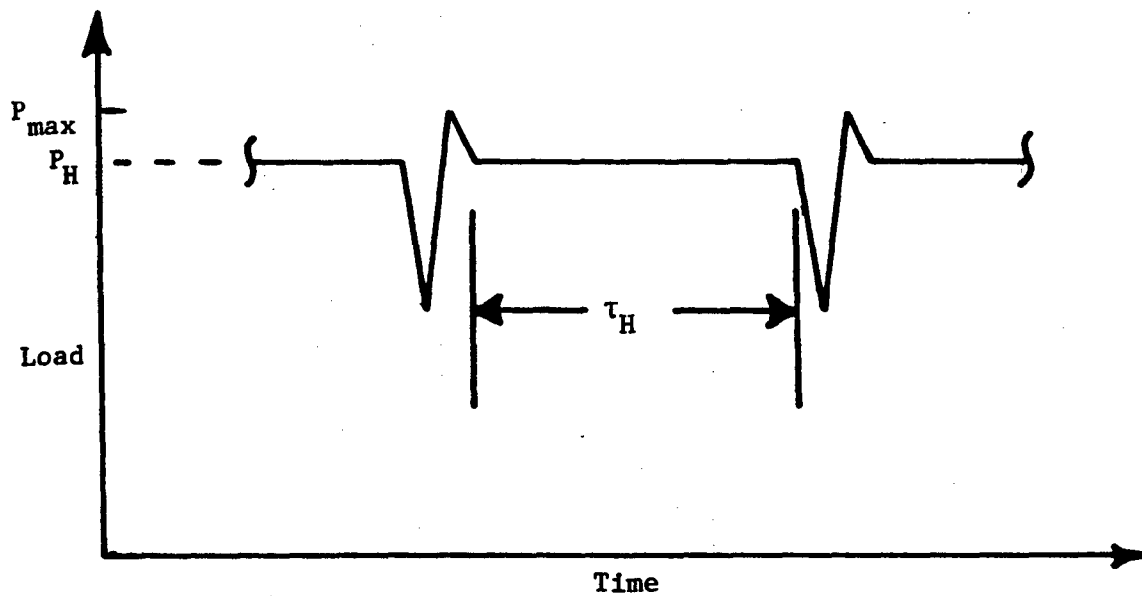
#### **2.2.8.1     Software Enhancements on IBM System CS9000**

Additional test and data reduction software for the IBM System CS9000 microcomputer have been developed to aid on-going laboratory test projects. The following packages are now available.

AUTOFCG Version 5.00 and 5.0a - Upgraded versions of the compliance based fatigue crack growth software, including support for HP5316A counter and automatic closure load calculation.

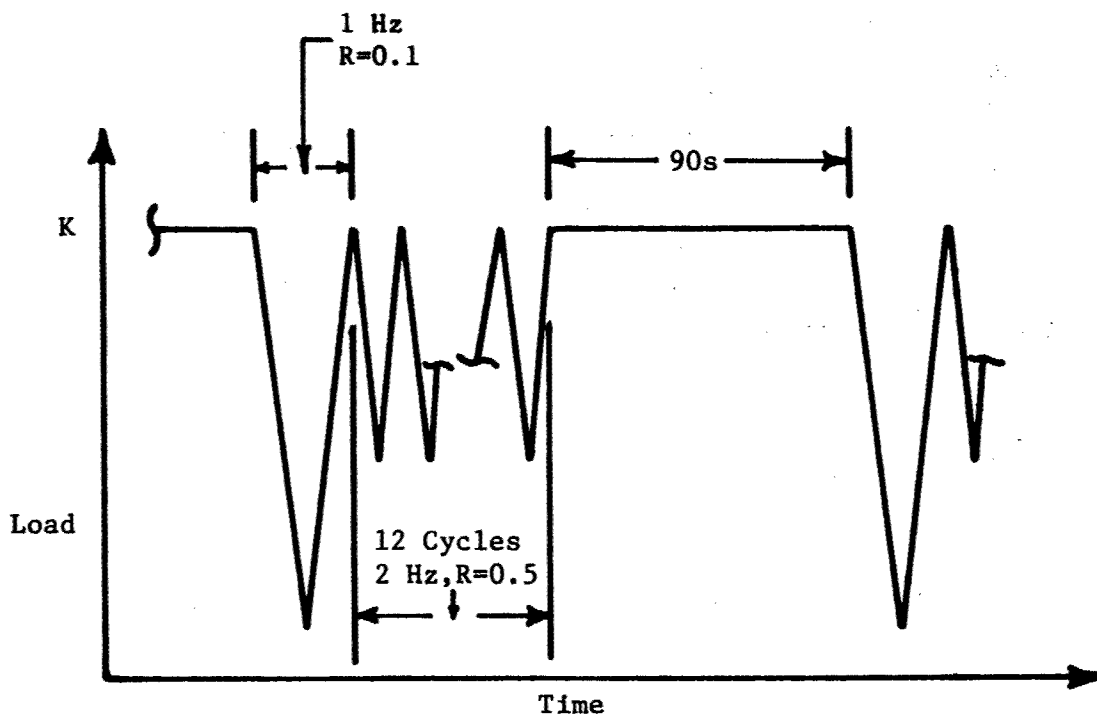


(a)

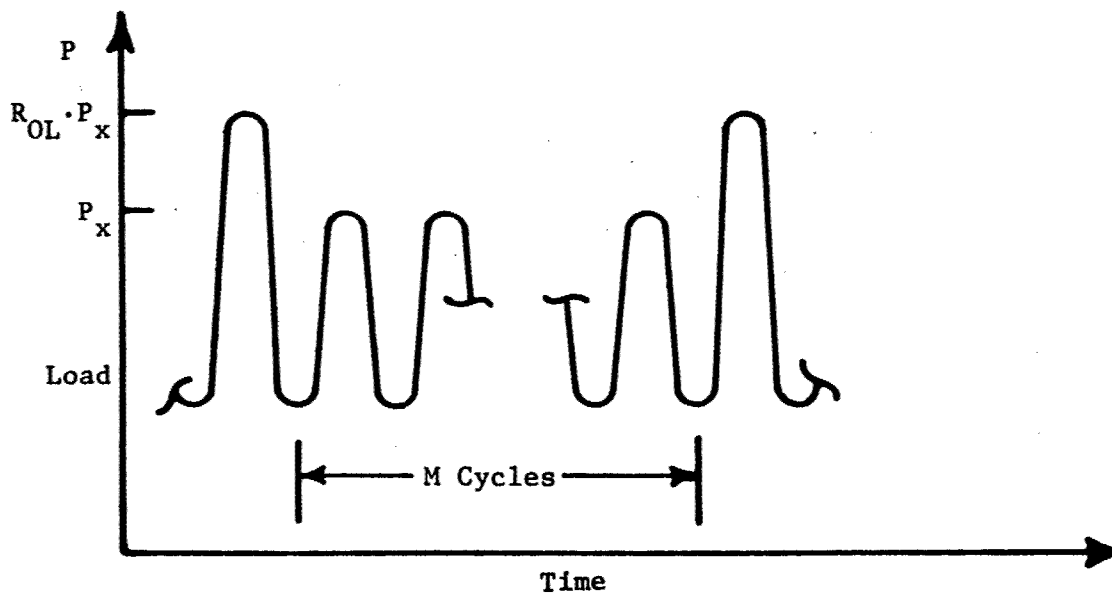


(b)

Figure 2.9. Combined Cyclic and Hold-Time Loadings Applied by Automated Control Software.



(a)



(b)

Figure 2.10. (a) Modified TF-34 Spectrum, and  
(b) Simple Overload Spectrum.

AUTOEP Version 5.00 and 5.0a - Upgraded versions of the automated electric potential crack growth software, including support for HP5316A counter.

AUTOIDG Version 4.22 - Upgraded version of the IDG control program.

SPIDG - A special IDG data reduction program designed to evaluate hysteresis loops taken from C(T) samples near the crack tip. Produces a closure load and compliance value as well as estimated crack length.

CLLD - A modified version of SPIDG which allows interactive manual selection of the closure load.

#### **2.2.8.2 Software Enhancements for PC Test Control System**

In previous work [6], software was developed to conduct an automated crack growth test under a periodic single-overload fatigue spectrum. A schematic of the applied load and the parameters that describe the load spectrum are shown in Figure 2.10b. Modifications were made to the software to support several research projects.

The program was modified so that the operator could automatically have hardcopies of the load displacement data made both before and after each overload. Also, the load displacement data could be stored on floppy disk or hard disk for subsequent analysis.

The original program used compliance information from crack mouth opening displacement measurements to determine crack lengths for C(T) specimens. The capability to use back-face strain compliance for crack length determination was added to the program to support higher test frequency requirements and to facilitate testing at elevated temperatures.

For the software that supports more common fatigue crack growth tests, an option was added to determine crack length from back-face strain measurements on single-edged cracked specimens.

## **2.3 REPAIR AND IMPROVEMENT OF THE MAJOR/MINOR TEST SYSTEM**

The Major/Minor test system was removed from service due to a damaged armature. This problem and several others associated with the equipment were identified and fixed.

### **2.3.1 Armature Failure**

The armature failure was traced to loose roller guides which allowed the moving armature to contact the fixed structure resulting in damage to the armature winding. The armature has been rewound by Environmental Equipments Ltd. (EEL).

To minimize future shutdown, the following improvements in preventative maintenance have been suggested:

- Periodic inspection based on system operational time. This will require partial disassembly of the shaker to inspect the armature roller guides.
- Close attention to load train alignment.
- Proper grip torquing procedure to eliminate any load transfer to the armature.

### **2.3.2 Water Cooling System**

The original aluminum heat exchangers were replaced with "gun metal" construction to reduce clogging by erosion. The internal shaker hoses were also replaced (while the armature was being rewound), as were the temperature switches.

The water cooling system requires nonelectrically conductive distilled water since it flows through energized coils in the shaker. Any additives to retard algae growth will increase the conductivity of water. Hence, the system water must be changed periodically.

The water inlet and outlet ports to the shaker have been equipped with pressure gages to monitor the differential pressure. In the future, this will allow early detection of restrictions in the small diameter flow circuits of the shaker.

### **2.3.3    Upgrading Control Equipment**

The operation of the original hydraulic control system had been plagued from the beginning by troublesome electronics, difficult maintenance procedures, delayed shipment of replacement parts, etc. Thus in 1986, the electronics (function generator, load signal conditioners, and servo-controller) were replaced with comparable equipment provided by another manufacturer. Specifically, a controller, function generator, load cell conditioner, and control panel were installed. These modifications made the operation of this unit both efficient and satisfactory.

### **2.3.4    Computer Interface**

A Commodore VIC-20 was temporarily used on the Major/Minor test system while awaiting a more suitable computer. It was used to monitor test parameters and provide fail safe shut-down.

An IBM CS9000 computer was subsequently interfaced to the system. Connections have been made for electric potential measurement as well as the load control and measurement circuits.

## SECTION 3

### MATERIAL CHARACTERIZATION TESTS

A variety of basic elevated temperature experiments were conducted to improve the characterization and understanding of material response in service conditions. Attempts were made to correlate the mechanical behavior with the original micro-structural characteristic of the material tested. The data were generated on crack closure, fatigue and creep crack growth, and creep rupture as well as hot corrosion behavior of several nickel-base superalloys and titanium alloys.

#### 3.1 CRACK CLOSURE

It is well known that the fatigue crack growth behavior of a material is influenced by crack closure phenomenon. However, a clear understanding of the closure mechanism is not available. In our attempt to improve this understanding, tests were conducted to study the effects of load history and specimen geometry on the fatigue crack closure measurements. In a separate study, the effect of closure on the growth of surface cracks was also investigated by conducting fatigue crack growth experiments on surface flaws introduced in a high-strength titanium alloy.

##### 3.1.1 Effects of Load History and Specimen Geometry on Fatigue Crack Closure Measurements

The phenomenon of crack closure affects the crack growth behavior in materials and hence, any attempt to predict the usable life of components under fatigue loads must account for crack closure. However, values of crack closure presented in the literature have been inconsistent. Various closure models are available but they seem to predict only limited sets of data. Crack closure is produced by many mechanisms; two important ones in this study are fracture surface roughness and the plastic wake. For these mechanisms, crack closure is dependent upon load

history and structural geometry, especially the structural thickness.

The effects on crack closure measurements of simple load histories and specimen sizes were investigated. Tests were conducted on compact type, C(T), specimens having various thicknesses and in-plane dimensions. The simple load histories were composed of constant amplitude load and stress intensity ranges.

Closure load was determined from data collected from three measurement techniques. In the first technique, a clip gage was used to determine the load displacement behavior at the crack mouth. As a second method, a strain gage was placed on the back-face of the C(T) specimen to determine the load-strain behavior. The third technique employed a laser interferometric displacement system where load displacement data were collected at various locations on the side of the specimen in the vicinity of the crack tip. Details of this investigation are presented in Reference 7.

### **3.1.2 Effect of Closure on the Crack Growth of Surface Cracks in a High Strength Titanium Alloy**

Fatigue crack growth experiments were conducted on surface flaws in a high strength titanium alloy. Cracks were initiated from semicircular notches introduced by electro-discharge machine (EDM) having approximate dimensions of 100 microns deep by 200 microns wide and having a height of 70 microns. Surface crack lengths in the range of 400 microns to 8 mm were investigated under both increasing and decreasing K conditions. Crack lengths and closure loads were determined from load displacement data obtained with the aid of a laser interferometric displacement gage which had a resolution capability of 0.1 micron. Stress ratios of 0.1, 0.5, and -1.0 were utilized. Crack growth rates were compared for all three stress ratios as a function of  $\Delta K$  and  $\Delta K_{eff}$  which was determined from the closure data. The use of effective stress intensity

range consolidated most of the data in a small band. The test procedure and results are discussed in Reference 8.

### **3.1.3 Crack Closure Measurement Through Fractography**

Currently, several experimental techniques are available for measuring crack closure. The values obtained from these techniques are not compatible with each other, hence, they pose a problem of reliability. Pelloux, et al. [9] used high resolution electron fractography to assess crack tip closure. This method was later modified by Sunder, et al. [10]. It uses a specially designed load sequence with a constant maximum stress and gradually decreasing minimum stress. The stress levels are carefully chosen to leave behind striation patterns on the fracture surface. The crack closure is then estimated by counting the number of equally spaced striations. Crack closure data obtained from this technique provides an accurate and reproducible value of closure stress.

A program was initiated to investigate the capability of this technique in determining the closure response to overload. The material chosen was Aluminum 7475 alloy. A programmed loading sequence of variable amplitude as shown in Figure 3.1 was applied at room temperature. The test was conducted on a subcompact tension specimen under automated control. Closure values were simultaneously recorded through back-face strain measurements. An overload of 80% was applied after a specified amount of crack growth, as shown schematically in Figure 3.2. After the test, the specimen was broken into two halves and the fracture surface replicated. The replica was then observed under TEM to analyze the striations produced. Figures 3.3a and 3.3b show striation spacing for the load sequence before and after, respectively, an 80% overload. These photographs were approximately 170 microns apart in the direction of crack growth. The striation spacing indicates an increase in closure level after the overload of up to 55%. However, no increase in closure due to overload could be picked up by the back-face strain gage technique. This indicates that the fractographic technique may

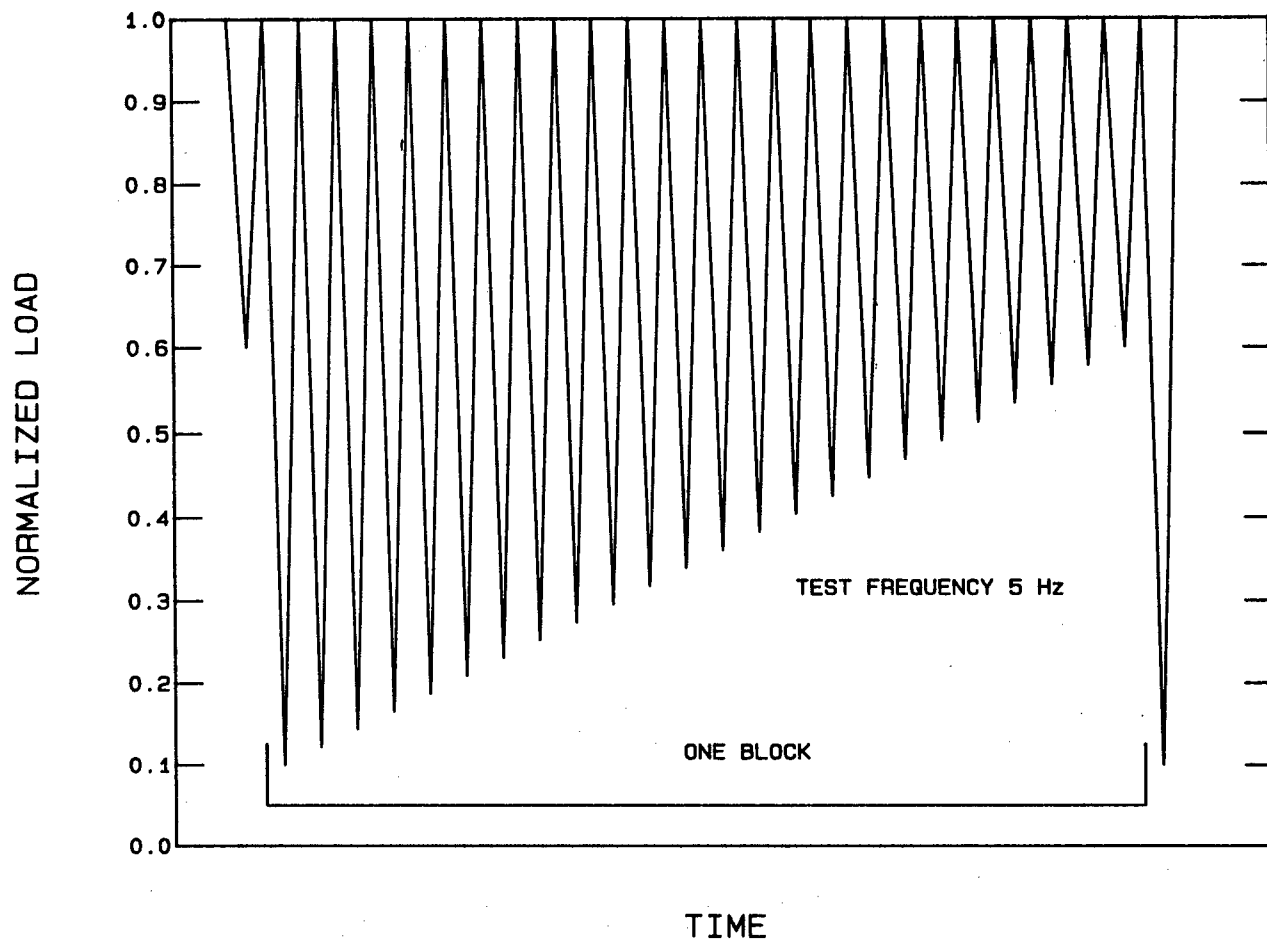


Figure 3.1. Load Sequence for Fractography Based Crack Closure Evaluation.

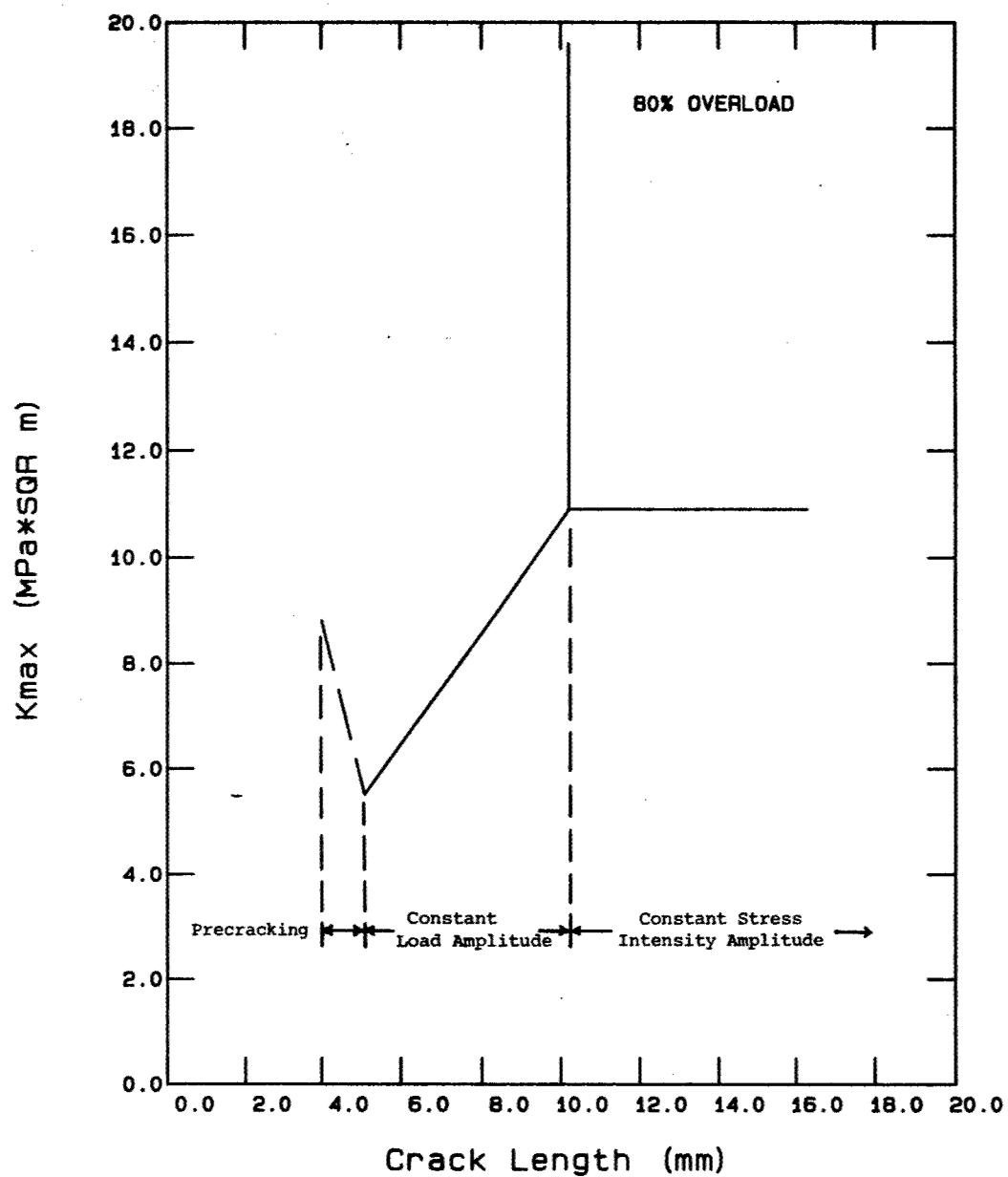
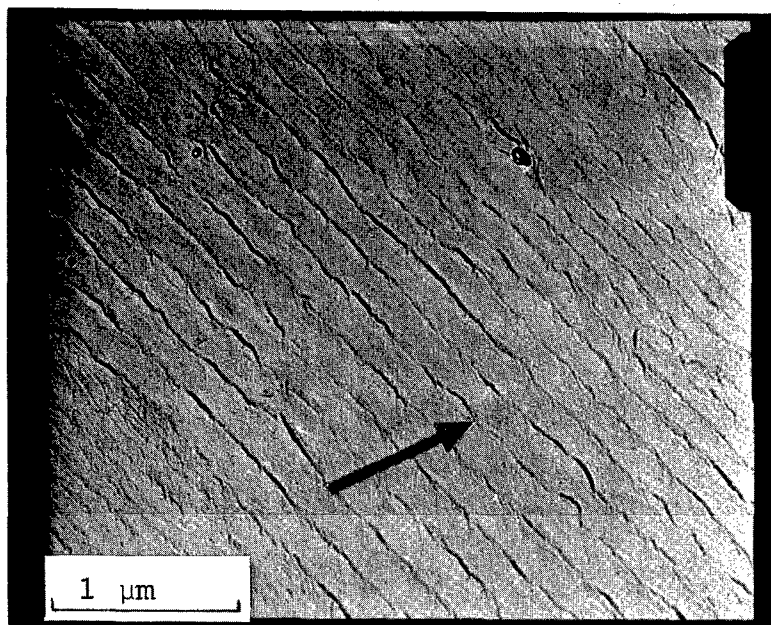
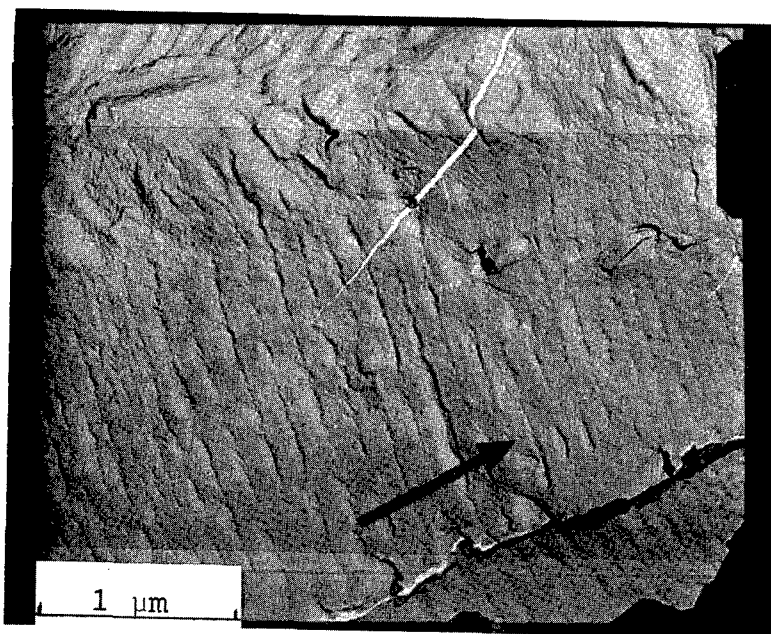


Figure 3.2. Schematic of K-Profile for Closure Test.



a. Before Overload: Note Eleven Equally Spaced Striation.



b. After Overload: Note the Increase in Equally Spaced Striation.

Figure 3.3. Transmission Electron Microscope Photograph  
Taken from Replica of Fatigued Specimen  
(X25000).

be more sensitive than other experimental methods typically used to account for increased closure due to overload.

### **3.2 FATIGUE CRACK GROWTH TESTING**

#### **3.2.1 TMF Baseline Testing**

Thermal/mechanical fatigue (TMF) tests have been performed to check out the new TMF test system and to provide baseline data for more advanced TMF test programs. Testing performed to date includes high frequency mechanical loading (600 cpm) combined with a slower thermal cycle (2 cpm). The results of these tests are being analyzed to determine if linear summation models based on isothermal fatigue data can predict crack growth behavior under nonisothermal conditions. These studies indicate that a more complex model incorporating both cycle- and time-dependent behavior may be required to obtain the desired results.

#### **3.2.2 HCF/LCF Initiation in IN718**

Under low cycle fatigue (LCF) loading, a major portion of life is used to initiate a detectable crack. In many components in a modern gas turbine engine, high frequency cyclic loads (HCF) are also present. The influence of HCF loads on the LCF behavior was investigated in this effort.

A matrix of tests were conducted using axial load fatigue specimens of Inconel 718 sheet at 649°C and 538°C on the C10 electro-pneumatic shaker. All tests were conducted under load control using an LCF trapezoidal waveshape at 0.33 Hz and  $R = 0.1$  with a 180 s hold-time at maximum load. During the hold-time, a 200 Hz sinusoidal HCF load was superimposed. The amplitude of this minor cycle loading was varied from zero to values where the failure mode was obviously high cycle fatigue. Baseline tests were also conducted under LCF loads with no hold-times at 649°C and under HCF constant amplitude loads at 538°C.

The two temperatures were chosen because the material behavior was almost time-dependent at the higher

temperature while it was almost entirely cycle-dependent at the lower temperature. Thus, in the absence of the minor cycles, the failure at 649°C was due primarily to sustained load while at 538°C, the hold-times had no effect and failure was due to low cycle fatigue. A limited amount of testing was also planned at an intermediate temperature.

### **3.2.3 HCF/LCF Initiation in N4+**

Crack initiation tests on single crystal alloy N4+ have been conducted at elevated temperatures using the Major/Minor test frame. Smooth tensile bar geometry specimens in both coated and uncoated surface condition have been tested at a frequency of 250 Hz at temperatures of 871°C (1600°F) and 1093°C (2000°F).

A number of experimental difficulties with temperature control, electro-hydraulic system controller breakdown, and finally, a shaker malfunction have delayed completion of this test matrix. The addition of an IBM CS9000 microcomputer and IRCON two color pyrometer as well as the replacement of the electro-hydraulic system controller should improve the control of the test parameters and increase the reliability of the test system.

### **3.2.4 HCF/LCF Initiation in Hastalloy X**

An investigation was conducted to determine the life of Hastalloy X sheet material, 0.5 mm thick, under combined high cycle fatigue and low cycle fatigue (HCF/LCF) load conditions at 427°C (800°F). The desired test frequency of HCF loads was in the kiloHertz range. At these frequencies, the loading system and the specimen interact very strongly. Thus, a preliminary task was initiated to evaluate the optimum specimen design and to determine an operating frequency.

The specimen material for the preliminary task was chosen to be steel because it was easy to obtain. The specimens were conveniently fabricated, and the modulus/stiffness was comparable to Hastalloy X at room temperature and at the test

temperature. Various sizes of steel specimens, 0.5 mm thick, were tested in the C20 electro-pneumatic shaker system to evaluate the specimen/system response at frequencies greater than one kiloHertz.

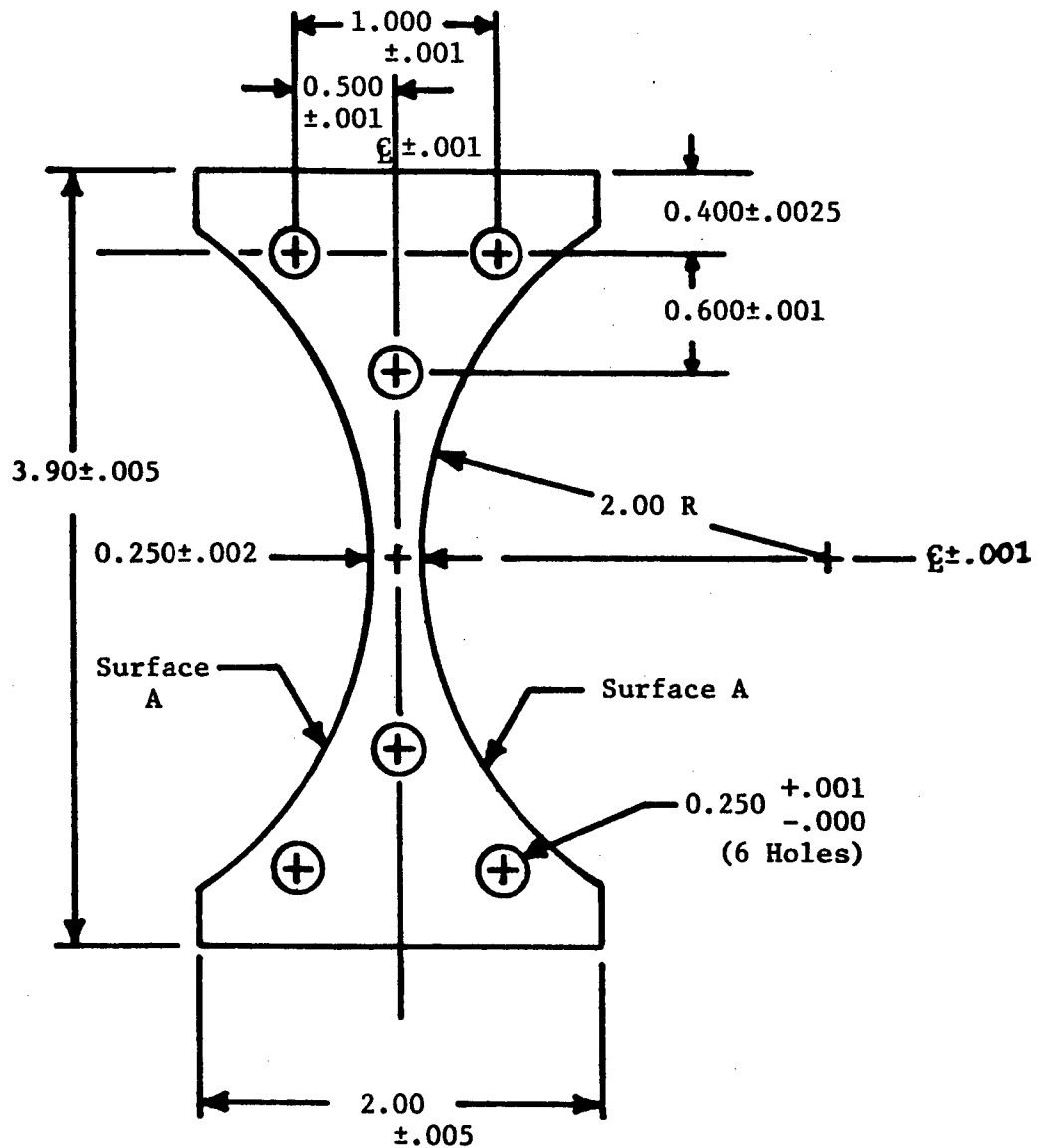
The steel specimens were strain-gaged both for room and 427°C test temperatures to determine the following:

1. Minor load capability as a function of frequency,
2. Percent specimen bending at antinode frequencies, and,
3. Calibration factor for force gage at selected test frequencies and load levels.

A frequency of 1120 Hz was chosen, having a slight resonance advantage and low bending. Correlation of strain gage to force gage signals showed a ratio of 1.1:1 which was relatively independent of LCF and HCF load amplitudes. The specimen configuration is shown in Figure 3.4. Initial testing was plagued with the elastic-plastic elongation of the Hastalloy X which approximately doubled the specimen compliance and resulted in decreased HCF load capability. The beginning HCF load capability for this specimen at 1120 Hz was 124 MPa peak-to-peak ( $\pm 63$  MPa about the mean load) but diminished to 49 MPa peak-to-peak with approximately 30% elongation of the specimen. Details of this investigation are described in Reference 11.

### **3.2.5 Fatigue Crack Growth Behavior of IN718**

Data were generated under different test conditions to model the fatigue crack growth behavior of IN718 for various load, temperature, specimen geometry, and environment. Fatigue crack growth experiments were conducted at 649°C under conditions of high load ratio and frequency to study the interaction of cycle- and time-dependent crack growth. Crack growth rate and micro-mechanisms of growth were found to be a function of frequency for a given R value and could be separated into three distinct frequency regimes - fully time-dependent behavior for lower frequencies, fully cycle-dependent behavior for higher



All Dimensions in Inches

Figure 3.4. HCF/LCF Specimen Configuration.

frequencies, and mixed cycle/time-dependent micro-mechanisms for intermediate frequencies. Increasing values of K were found to shift the transition frequencies of these behavior regimes towards higher frequency values.

This investigation was extended to study the crack growth rate of Inconel 718 in vacuum [12]. Frequencies ranging from 0.001 to 5 Hz were used to investigate the influence of frequency and environment on crack growth. Three R values (0.1, 0.5, and 0.8) were employed in the study.

It was also found that in vacuum, the fatigue crack growth rates as a function of frequency can be represented by three distinct crack growth regimes, similar to that observed in air. Comparison of the results obtained in vacuum and air shows that the air environment has a detrimental influence on the crack growth in the time-dependent and mixed regimes and negligible effect in cycle-dependent regime. The mechanism of intergranular crack growth in the time-dependent regime in vacuum was found to be creep cavitation of the grain boundaries ahead of the crack tip while in air, the crack growth accelerated simply by environmental degradation [12].

#### **3.2.6 Fatigue Crack Growth at High Load Ratios in the Time-Dependent Regime**

Experimental crack growth rates were determined in Inconel 718 M(T) specimens at 649°C under conditions of high load ratio (R) and frequency (10 to 100 Hz). Under these conditions, the material displays cycle-dependent crack growth as well as time-dependent crack growth. At R values approaching unity, the observed growth rates were lower than those obtained under sustained load at the same mean load in the absence of the superimposed cyclic loading. Tests on C(T) specimens at lower frequencies were used to demonstrate the existence of three regions of behavior -- cycle-dependent, mixed mode, and time-dependent.

A linear cumulative damage model was used to predict the growth rates due to combined cycle-dependent and

time-dependent mechanisms. The model was developed from 427°C data for the cycle-dependent term and sustained load crack growth data obtained at 649°C for the time-dependent term. Although the model could not predict the synergistic effect at high R, it provided a reasonable representation of much of the data. It was concluded that the use of low temperature data for the cyclic term was inadequate for representing the threshold values and growth rates at low  $\Delta K$  values at the higher temperature. Details of this investigation are presented in Reference 13.

### 3.2.7 Variable R Tests at Constant $K_{\max}$ for Inconel 718

Crack growth of Inconel 718 was studied as a function of R at a constant  $K_{\max}$  level of 40 MPa.m<sup>0.5</sup>. Temperature and frequency conditions for the experiments were selected to obtain the crack growth in the three different regions exhibiting time-dependent, cycle-dependent, and mixed mode behavior. The test conditions and results of these tests are identified in Figure 3.5 where crack growth rate is presented as a function of a stress ratio function (1-R). The conditions of T = 650°C and f = 0.005 Hz produce crack growth behavior which is fully time-dependent; the growth rate is noted to increase slightly with decreasing (1-R). Obviously, the crack growth is controlled by  $K_{\max}$  rather than delta-K. Cycle-dependent behavior occurs under conditions of T = 316°C and f = 1.0 Hz; the crack growth behavior increases with increasing (1-R) up to (1-R) = 0.7 or increasing delta-K (up to 28 MPa.m<sup>0.5</sup>). As expected, the crack growth rate is controlled by the delta-K. Delta-K also controls the behavior for the mixed crack growth regime (T = 650°C, f = 1 Hz, and 0.7 > (1-R) > 0.2). In this case, crack growth changes from the mixed growth behavior to the fully time-dependent growth behavior for (1-R) less than 0.2.

Growth rate is observed to remain constant for both mixed and cycle-dependent regimes of crack growth when 1-R exceeds 0.7. In this constant growth rate regime, the crack driving force delta- $K_{\text{eff}}$  remains unchanged. For ease of

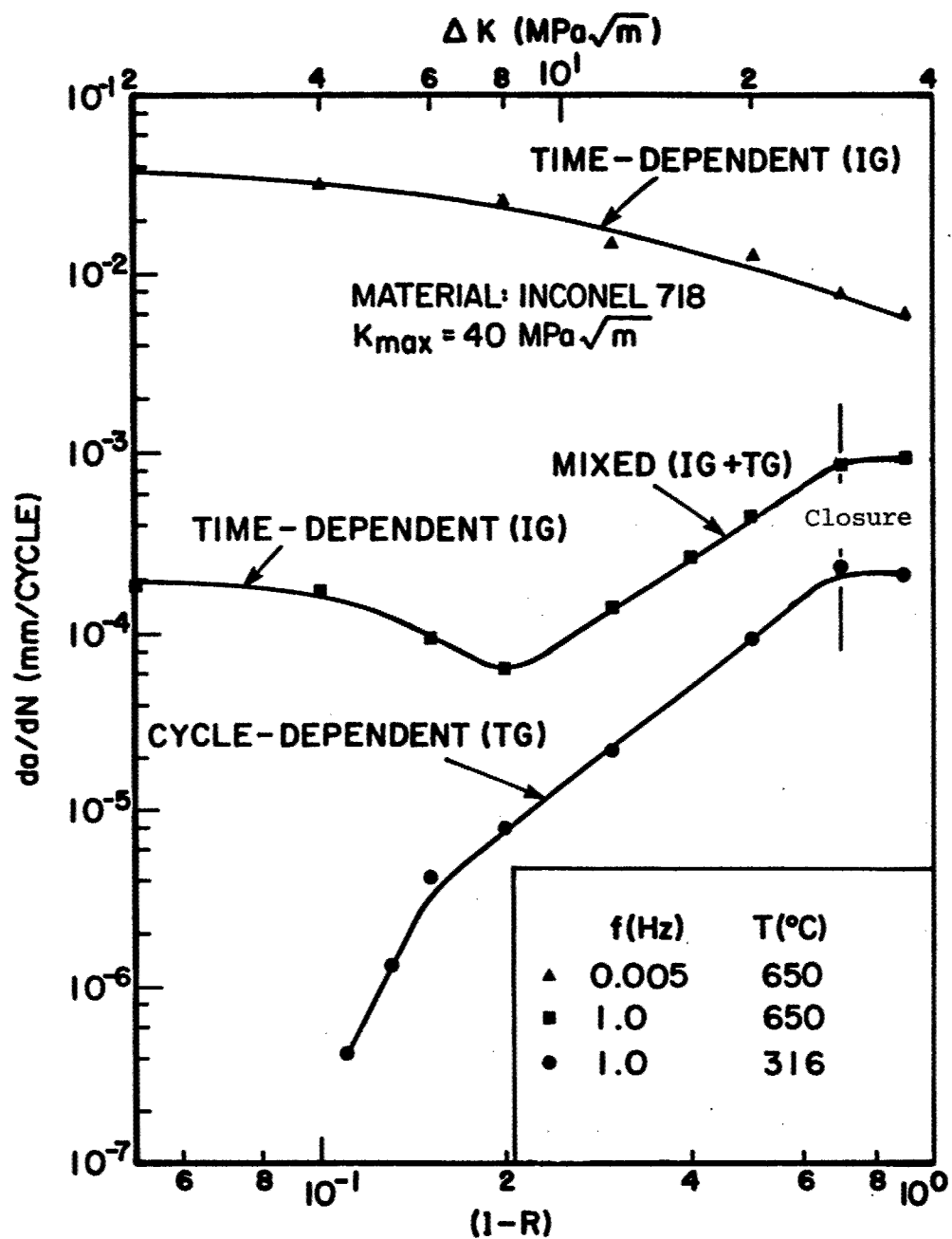


Figure 3.5. Three Modes of Fatigue Crack Growth Behavior Presented as a Function of (1-R).

explanation, the crack driving force,  $\Delta K_{eff}$ , is defined by the following expression

$$\Delta K_{eff} = K_{max} - K_{closure}, \text{ for } K_{min} < K_{closure}$$

$$\Delta K_{eff} = K_{max} - K_{min}, \text{ for } K_{min} > K_{closure}.$$

It can be seen from the above expression that for a test at constant  $K_{max}$ ,  $K_{min}$  ( $K_{min} = RK_{max}$ ) should be less than  $K_{closure}$  for  $\Delta K_{eff}$  to remain unchanged with increasing values of  $R$ . As  $R$  is gradually increased,  $K_{min}$  increases also and exceeds  $K_{closure}$  at  $R = 0.3$ . At this point, crack growth rate is noticed to decrease suggesting that  $\Delta K_{eff}$  is decreasing. Thus, the  $K_{min}$  value approaches  $K_{closure}$  at a value of  $R$  which corresponds to the beginning of decrease in crack growth rate.

### 3.2.8 Modeling of IN718 Crack Growth Behavior

A typical engine component service environment consists of combinations of various frequencies, maximum loads, temperatures, load ratios, and load hold-times. A study of crack growth rate behavior under these conditions leads to methodologies and modeling approaches which can be used to predict actual service behavior.

A series of tests were performed to acquire a database which could be used to develop and evaluate various crack growth rate models. Data was acquired to determine frequency ( $f$ ), temperature ( $T$ ), load ratio ( $R$ ), and maximum stress intensity ( $K_{max}$ ) effects and to correlate these with observed failure mechanisms ( $M$ ). A summary of some of these data is presented in Figures 3.6 and 3.7. Three distinct regions of crack growth behavior can be identified on the plot, which can be modeled separately.

The general form of the model [14] is given by the expression

$$[da/dN]_M = C_M \cdot f_1(K_{max}) \cdot f_2(f) \cdot f_3(R) \cdot f_4(T) \quad (3)$$

where  $f_1$ ,  $f_2$ ,  $f_3$ , and  $f_4$  are defined separately for the three

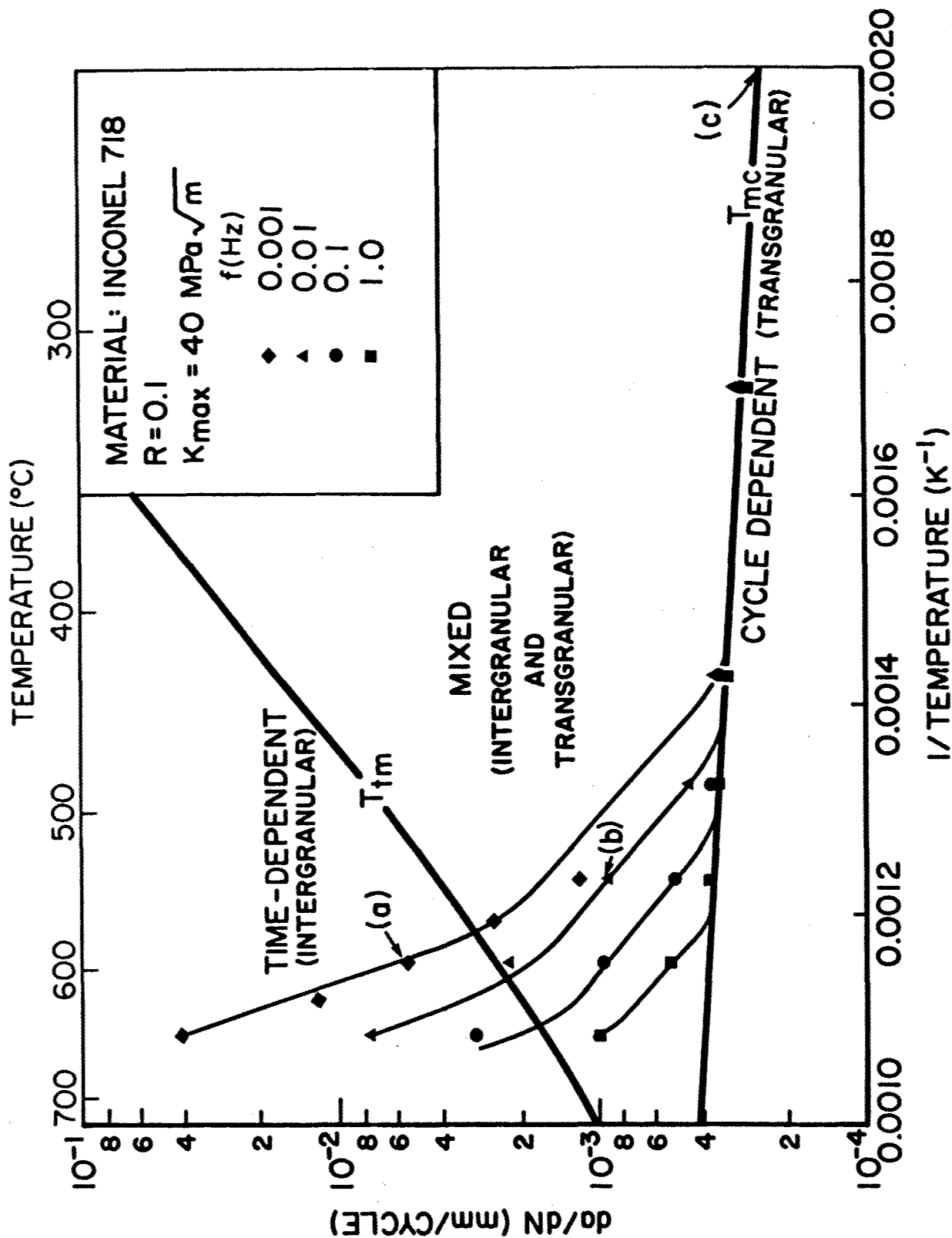


Figure 3.6.  $da/dN$  vs  $1/T$  Plot at  $K_{max} = 40 \text{ MPa}\sqrt{m}$  showing the Change in Micro-Mechanism of Crack Growth with Changes in Frequency and Temperature.

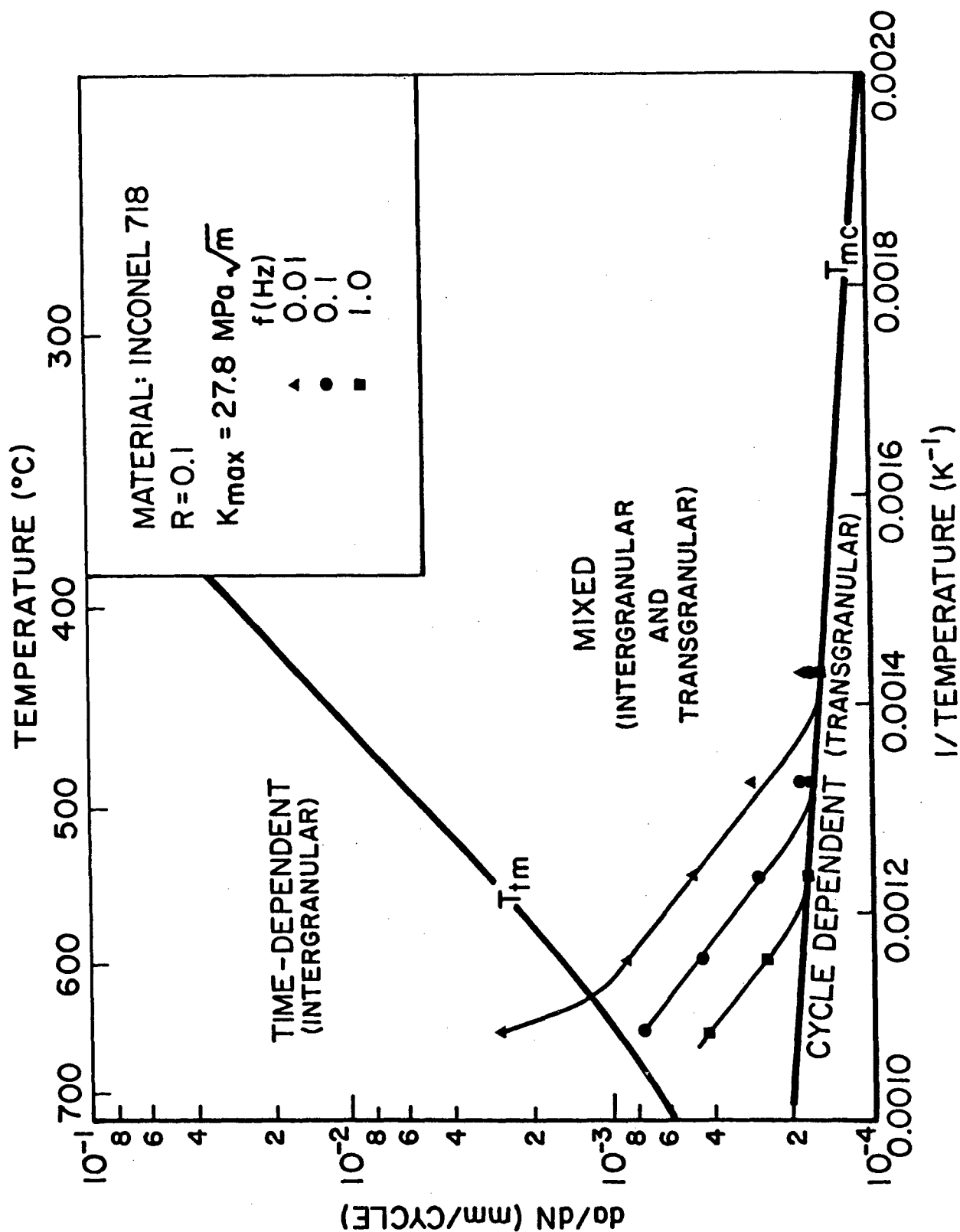


Figure 3.7.  $da/dN$  vs  $1/T$  Plot at  $K_{max} = 27.8 \text{ MPa}\sqrt{m}$  Showing the Change in Micro-Mechanism of Crack Growth with Changes in Frequency and Temperature.

crack growth regions. Separate functional forms and associated constants in the expression for the three crack growth regimes are given in Tables 3.1 and 3.2. Observed fracture morphology provides a physical basis for these three different modes of crack growth.

### 3.2.9 Threshold Evaluation of IN718

Evaluation of crack growth behavior in materials used in gas turbine engines has indicated the existence of both cycle-dependent and time-dependent effects. In determining the life of critical components, both types of effects and their interaction must be taken into consideration in a model. It has been shown that the stress intensity factor is an important parameter in characterizing both the cycle- and the time-dependent behavior in a life prediction model. Since a major portion of life is spent at the low growth rates, the behavior of the material must be well understood in this near-threshold regime. The crack growth behavior can also be time-dependent; thus, the load history and the frequency may affect the near-threshold response.

An experimental program was conducted to evaluate the effects of frequency and hold-time on the near-threshold crack growth behavior of Inconel 718 at 649°C in laboratory air. Frequencies from 0.01 to 30 Hz and hold-times up to 50 s were applied to C(T) specimens using a computer controlled test machine. Closure loads were determined from digitally acquired load displacement data. Several tests using high stress ratios (R) were used to assess the influence of closure in the low growth rate regime. Various loading histories were employed to achieve near-threshold growth rates.

Several mechanisms known to affect threshold and low crack growth rates were evaluated. Of primary consideration was the influence of closure. Both the oxide formation and the inelastic deformation wake behind the crack tip were considered as possible mechanisms which can affect the closure behavior. The experimental data generated in this program were used to

TABLE 3.1

CONSTANTS AND INDIVIDUAL FUNCTIONS OF THE MODEL  
FOR EACH CRACK GROWTH REGION FOR A CONSTANT TEMPERATURE, T

$$[da/dN]_M = F_M = C_{TM} \cdot f_1(K_{max}) \cdot f_2(f) \cdot f_3(R)$$

where M = c, m, or t

Regime, M	Stress-Intensity ( $K_{max}$ )	Frequency (f)	Stress-Ratio (R)
Subscript	$f_1(K_{max}) = K^n_{max}$	$f_2(f) = f^{-\alpha}$	$f_3(R)$

Time, t	$n = 3$	$\alpha = 1$	$[1 - R^{n+1}]$ $(n+1)(1-R)$ where $n = 3.00$
---------	---------	--------------	---

Mixed, m	$n = 2.42$	$\alpha = 0.34$	$(1-R)^m$ where $m = 1.50$
----------	------------	-----------------	-------------------------------

Cycle, c	$n = 3.04$	$\alpha = 0$	$(1-R)^m$ where $m = 2.14$
----------	------------	--------------	-------------------------------

TABLE 3.2  
TEMPERATURE-DEPENDENT FUNCTION FOR EACH  
CRACK GROWTH REGION

( $K_{\max}$  is in MPa. $\sqrt{m}$ ,  $f$  is in Hz, and  $da/dN$  is in mm/Cycle)

Regime Subscript M	Temperature (T) $f_4(T) = \exp(-Q/R_g \cdot T)$ where Q is	$C_M$
Time, t	245 kJ.mol <sup>-1</sup>	1.70E+5
Mixed, m	66 kJ.mol <sup>-1</sup>	7.63E-4
Cycle, c	4 kJ.mol <sup>-1</sup>	1.43E-8

correlate near-threshold crack growth rates with frequency,  $R$ , and prior load history. Results of this investigation are presented in Reference 15.

#### **3.2.10 Effect of Overloads on Alloy IN718**

Crack growth rate experiments were conducted on C(T) specimens of Inconel 718 at 649°C. The loading spectrum consisted of a single 1 Hz cycle at  $R = 0.1$  and a hold-time. The ratio,  $R_{in}$ , of the hold-time load to the maximum load of the fatigue cycle was 1.0, 0.9, 0.8, and 0.5 with hold-times from 0 to 2000 s. Tests were performed under computer controlled constant maximum  $K$  conditions at  $K_{max} = 40$  and 50 MPa. $\sqrt{m}$ . Data show that for  $R_{in} = 1.0$ , a linear summation model works well, while at  $R_{in} = 0.9$ , there is a measurable retardation effect on the crack growth during the hold-time. For values of  $R_{in}$  less than 0.8, the sustained load crack growth is almost completely eliminated. A simple retardation model was proposed which can fit the experimental data; this model was based on the concept of an overload plastic zone being produced by the fatigue cycles. It was concluded that hold-times do not contribute to crack growth in this material unless their amplitude is at or near the maximum amplitude of the adjacent fatigue cycles [16].

#### **3.2.11 Fracture Surface Analysis of IN718 Tested Under TMF Conditions**

An investigation was conducted to study the crack growth morphology developed in a nickel-base superalloy under load controlled thermo-mechanical cycling. Fracture specimens from the crack growth experiments conducted under two different conditions were analyzed. In the first set of experiments, tests were conducted with different phase angles and the temperature was cycled between 427°C and 649°C using an M(T) specimen while in the other experiment, isothermal temperature shedding was utilized on a C(T) specimen. The fracture surfaces were analyzed under SEM.

All the TMF cycling data were found to be bounded by the isothermal data obtained at maximum and minimum

temperatures. In-phase TMF cycling was the most damaging leading to the highest growth rates. However, this growth rate was lower than the growth rate corresponding to the same  $\Delta K$  at the maximum isothermal temperature. The lowest TMF cycling crack growth damage occurred under out-of-phase TMF cycling. However, this growth rate was still higher than the crack growth obtained at a given  $\Delta K$  corresponding to the lowest temperature in isothermal conditions. Higher growth rates were found to be associated with a greater amount of environmentally enhanced time-dependent intergranular mode of crack growth as seen under isothermal conditions. Most of the crack growth damage occurred on the rising portion of the loading cycle. Extensive intergranular time-dependent damage occurred when the temperature and load peaked together. Cycle-dependent transgranular type of crack growth resulted when the lowest temperature was in phase with the highest load [17].

### **3.2.12 Surface Flaw/Short Crack in Ti Alloys**

A computerized interferometric displacement gage was used to monitor the crack mouth opening behavior of naturally initiated small fatigue cracks in the high strength titanium alloy Ti-6Al-2Sn-4Zr-6Mo. Complete load versus displacement curves were obtained for naturally initiated semi-circular crack of surface length as small as 60 microns. For a crack of this size, the maximum crack mouth opening displacement was less than 0.5 microns and the precision of the individual displacement measurements was approximately 0.01 microns. Excellent correlation between crack mouth opening compliance and surface crack length was demonstrated, and the data were shown to agree with an analytical expression for part-through surface cracks.

A matrix of experiments was performed for a range of loading conditions, and crack growth data were plotted versus the nominal  $\Delta K$  and effective  $\Delta K$ . The effective  $\Delta K$  was defined using crack closure measurements. Experimental measurements obtained for a small crack indicated that closure often develops discontinuously as the crack initially extends. This behavior

appears to result from the formation of individual asperities on the fracture surface. In general, the interferometric method proved to be very effective and demonstrated unique capability to monitor the behavior of very small fatigue cracks.

### **3.2.13 Crack Growth from Notches**

In aircraft engine components, cracks normally initiate from the locations of stress concentrations such as notches and inclusions. Short cracks originating from these stress concentrations will initially grow through a decreasing notch-affected stress field. Due to the 'short crack' effect, initial growth rates may not be correlated by the parameters that are typically used to correlate long crack growth rates. When the notch tip stress is higher than the yield strength of the material, the notch is enveloped by a plastic zone. In these cases, the cracks which are initiated at the stress concentration locations initially grow through the plastic zone. The early growth of the short crack is within the notched plastic zone. At higher temperatures, the problem of predicting the life of a short crack is further complicated by the time-dependent effects of the material on the notch plastic zone. Due to these complications, it is very important to understand the behavior of short cracks at the notches, to develop improved life prediction models for aircraft engine components operating at elevated temperatures.

An investigation was initiated to study and understand the growth of cracks from a notch. C(T) specimens with a keyhole  $K_t = 4.29$  were fabricated for this study. The tests were conducted at 650°C on Inconel 718 specimens at a frequency of 1 Hz. The entire specimen, including the notch, was first mechanically polished. Then the specimen was electro-polished to remove any residual stresses created by the mechanical polishing process.

During the tests, crack lengths were monitored both with electric potential and compliance methods. The electric

potential technique was found to be more precise for detecting the crack initiation as compared to compliance method.

The crack growth tests were conducted at two different load levels of 5133 N and 3336 N. These loads were chosen to create two conditions - a notched plastic zone produced by higher load and an unaffected one (negligible plastic zone) at the lower load. Cracks were grown to a crack length of 3.80 mm from the notch tip of the specimen. Crack growth rates are shown as a function of the crack length in Figure 3.8. Figures 3.9 and 3.10 describe the crack growth rates vs stress intensity factor behavior for the low and high load conditions, respectively.

In Figure 3.8, the fatigue crack growth rate for the low load condition is seen to increase continuously with crack length. Figure 3.9 shows that, at the short crack lengths, the growth rates are higher than those for long crack data corresponding to the same elastic stress intensity range. In the higher load test, Figure 3.8 shows that the crack growth rate initially slowed down before increasing with the crack length. Short crack growth rates were shown by Figure 3.10 to be different from that of the long crack growth rates for the same elastic stress intensity range within the initial plastic zone. As the crack grew from the notch (while inside the plastic zone), the growth rates were initially higher. As the crack continued to grow, the rates decreased and increased finally reaching the same levels as that of the long crack, as the crack tip reached the end of the notch plastic zone.

### **3.3 CRACK GROWTH BEHAVIOR OF SINGLE CRYSTALLINE MATERIAL**

Fatigue and creep crack growth behavior of an advanced nickel-base superalloy single crystal were investigated in the temperature range of 870-1094°C (1600-2000°F). The objective of this program was to understand the influence of environment as well as the effect of anisotropy on elevated temperature crack growth behavior. The influence of environment on the fatigue and

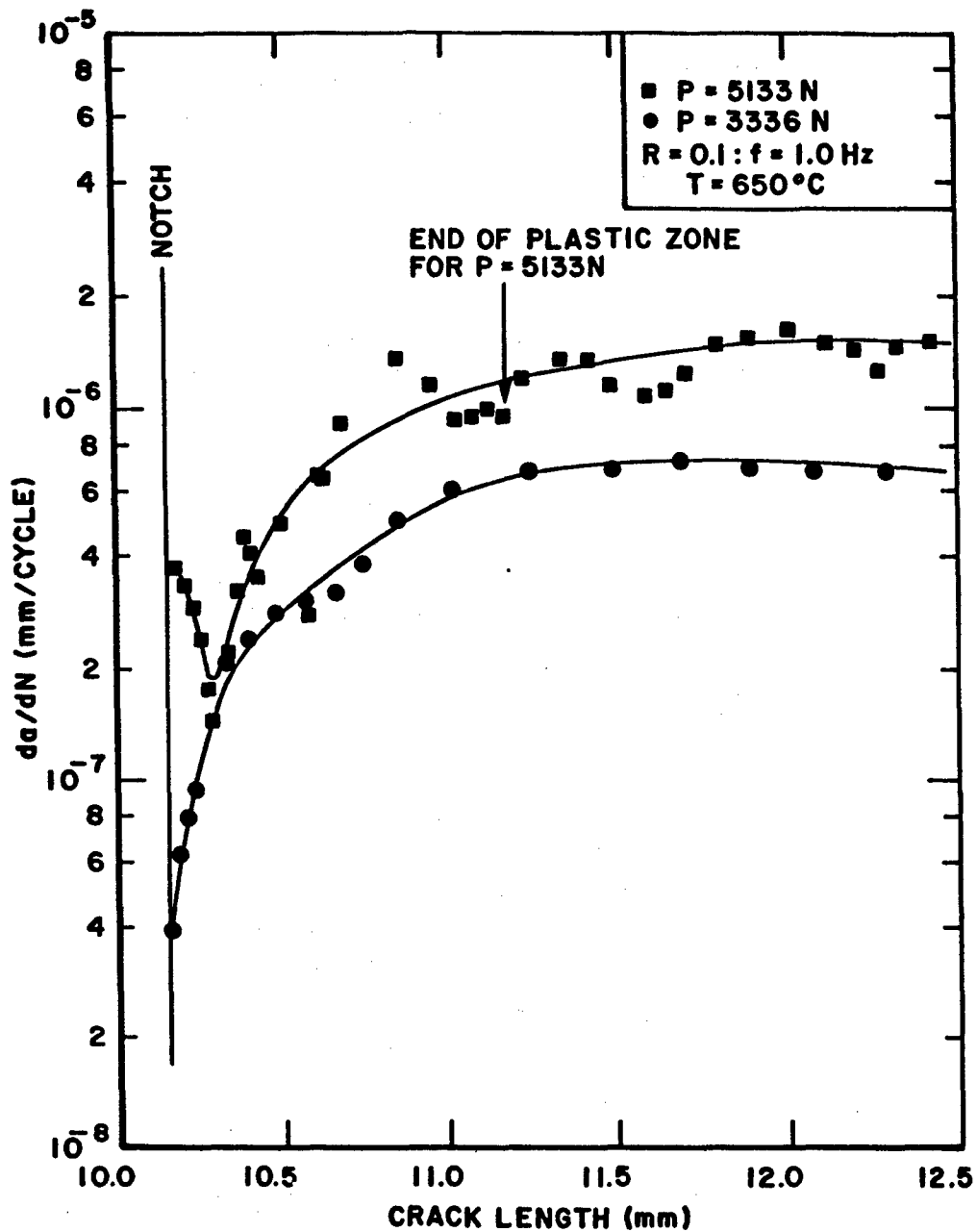


Figure 3.8.  $da/dN$  vs Crack Length Behavior of Cracks Growing from a Notch.

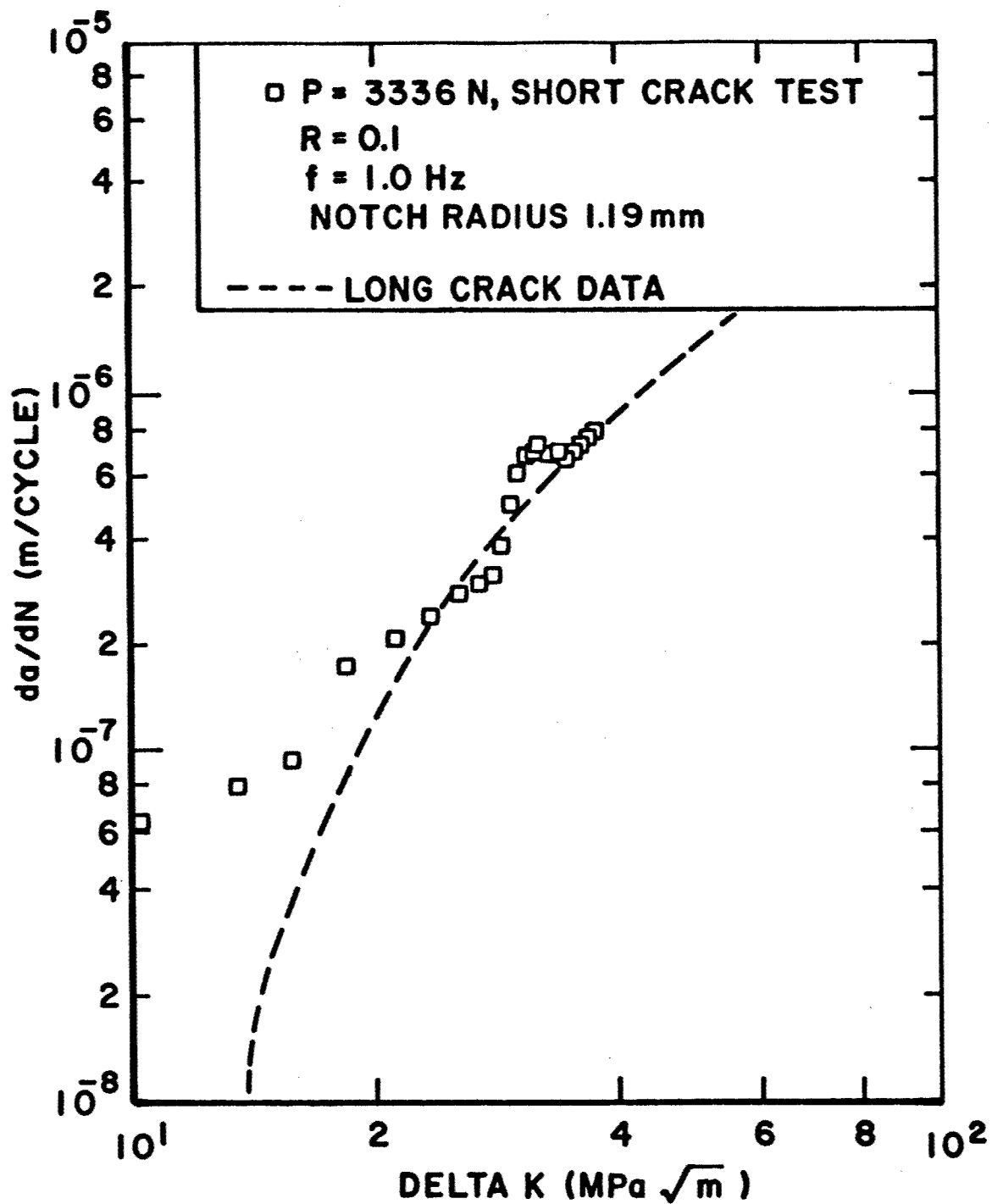


Figure 3.9.  $da/dN$  vs  $\Delta K$  Behavior of Cracks Growing from a Notch (for Small Load of 3336N).

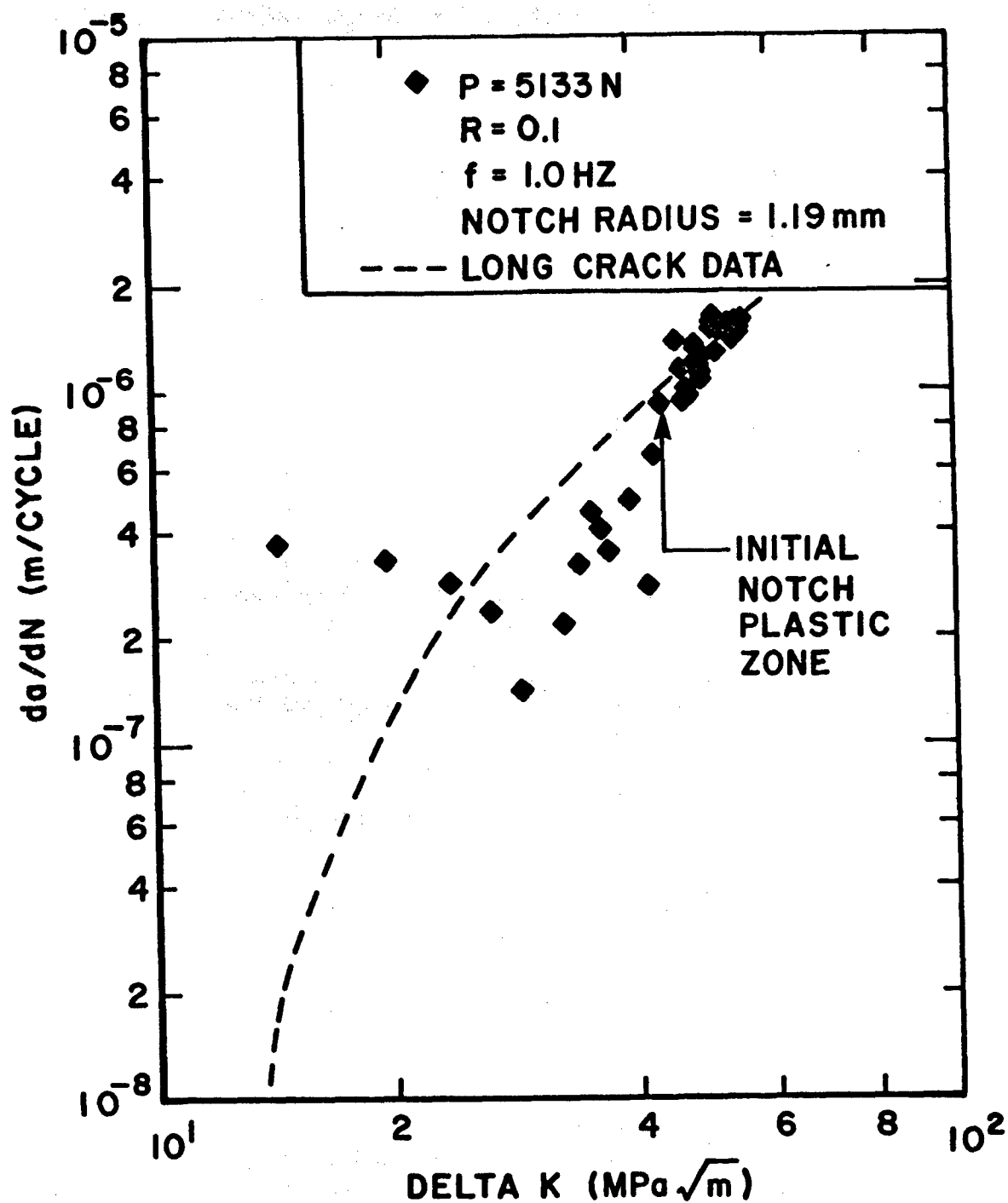


Figure 3.10.  $da/dN$  vs  $\Delta K$  Behavior of Cracks Growing from a Notch (for High Load of 5133N).

creep crack growth characteristics was studied by conducting tests in laboratory air and in a vacuum of  $10^{-5}$  torr. Tests were also conducted with crystal tensile axis and crack growth direction aligned in several orientations to investigate the influence of anisotropy on elevated temperature crack growth behavior. The influence of temperature on the crack growth behavior was studied by analyzing  $da/dt$  vs  $K$  or  $da/dN$  vs  $K$  data. Detailed fractographic analysis were conducted to understand the prevailing mechanism under specific conditions. The details of these results are presented in References 18 and 19.

### 3.3.1 Fatigue Crack Growth in Alloy N4

The effect of crystal anisotropy on the fatigue crack growth has been investigated by conducting constant load fatigue crack growth tests with four crystal orientations of  $\langle 100 \rangle / \langle 010 \rangle$ ,  $\langle 010 \rangle / \langle 100 \rangle$ ,  $\langle 010 \rangle / \langle 101 \rangle$ , and  $\langle 101 \rangle / \langle 010 \rangle$  tensile/crack orientations (the tensile loading axes are parallel to  $\langle 100 \rangle$ ,  $\langle 010 \rangle$ , and  $\langle 101 \rangle$  and crack growth directions are parallel to  $\langle 010 \rangle$ ,  $\langle 100 \rangle$ , and  $\langle 101 \rangle$ , respectively). The effect of crystal anisotropy on fatigue crack growth for the crystal orientations investigated was found to be negligible for tests conducted over the temperature range of  $650^{\circ}\text{C}$  to  $870^{\circ}\text{C}$ . The testing over this wide range of temperatures provided information on the influence of temperature on fatigue crack growth. Detailed fractographic analysis of the failed specimens were conducted to determine the crack growth mechanism. Reference 19 presents the details of this study.

In another series of tests, several experiments were conducted at frequencies of 0.1 and 0.01 Hz to study the effect of frequency. To emphasize the time-dependency aspect, a number of tests were conducted at hold-times of 2, 5, 10, 25, 50, and 500 s. Frequency or hold-time had very little effect on the fatigue crack growth behavior of this alloy at  $870^{\circ}\text{C}$ . The details of this investigation are reported in Reference 20.

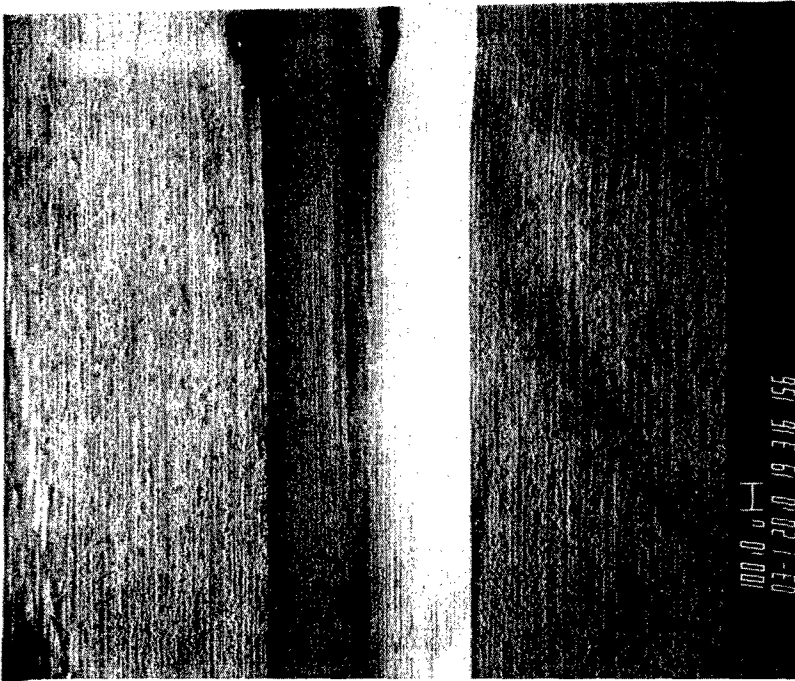
### 3.3.2 Fatigue Crack Growth of Alloy N4 in Vacuum

Fatigue crack growth tests in vacuum of approximately  $10^{-5}$  torr were conducted under temperature and loading conditions similar to those utilized for tests conducted in air. Tests conducted at  $870^{\circ}\text{C}$  indicated a higher crack growth rate in vacuum as compared to laboratory air. However, when the data were plotted as  $da/dN$  vs  $\Delta K_{\text{eff}}$ , the difference in growth rates disappeared and the two curves merged to a single line. Hence, this difference was attributed to an oxide induced closure phenomenon. Threshold tests were also conducted where the influence of environment was expected to be most pronounced. Details of this study were presented in References 19 and 20.

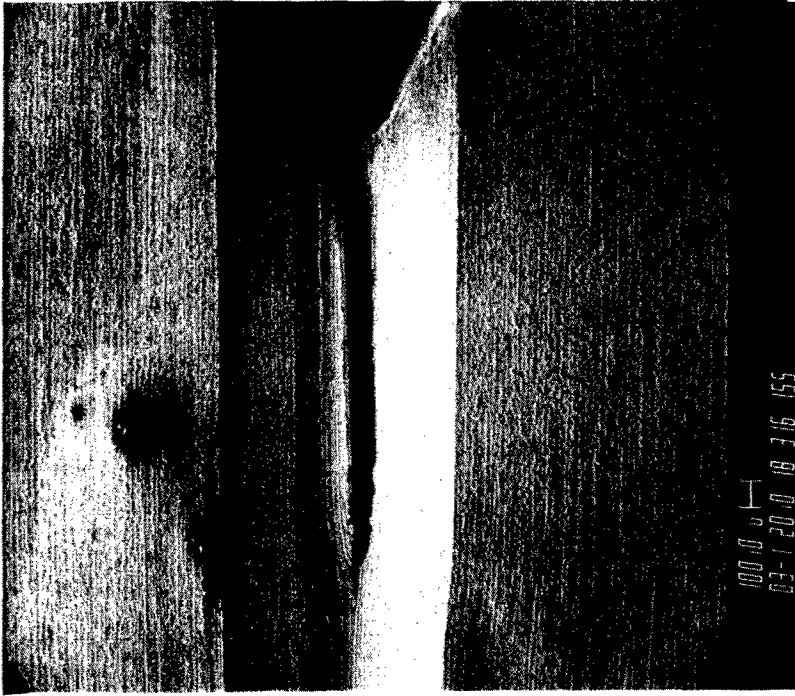
### 3.3.3 Creep Crack Growth (CCG) of Alloy N4 in Laboratory Air

The effect of anisotropy was studied in detail by conducting tests with specimens oriented in  $\langle 100 \rangle / \langle 010 \rangle$ ,  $\langle 010 \rangle / \langle 100 \rangle$ ,  $\langle 101 \rangle / \langle 010 \rangle$ , and  $\langle 010 \rangle / \langle 101 \rangle$  directions. Most of the CCG tests were conducted with side-grooved subcompact tension specimens. In some tests, a phenomenon of crack layering as shown in Figure 3.11 was observed after an initial growth of 50 to 100 mm, resulting in crack arrest. Figure 3.11a shows the extension of crack layering far ahead of the primary crack tip. Figure 3.11b shows the overall crack along with layered cracks. The reason for such crack growth layering is still being investigated. The layering problem was eliminated by increasing the depth of side-groove from 15 to 25% of specimen thickness. Previously, some layering was also observed with side-grooved subcompact IN718 specimens tested at  $540^{\circ}\text{C}$  under static load.

The study of crystal anisotropy on the creep crack growth behavior is a two-dimensional problem. The anisotropy effect is dependent both on the loading direction and the crack growth direction. In this investigation, the effect of anisotropy on creep crack growth behavior was studied by selecting five different combinations of orientations -  $\langle 100 \rangle / \langle 010 \rangle$ ,  $\langle 010 \rangle / \langle 100 \rangle$ ,  $\langle 101 \rangle / \langle 010 \rangle$ ,  $\langle 010 \rangle / \langle 101 \rangle$ , and  $\langle 100 \rangle / 35^{\circ}$



a. Crack Layering Ahead of Crack Tip.



b. Full View Showing the Notch, Precrack, and Crack Layering.

Figure 3.11. Crack Layering.

off from  $\langle 010 \rangle$ . These tests were conducted both in air and vacuum at  $870^{\circ}\text{C}$ . The results of the laboratory air tests are shown in Figure 3.12. It appears that the crack growth rate initially is nearly four to five times higher when the crystal is oriented in  $\langle 010 \rangle / \langle 100 \rangle$  as compared to  $\langle 100 \rangle / \langle 010 \rangle$ . However, this trend reverses at higher  $K_{\text{max}}$  values. Again, the crack growth rate is somewhat higher when the loading axis is changed from  $\langle 100 \rangle$  to  $\langle 101 \rangle$  as shown in Figure 3.12. The slowest growth rate was obtained when the crystals were oriented in  $\langle 010 \rangle / \langle 100 \rangle$  direction. These changes in growth rates are minor and may be well within the scatterband.

#### **3.3.4 Creep Crack Growth of Alloy N4 in Vacuum**

Creep crack growth tests in vacuum were conducted to provide baseline results for evaluating the influence of environment on CCG behavior of alloy N4 single crystals. The vacuum tests were conducted on subcompact tension specimens precracked to an unusually high precrack length of 0.44 inches ( $a/W = 0.52$ ) to obtain a relatively high initial stress intensity value that is within the load capacity of the loading pins and grips. The results of the test conducted on specimens with  $\langle 101 \rangle / \langle 010 \rangle$  orientation in vacuum at  $870^{\circ}\text{C}$ ,  $925^{\circ}\text{C}$ , and  $1093^{\circ}\text{C}$  are shown in Figure 3.13. Results of vacuum tests with other orientations conducted at  $870^{\circ}\text{C}$  have been previously reported [5].

It is noted that the CCG behavior is similar for all orientations when the crack front is parallel to primary dendrite. The general observation is that creep crack growth in vacuum is rapid [18] and occurs at relatively high stress intensities of 45 to  $55 \text{ MPa} \cdot \sqrt{\text{m}}$ . At levels of stress intensity in the range of 35 to  $45 \text{ MPa} \cdot \sqrt{\text{m}}$ , no growth was observed in over 100 hours of testing.

#### **3.3.5 Fracture Surface Analysis of Creep Crack Growth Specimens**

The fracture surface of the alloy N4 specimens tested in air and vacuum were observed under SEM to determine the

LAB AIR @ 1600F

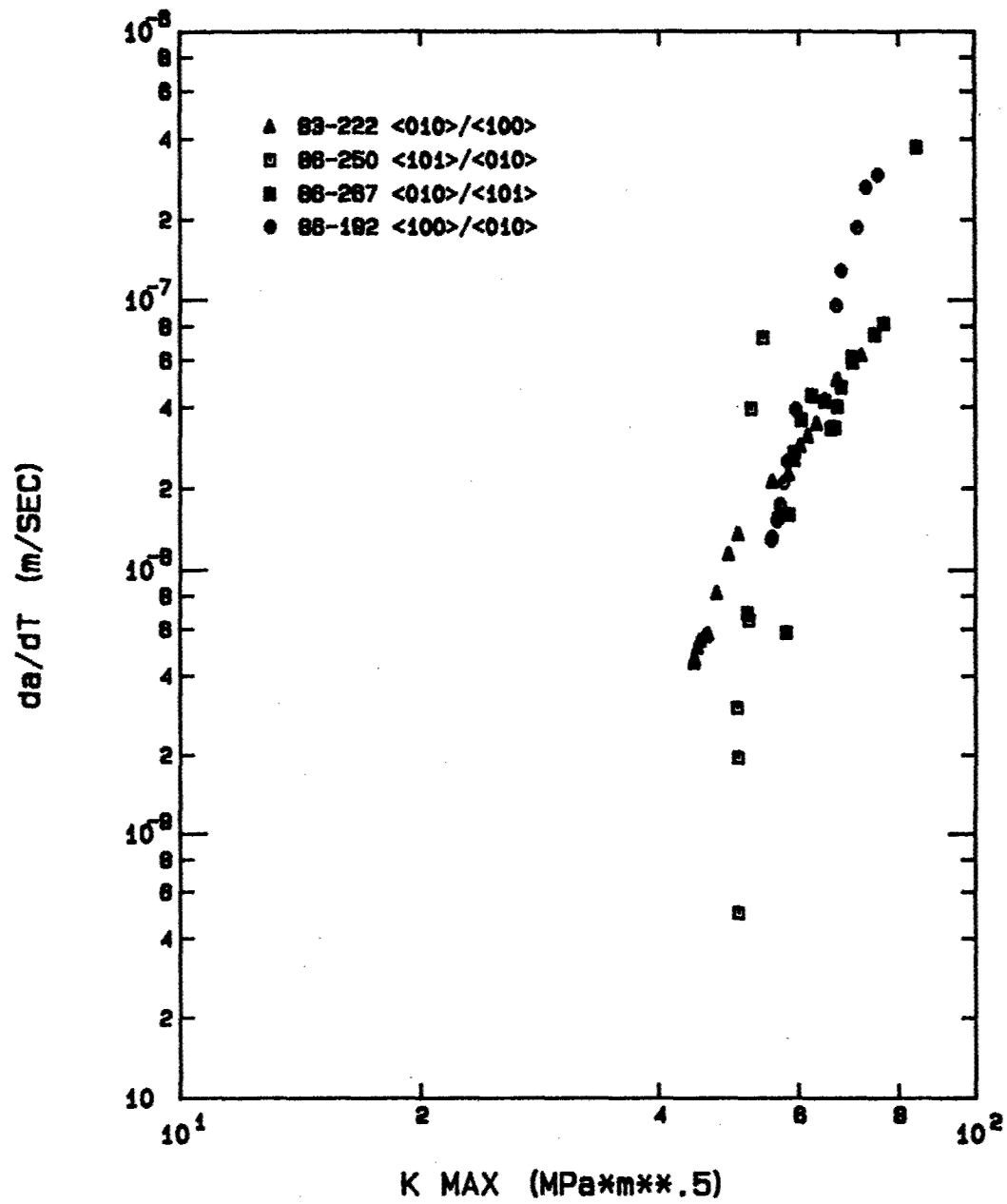


Figure 3.12. Effect of Crystal Anisotropy on Creep Crack Growth.

VAC <101>/<010>

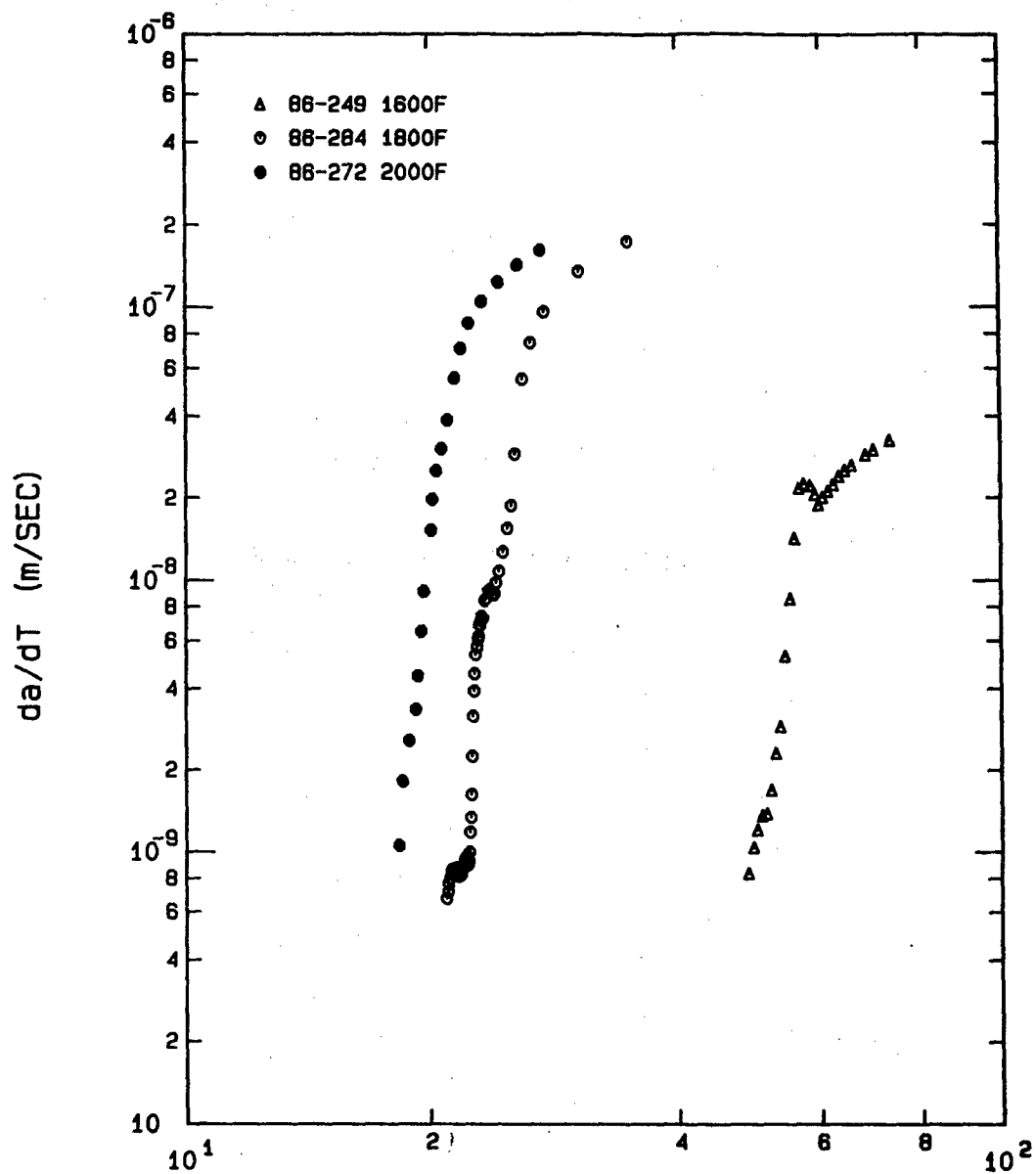


Figure 3.13. Effect of Temperature on the Creep Crack Growth of Rene' N4 Alloy.

failure mechanisms. Figure 3.14 is the fractograph taken from the creep crack growth specimen which was tested in air, which clearly shows an interdendritic failure. Here, the crack follows the interdendritic path, apparently weakened by oxygen diffusion which may embrittle the interdendritic constituents, some of which have higher affinity for oxygen. Further, the diffusion of oxygen is quite fast in this region as compared to the bulk material. Figure 3.15 shows the fracture surface of the creep crack growth specimen in the region where the transition occurs from stable crack growth (interdendritic) to fast fracture (crystallographic). The transition occurs at a growth rate which is above the maximum rate at which data were obtained, which is approximately  $7.5 \times 10^{-8}$  m/s [20]. The crystallographic fracture mechanism, therefore, does not appear until growth rates are above  $7.5 \times 10^{-8}$  m/s. This indicates that the environmental degradation into the material occurs at a rate which is in excess of this crack velocity. Up to this velocity, the growth rates in air and vacuum are significantly different due to the environmental effect and the resultant differences in fracture mechanisms. Only at very high crack velocities would the air and vacuum growth rates be expected to coincide when the velocity is faster than the rate of penetration of oxygen into the interdendritic region ahead of the crack tip.

For the case of specimens tested in vacuum, however, the crack front appears more crystallographic. In this case, the crack path is more homogeneous since there is little difference in the bulk and interdendritic region. There is no weakening of the interdendritic region in the absence of oxygen. In vacuum, a higher stress intensity level is apparently needed to grow the crack, or a slower crack growth rate occurs at the same stress intensity level as compared to the air test. This is evidenced by the fracture surface in Figure 3.16, showing a homogeneous and crystallographic feature with complete absence of interdendritic path. This failure may be termed as transdendritic.

CG Direction

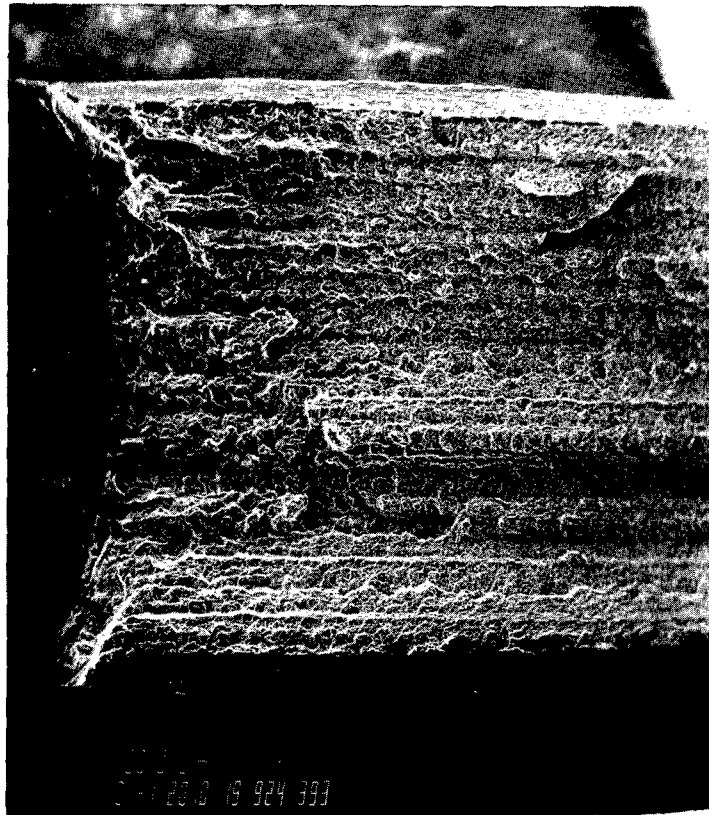


Figure 3.14. Interdendritic Failure.

Crack Growth Direction

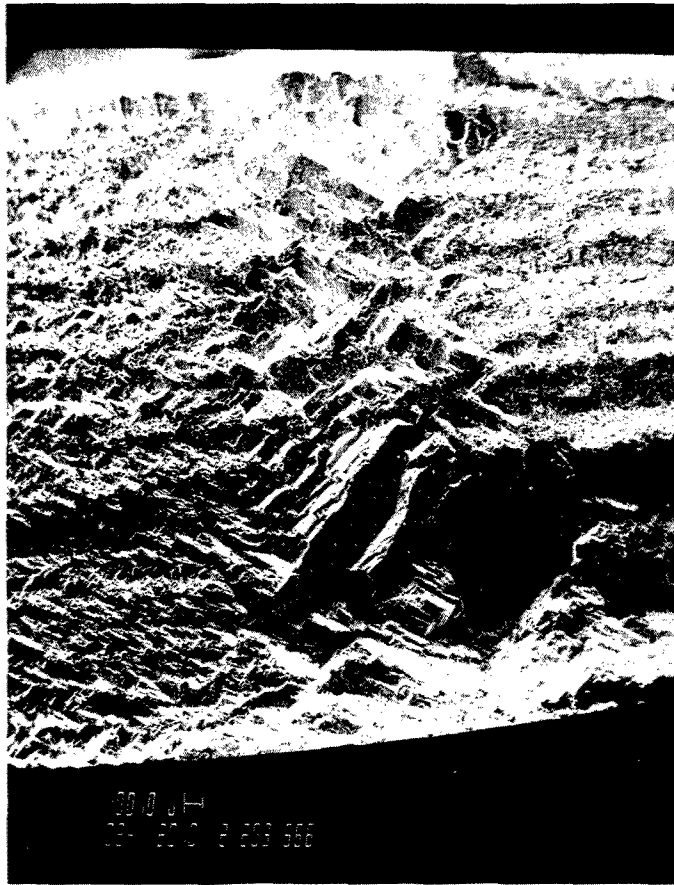


Figure 3.15. Fracture Surface of Specimen Tested in Air, Showing Transition Zone.

Crack Growth Direction

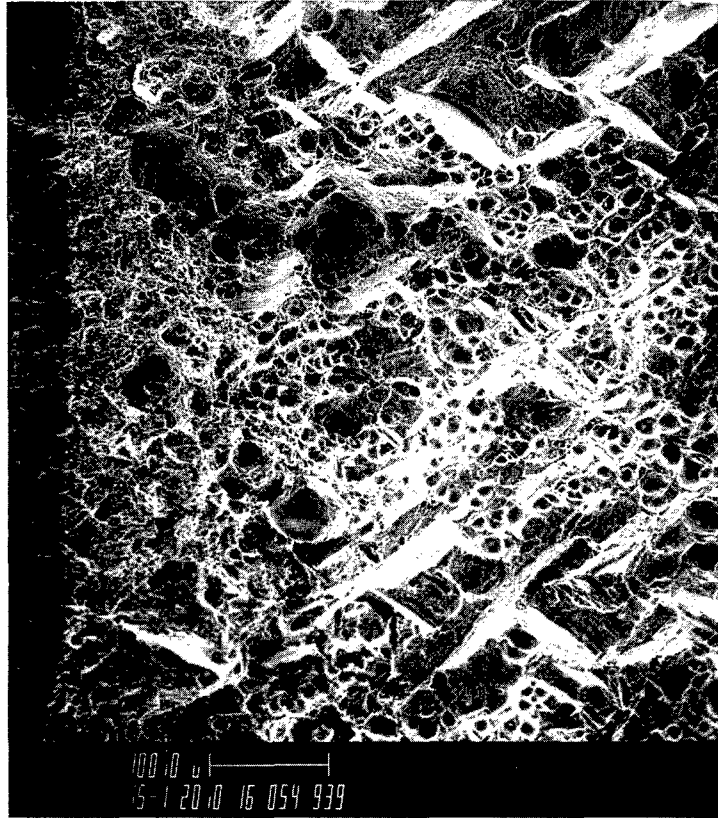
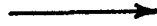


Figure 3.16. Fracture Surface of Specimen Tested in Vacuum, Showing a Small Zone of Transdendritic Failure.

### 3.4 CREEP RUPTURE TESTS

#### 3.4.1 Creep Rupture Tests of Bare and Coated Alloy N4 in Air

Single crystals of gamma prime precipitation hardened Rene' N4 with tensile axis parallel to  $\langle 010 \rangle$  were tested under sustained load in the temperature range of 760°C to 1090°C. The influence of coating was studied by conducting similar tests on bare samples in vacuum. It appears that the coating influences creep rupture life only at higher temperatures by limiting the surface oxidation, since little difference in rupture life was found up to 870°C where oxidation is negligible. The fracture surfaces of the specimens indicated that the initiation of cracks was more or less random. In some cases, the crack initiated from the internal pores, while surface cracks were also found in other specimens. TEM observations showed a complex substructure of stacking faults within gamma prime precipitate along with dislocation networks on the interface. At higher temperatures above 980°C, the shearing was mainly by  $a/2$  [110] dislocations. Details of this work are available in Reference 21.

#### 3.4.2 Microstructure Evaluations of Creep Rupture in Single Crystalline Material

A detailed microstructural evaluation of the creep processes occurring in a single crystalline material over the temperature range of 760°C to 1093°C was conducted through scanning and transmission electron microscopic analysis. The various stages of deformation process and the substructure developed in the primary, steady, tertiary, and rupture regimes were investigated by analyzing the microstructure developed at different amounts of creep strain.

#### 3.4.3 Creep Rupture Tests of Alloy N4

The test results and creep behavior of specimens with the tensile axis parallel to  $\langle 010 \rangle$ , over the temperature range of 760°C to 1093°C have been reported earlier [21].

The surface of creep rupture specimens tested at 870°C, 980°C, and 1093°C under different stresses was observed under optical and SEM microscopes. In some cases, there were indications of the crack initiating from the surface as shown in Figure 3.17, while in other cases, evidence of multiple initiations from the bulk of the specimen was found. The crack in some cases may have initiated through the shrinkage pores as shown in Figure 3.18.

A detailed TEM analysis of these specimens was conducted to investigate the progressive development of substructure with increasing creep strain. A number of sustained load creep tests were conducted at 870°C where the tests were stopped at selected levels of creep strain in the primary, secondary, and tertiary regions to study the development of substructure at different stages of creep. The results of the TEM analysis are discussed in paragraph 3.4.4.

#### **3.4.4 Substructural Analysis of Creep Tested Specimens at 870°C**

Thin foils were prepared from creep specimens tested in air at 870°C to different levels of strain. For comparison, one foil was prepared from undeformed heat-treated material of the same batch of material to evaluate the substructure. The TEM micrograph shown in Figure 3.19 represents the general microstructure of heat-treated Rene' N4 alloy; the figure shows that the undeformed substructure is free of any dislocations.

Figure 3.20a shows the general features of the substructure developed at 0.15 percent strain (in the primary creep strain regions) at 870°C. Notice the presence of dislocations in the matrix and at the interface. Figure 3.20b provides a higher magnification of another representative area showing again that the dislocations are mainly in the matrix surrounding the precipitate, indicating that their movement has been restricted by gamma prime precipitate.

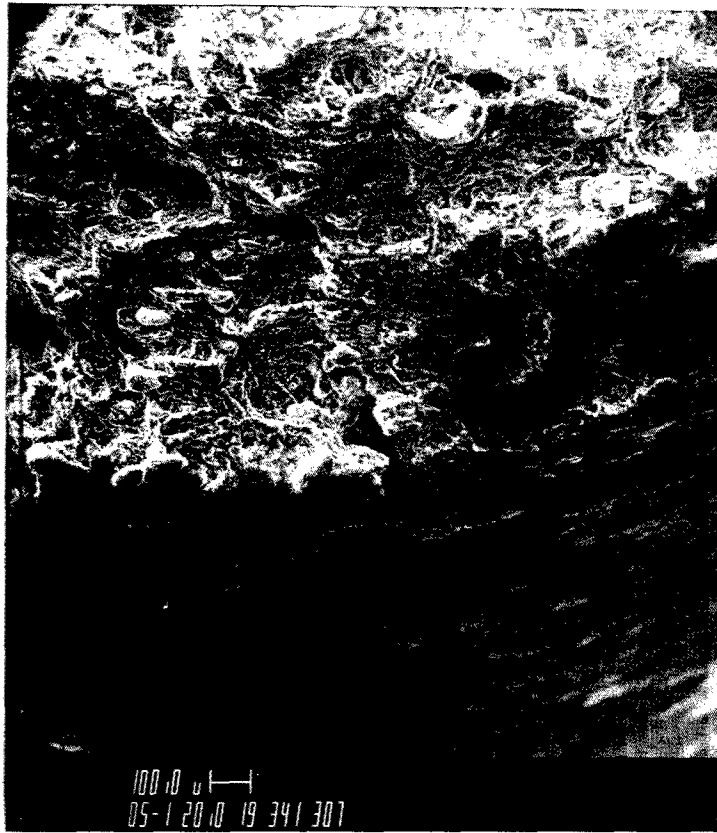


Figure 3.17. Fracture Surface of a Creep Rupture Specimen Showing Crack Initiation from Surface.

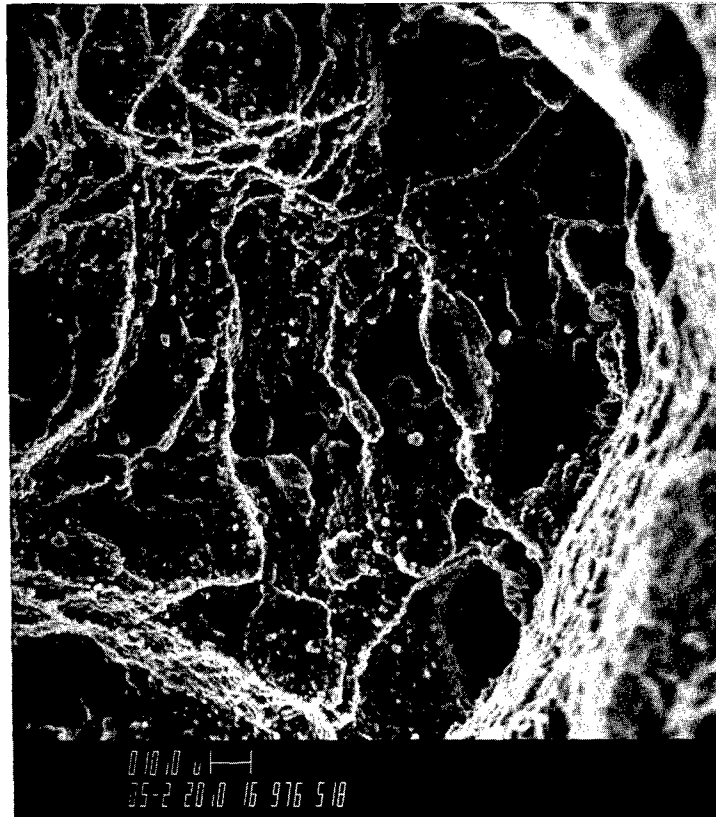


Figure 3.18. Fracture Surface of a Creep Rupture Specimen Showing Shrinkage Pores.

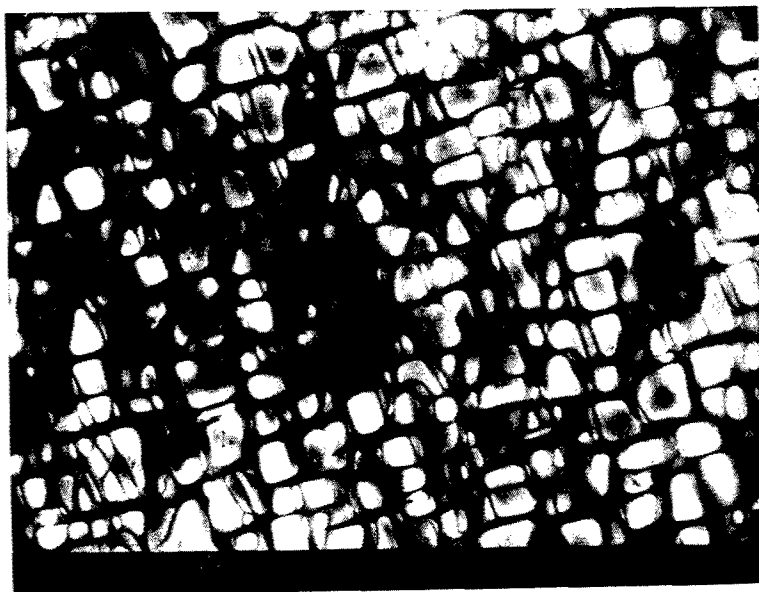
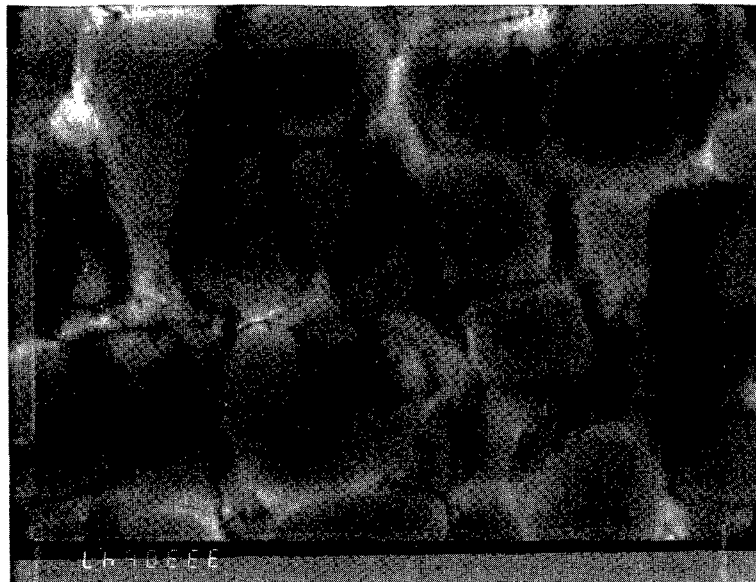
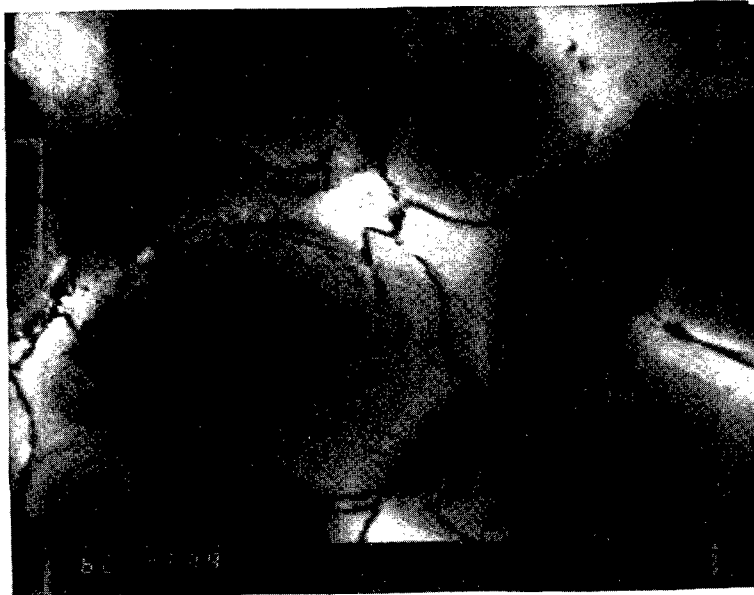


Figure 3.19. TEM Microstructure of Heat-Treated, Rene' N4 Single Crystal.



a. Tested at 870°C (X33000).



b. Notice the Dislocation Surrounding Gamma Prime Precipitate (X66000).

Figure 3.20. Substructure Developed at 0.15% Creep Strain at 870°C.

At a strain of 0.86 percent, which lies in the initial stage of steady-state creep, the development of faults in the precipitate is noticed, as shown in Figure 3.21a. At the same time, with increased strain, dislocation interaction leads to the formation of a dislocation network at the interface, as shown in Figure 3.21b. Some of the dislocations can be seen entering the precipitate, as shown in Figure 3.21c, thus, indicating dislocation movement in both the matrix and precipitate.

The dislocation activity intensifies with increased deformation and the general substructural feature of a specimen strained up to 2.5 percent is shown in Figure 3.22a. The increase in stacking faults as well as dislocation density is clearly noticed. Figure 3.22b provides another TEM micrograph from the same specimen showing a super pair entangled with stacking faults. The shear or cutting of the gamma prime precipitate by a super dislocation is shown in Figure 3.22c. These dislocations were analyzed through the  $g \cdot b = 0$  invisibility criterion (where  $g$  is the reflecting plane vector and  $b$  is the dislocation Burger's vector), and found to be  $a/2 \langle 110 \rangle$  type.

Figure 3.23 shows the substructure developed at very high strain levels of >10 percent, leading to failure. The substructure is very complex; one notices at least two sets of faults, along with the indication of precipitate shearing by  $a/2 \langle 110 \rangle$  super dislocation. Also, there is an intensive network of interfacial dislocation. Although not shown in the micrograph, the development of microtwins was also observed. The complex dislocation structure is indicative of two modes of precipitate shear: one involving the creation of low energy superlattice extrinsic and intrinsic stacking faults by the viscous glide of  $a/3 \langle 112 \rangle$  partial dislocations through gamma prime, and the second involving the cutting of gamma prime particles by constricted  $a/2 \langle 110 \rangle$  dislocation pairs.



a. Stacking Faults with Precipitate (x500000).



b. Dislocation Network at the Interface (x500000).

Figure 3.21. Substructure Developed at 0.86% Creep Strain Tested at 870°C.

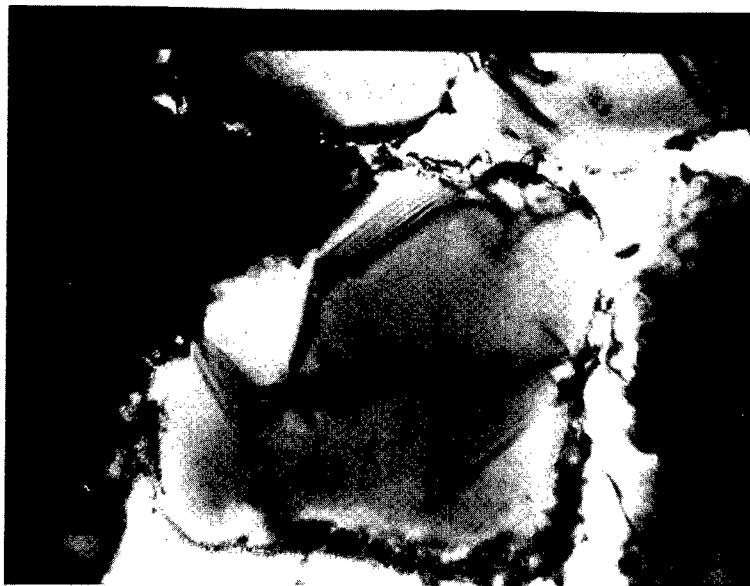


c. Dislocation Migration into Precipitate (X66000).

Figure 3.21 (Concluded). Substructure Developed at 0.86%  
Creep Strain Tested at 870°C.



a. High Density of Stack Fault  
(X33000).



b. Super Pair Entangled with  
Stacking Fault (66000).

Figure 3.22. Substructure Developed at 2.5% Creep Strain Tested at 870°C.



c. Precipitate Shear by Super Pair (X66000).

Figure 3.22 (Concluded). Substructure Developed at 2.5% Creep Strain Tested at 870°C.

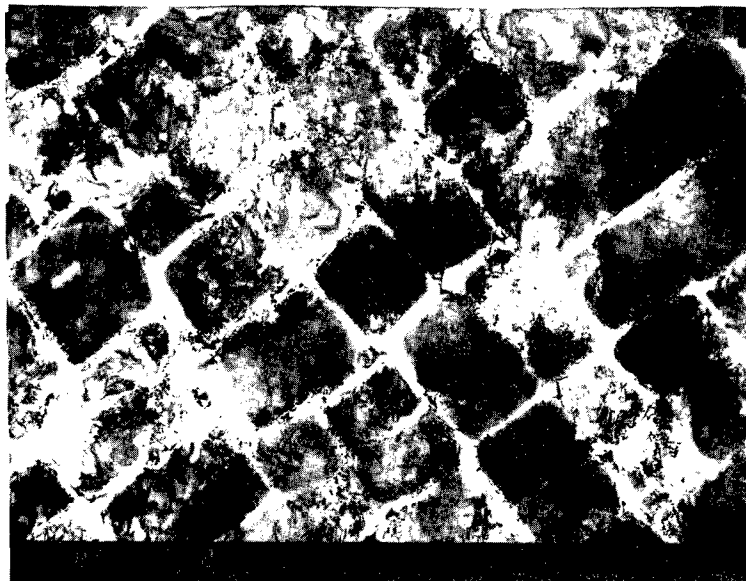


Figure 3.23. Substructure Developed at >10.0% Creep Strain Tested at 870°C (X66000).

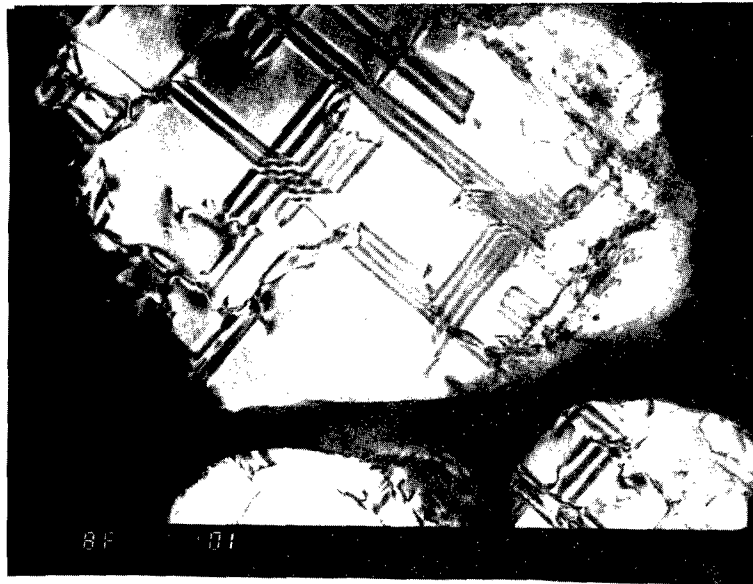
#### 3.4.5 Development of Substructure at 760°C, 870°C, 980°C, and 1093°C

Thin foils were prepared from specimens that experienced creep rupture at 760°C, 870°C, 980°C, and 1093°C under sustained loadings of 700 MPa, 455 MPa, 210 MPa, and 87.5 MPa, respectively, to investigate the difference in creep morphology with temperature. Figure 3.24a is a low magnification (20,000X) TEM micrograph showing heavily faulted structure of the specimen failed at 760°C. Most of the dislocation activity is confined to the precipitate, and the precipitate shear appears to occur by the glide of  $a/3 \langle 112 \rangle$  partial dislocations. The faulted structure can be seen more clearly in Figure 3.24b, where two sets of faults can be easily distinguished. Similar faulted substructure is observed in the foil prepared from specimens failed at 870°C. At 870°C, two sets of microtwins were also observed. One such set of microtwins is shown in Figure 3.25a. Although not as clear, the microtwin activity on the other set of planes is shown in Figure 3.25b. There are some indications that the intersection of such microtwins act as crack nucleation sites. This phenomenon has been observed only at 870°C and it is postulated that the microtwins are formed by a cooperative stacking of faults.

The substructure is somewhat different for specimens tested at 980°F. The formation of cells in these substructures is quite evident as shown in Figure 3.26a, and hardly any fault is noticed. The cell walls are made up of networks of super pairs of  $a/2 \langle 110 \rangle$  dislocations as shown in Figure 3.26b. Such dislocation pairs can be seen within the precipitate also, as discussed earlier. In contrast to the deformation mode at 760°C, where the deformation was controlled by viscous glide of  $a/3 \langle 112 \rangle$  partial dislocation, at 980°C the deformation mode is predominantly controlled by the glide of super  $a/2 \langle 110 \rangle$  dislocation pairs, see Figure 3.26c. At the intermediate temperature of 870°C, both shear modes are operative.

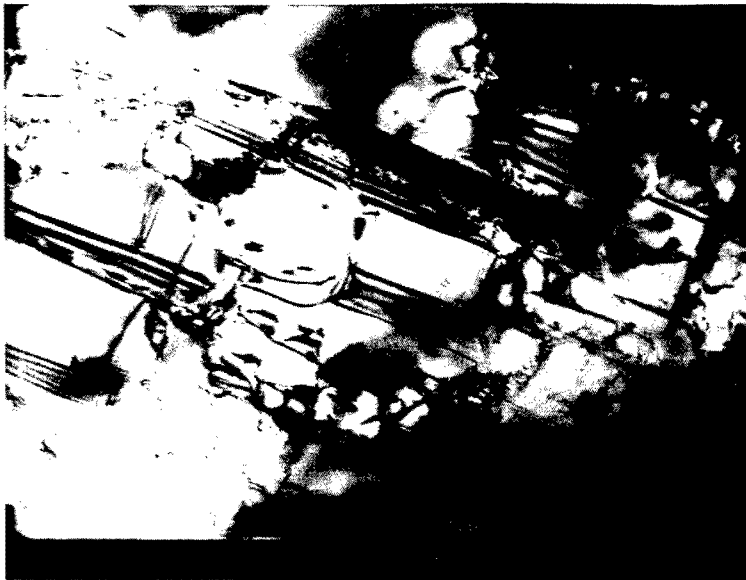


a. High Density of Faults.



b. Two Sets of Faults in the Precipitate.

Figure 3.24. Substructure Developed in the Creep Ruptured Specimen at 1400°F.



a. Indication of Microtwin  
Formation from Stacking Faults.

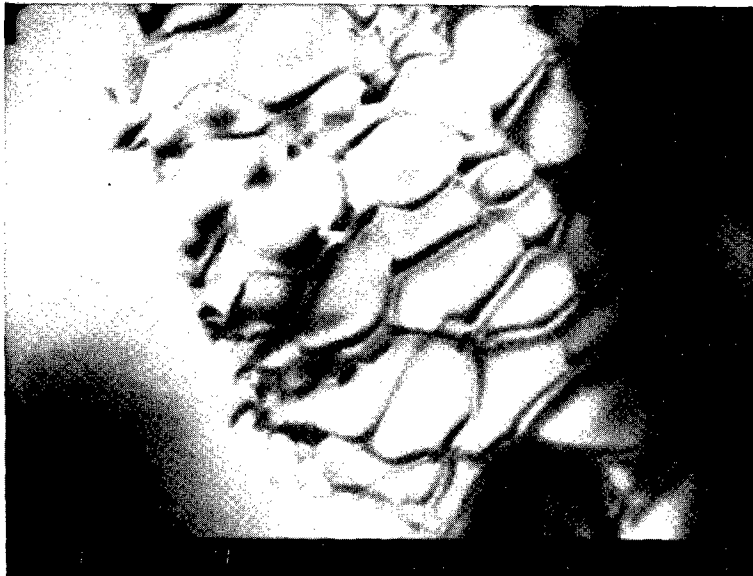


b. Two Sets of Intersecting  
Microtwins.

Figure 3.25. Substructure Developed in Creep-Ruptured Specimen at 870°C.

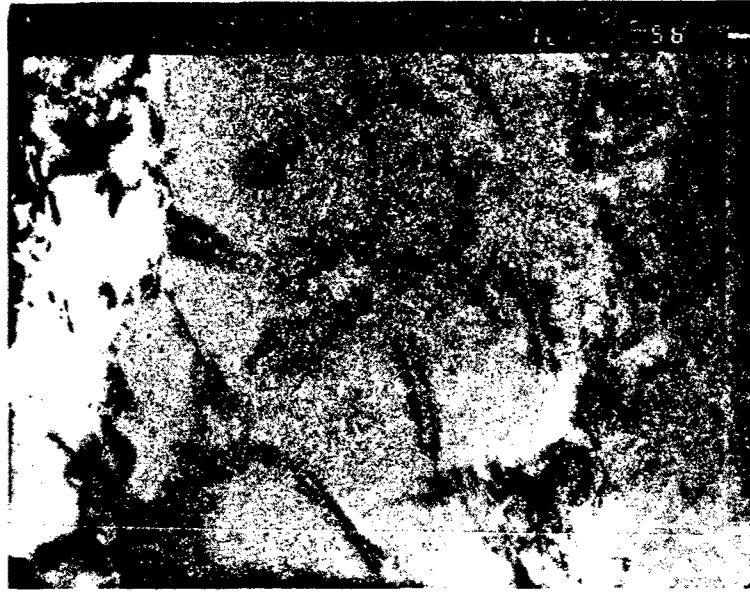


a. Cell Structure.



b. Network of Super Pair Dislocation.

Figure 3.26. Substructure Developed in Creep-Ruptured Specimen at 870°C.



c. Super Pair Dislocation in Precipitate.

Figure 3.26 (Concluded). Substructure Developed in  
Creep-Ruptured Specimen at  
870°C.

The higher temperature of 1093°C leads to the unstability of precipitate structure itself and formation of creep cell structures even within the precipitate is observed, as shown in Figure 3.27a. The deformation cell is more clearly shown in Figure 3.27b, while Figure 3.27c shows the development of cell walls within a precipitate. The cell wall here is composed of  $a/2 \langle 110 \rangle$  super dislocation pairs. Figure 3.27d is a higher magnification micrograph of such a cell wall showing the interaction of super  $a/2 \langle 110 \rangle$  dislocation pairs.

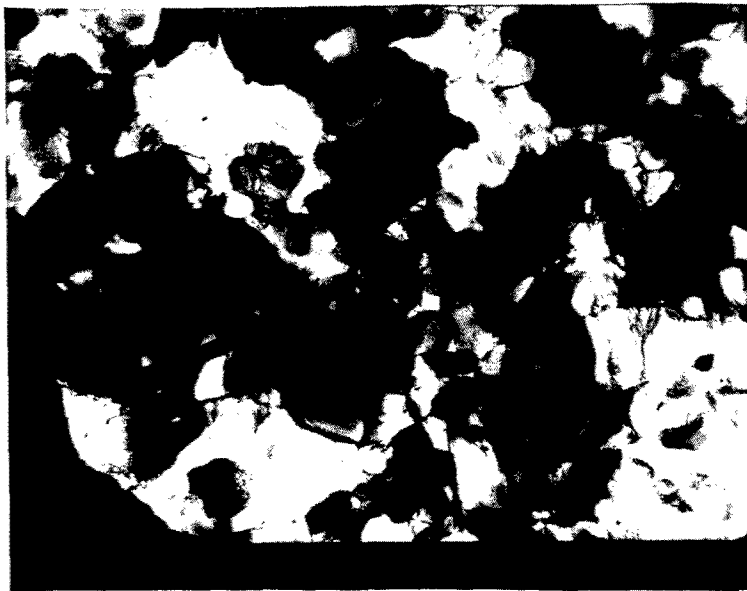
### 3.5 HOT CORROSION TESTS

Certain "environmental conditions" of stress, temperature, and contaminants have been shown to produce crack damage and mechanical property changes in many metallic materials. The nature and the mechanisms of degradation of physical and mechanical properties are dependent on these conditions. The stress plays a major role in degradation of mechanical properties of certain materials under a specific combination of environment. Hot corrosion attack is particularly severe in the temperature range of 700-900°C and is expected to be accentuated by the presence of stress.

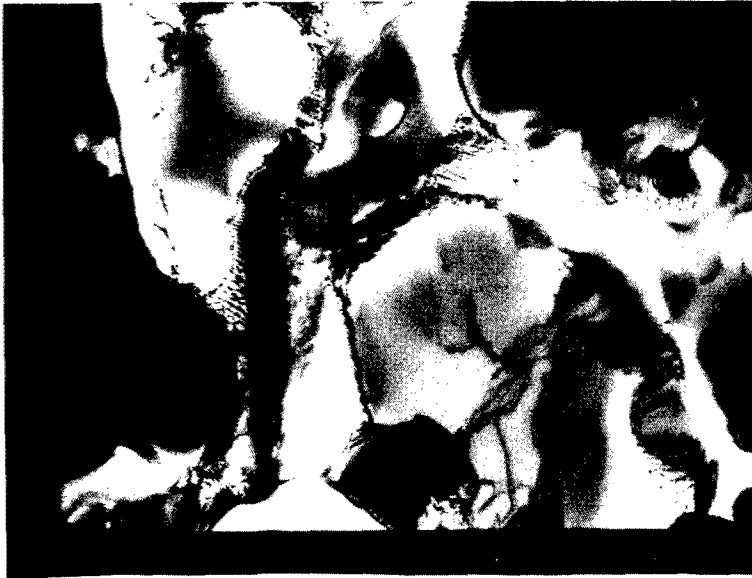
Very limited information is available on the role that stress plays on the hot corrosion behavior of Ni-base superalloy. Standard hot corrosion tests were also conducted to provide baseline data and compare results with experiments conducted under the influence of load.

#### 3.5.1 Effect of Hot Corrosion on Creep Rupture Life of IN718

The objective of this study was to examine the effect of stress in the hot corrosion process and the microstructural changes and mechanisms which occur during corrosion-mechanical property interactions. Sustained load creep tests were conducted at a temperature of 800°C (1472°F) in laboratory air at stress levels in the range of 70 MPa to 210 MPa. Smooth, round tensile specimens were coated with a 90%



a. Cell Structure.



b. High Magnification of Cell Structure.

Figure 3.27. Substructure Developed in Creep-Ruptured Specimen at 1093°C.



c. Cell Development Within  
Precipitate.



d.  $a/2 \langle 110 \rangle$  Super Pair in Cell  
Wall.

Figure 3.27 (Concluded). Substructure Developed in Creep-Ruptured Specimen at 1093°C.

Na<sub>2</sub>/SO<sub>4</sub>/10% NaCl salt mixture by spraying heated specimens with an aqueous salt solution. Results of tests conducted with salt coated specimens were compared with tests conducted with uncoated specimens. Specimens were subsequently sectioned, and a detailed metallographic analysis of the hot corrosion attack was conducted. Creep data showed a degradation in the creep resistance of IN718 due to the presence of the molten salt environment. The degradation was primarily due to oxide penetration into metal which had been depleted of alloying elements and subsequent cracking along oxide-metal interfaces.

### **3.5.2 Effect of Hot Corrosion on Creep Rupture Life of Rene' 77 and Rene' 80**

A study was initiated to study the effect of hot corrosion on creep rupture life of alloy Rene' 77 and Rene' 80. Specifically, the objective was to investigate the effect of stress and load history on the hot corrosion process, and the microstructural changes and mechanisms which occur during corrosion-mechanical property interactions. Sustained load creep tests using smooth, round bar specimens were conducted at temperatures of 800°C and 1000°C at stress levels ranging from 105 MPa to 525 MPa. Specimens were coated with a thin film of 90% Na<sub>2</sub>SO<sub>4</sub>/10% NaCl solution to obtain the hot corrosion environment at elevated temperature. Results of tests conducted with salt coated specimens were compared with tests conducted with uncoated specimens. A successful attempt has been made to correlate stress level, temperature, and environmental damage as measured by depth of penetration to examine the effect of stress on environmental attack. Details of this study are available in Reference 22.

### **3.5.3 Effects of Stress and Stress History on Environmental Attack in Rene' 80**

An investigation was conducted to investigate the influence of stress and stress history on environmental degradation. The study addressed the environmental attack under various combinations of sustained and cyclic loading in order to determine the roles that stress and stress history play in the

high temperature environmental degradation of a representative gas turbine engine material.

The material used in this study was a turbine blade nickel-base superalloy, Rene' 80. To study the influence of stress on environmental degradation, sustained-load creep tests were conducted using smooth, round bar tensile specimens. Tests were conducted at 900°C in two environments, laboratory air and a 90% Na<sub>2</sub>SO<sub>4</sub>/10% NaCl molten salt mixture. All tests were carried to failure, and the specimens were then sectioned below the necked region of the failure. The cross-sections were metallographically prepared for SEM analysis. The environmental attack was characterized and the cause and sites of crack initiation were identified. The depth of attack was determined by measuring the amount of sound metal along diameters in the cross-section plane. Results showed increasing depths of environmental attack with increasing stress levels in both environments. The depths of environmental attack which led to cracking were significantly greater than that for specimens tested in an unstressed condition. Oxide layers formed during sustained load testing in laboratory air were generally adherent and protective. Surface layers formed during sustained load testing in molten salt films were porous, non-adherent, and apparently non-protective.

In order to assess the role of stress history, tests were conducted under sustained load with periodic superimposed cyclic unloading (creep-fatigue) where cracking of the surface oxide layer is likely. The creep-fatigue interaction was studied by conducting tests using different time intervals, from zero (pure fatigue) to 900 seconds, between the unloading-reloading fatigue cycle which contributes to surface oxide cracking. The results of these tests are discussed in Reference 23.

#### **3.5.4 Hot Corrosion in Alloy Rene' 77 and Rene' 80**

Static hot corrosion tests on specimens of Rene' 77 and Rene' 80 were conducted. Cylindrical pins were salt coated

and tested for 72 hours at a temperature of 900°C (1652°F) in laboratory air. Weight change calculations and measurements of the depth of corrosion attack were made; a metallographic analysis was conducted. The test procedure and results are discussed in Reference 24.

## SECTION 4

### ANALYTICAL DEVELOPMENTS

#### 4.1 BACK-FACE STRAIN ON SE(T) GEOMETRY

A finite element analysis was conducted to determine the theoretical back-face strain (BFS) values for 0.2 to 0.8 crack length to width ratios of a pin loaded single edge notched, SE(T), specimen. As a result of a previous analysis of an SE(T) specimen, initial meshes had been developed with 104 elements and 356 nodes for the JA code [25]. The meshes incorporated eight (8) triangular elements having quarter point nodes and common vertices at the crack tip to simulate the  $\sqrt{r}$  singularity. Due to symmetry, only half of the SE(T) specimen was modeled.

The strain calculated on the back-face (opposite of the notch) was used to determine a polynomial fit for a relationship between BFS compliance (ratio of strain divided by load,  $C_e$ ) and crack length ratio ( $a/W$ ). This relationship provides the basis for an automated crack growth control program to determine crack length from BFS compliance.

#### 4.2 ANALYSIS OF DISK-SHAPED COMPACT SPECIMEN

A finite element analysis was conducted on a disk-shaped compact specimen DC(T) to determine crack mouth opening displacement (CMOD) and back-face strain for a range of crack lengths. A mesh generation program was developed to generate the input values for crack length to width ratios from 0.25 to 0.8. The finite element code use for the analysis was SNAP [26].

A typical mesh for the DC(T) specimen with  $a/W = 0.5$  is shown in Figure 4.1. Special triangular elements with quarter point nodes have been used to simulate the  $\sqrt{r}$  singularity around the crack tip. The results for the stress intensity factor as a function of crack length compare favorably with values given in the published literature.

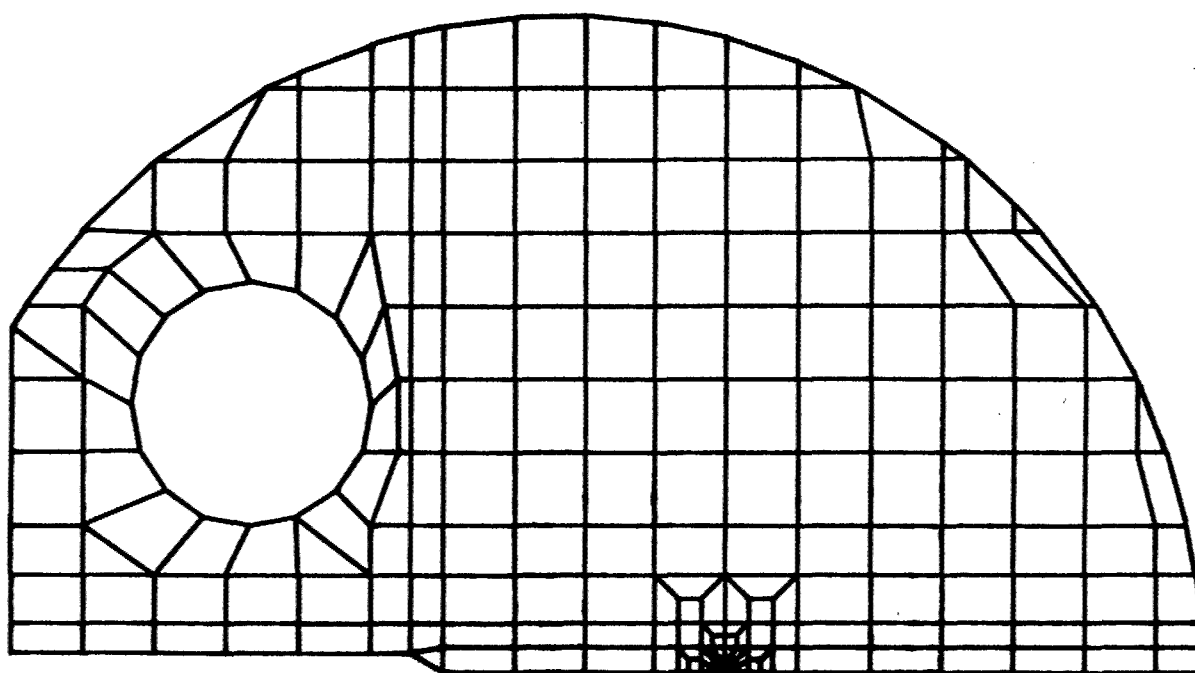


Figure 4.1. Mesh for Finite Element Analysis of DC(T),  $a/W = 0.5$ , Specimen.

From the finite element results for the CMOD and BFS, relationships were established for the crack length as a function of the CMOD compliance and of the BFS compliance. Then, these relationships were incorporated into the software for the automated crack growth control of DC(T) specimens.

#### **4.3 THREE DIMENSIONAL ANALYSIS OF CURVED CRACK FRONT**

A three dimensional analysis of a curved crack front was initiated using a code based on the alternating finite element technique [27]. Problems in the code developed during the analysis of a nearly straight through-the-thickness crack in a ring specimen. An input file has been generated for a benchmark problem which has been analyzed and reported in the literature. The code will be operated with the benchmark data and the results will be compared to the published values. Subsequently, the problems with the input for the original geometry will be investigated.

#### **4.4 VALIDATION OF BODNER-PARTOM ROUTINES IN SNAP**

The purpose of this task was to validate a computer algorithm to describe material response using the Bodner-Partom (B-P) constitutive Equation [28] in the "SNAP" finite element program [26]. The validation scheme involved the comparison of cyclic stress-strain response computed by SNAP with the response calculated from the direct solution of B-P equations.

For a trial problem, a tensile strip specimen subjected to cyclic loads was chosen. The corresponding finite element model of the tensile specimen is shown in Figure 4.2. The specimen was modeled with six triangular elements and eight nodes. A cyclic loading with a peak load of 200 kips at 0.167 Hz and R (minimum load/maximum load) of -1.0 as shown in Figure 4.3 was applied to the specimen. The B-P model parameters and equations used in the SNAP simulation are given in Table 4.1.

Solutions were carried out for five full cycles. For loads below the peak load, the solution converged within two or three

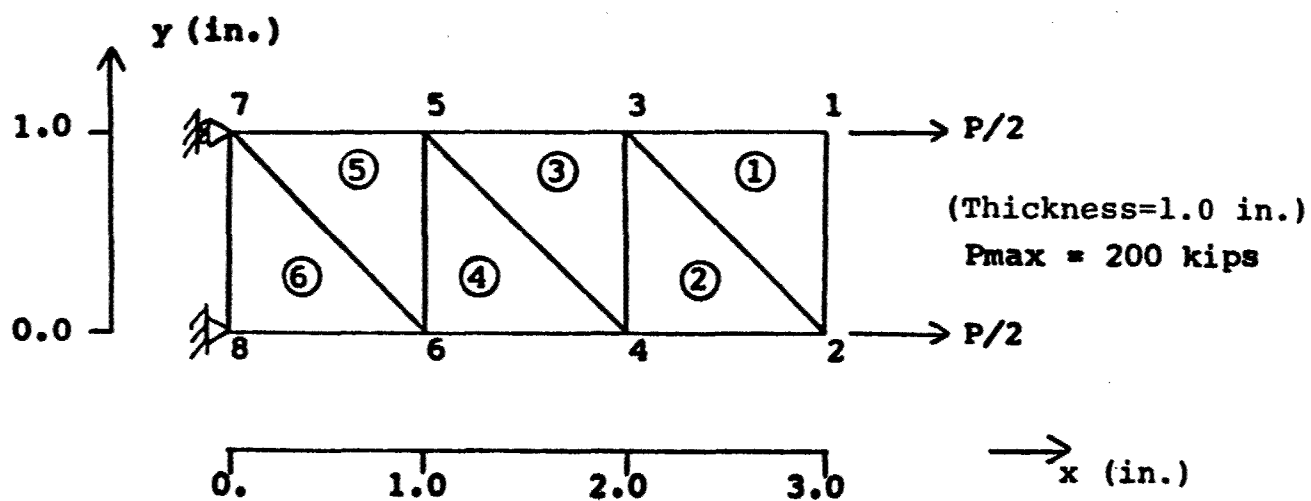


Figure 4.2. Finite Element Model of a Tensile Strip Specimen.

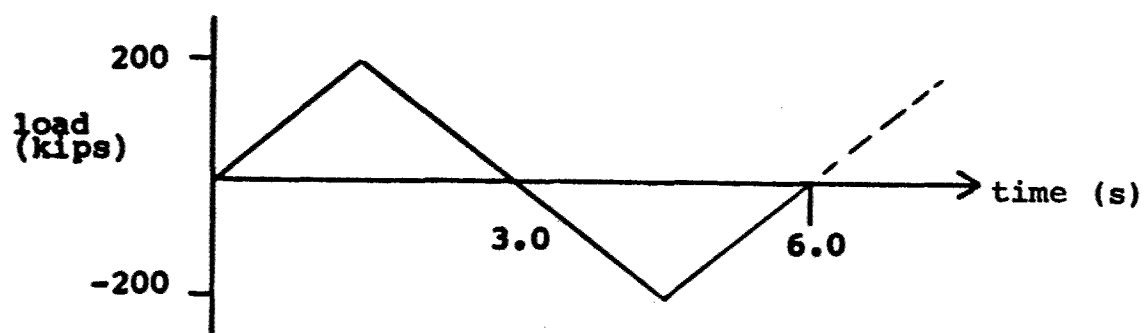


Figure 4.3. Loading Cycle.

TABLE 4.1

PARAMETERS FOR THE BODNER-PARTOM  
CONSTITUTIVE EQUATIONS  
(REFERENCE 24)

$$D_0 = 10^4 \text{ s}^{-1}$$

$$n = 0.7$$

$$m = 2.57 \text{ (ksi)}^{-1}$$

$$Z_0 = 915 \text{ ksi, (Initial Value for Z)}$$

$$Z_1 = 1015 \text{ ksi}$$

$$Z_2 = 600 \text{ ksi}$$

$$A = 0.0018 \text{ s}^{-1}$$

$$r = 2.66$$

$$Q = \begin{array}{l} 1, \text{ Fully Isotropic Flow} \\ 0, \text{ Fully Anisotropic Flow} \end{array}$$

Constitutive Equations

$$\dot{\epsilon}^P = \frac{2}{\sqrt{3}} D_0 e^{-\left(\frac{n+1}{2n}\right) (Z/\sigma)^{2n}},$$

$$\dot{Z}^+ = [Q + (1-Q) \frac{\sigma}{|\sigma|}] \dot{Z} \text{ for tension,}$$

$$\dot{Z}^- = [Q - (1-Q) \frac{\sigma}{|\sigma|}] \dot{Z} \text{ for compression,}$$

$$\dot{Z} = m(Z_1 - Z) \dot{W}_P - AZ_1 \left(\frac{Z - Z_2}{Z_1}\right)^r,$$

$$\dot{W}_P = \sigma \dot{\epsilon}^P$$

iterations. Around the peak load, four to seven iterations were required for convergence. In general, the convergence was reasonably fast during the five cycles of loading. The cyclic stress-strain curve saturated at the second loading cycle as shown in Figure 4.4. This curve computed by SNAP was directly compared with the results obtained from the direct solution of the B-P equations. The SNAP results compared extremely well with the direct solution (see Figure 4.4) and the difference was less than one percent. The present results validate the B-P model algorithm in SNAP for its accuracy and numerical efficiency.

#### 4.5 COMPLIANCE EXPRESSIONS FOR C(T) SPECIMENS

Two empirical equations were developed that express displacement across the crack in a compact type C(T) specimen as a function of crack length and distance behind the crack tip. The coefficients in the equations were generally determined by least square procedures where the equations were fitted to crack surface displacements obtained from finite element analysis. One expression utilized simple types of functions which depended on either crack length or distance from the crack tip; these functions were combined to form an equation that is similar to a series expansion in two separate variables. The second equation was developed from a combination of the far field behavior of the displacements and a near field fit which incorporates the near-tip analytical displacement behavior.

Both equations have application to a broad range of values of both crack length and distance from the crack tip. Either equation can be used in conjunction with measurements of displacement across the crack surface to indirectly determine the crack length. This effort is detailed by Reference 29.

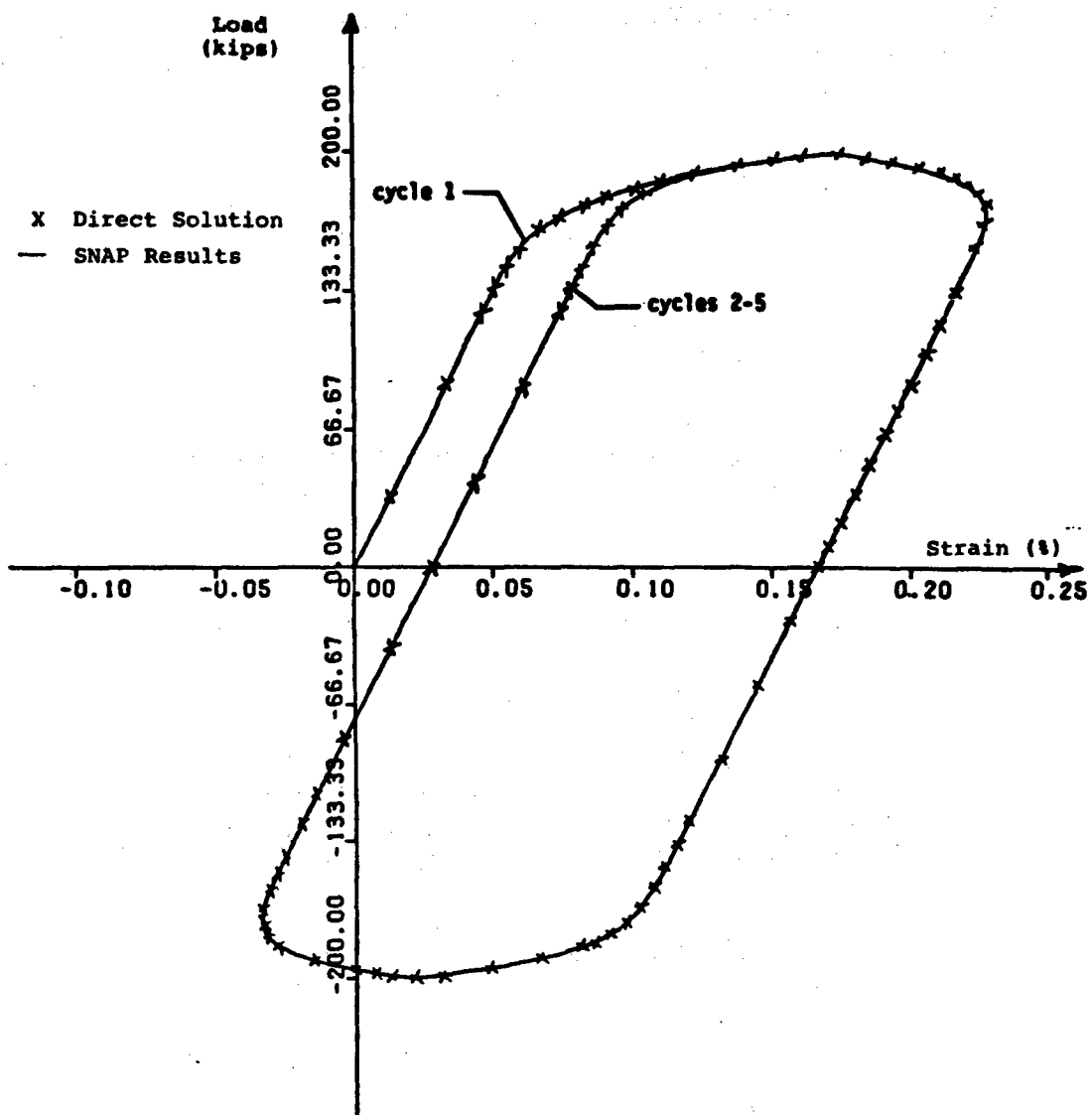


Figure 4.4. Comparison Between the SNAP and the Direct Solutions for the Cyclic Loading Response.

## **SECTION 5**

### **DATA MAINTENANCE AND TEST SUPPORT ACTIVITIES**

As an essential part of our research activity, a procedure was developed in which all the data generated in the laboratory is transmitted to a central HOST computer for manipulation and storage. This system was continuously maintained and updated. In this program, various types of mechanical tests were also conducted to support the material characterization research activities of other branches.

#### **5.1 DATA TRANSMISSION AND STORAGE**

The data generated in the laboratory is transmitted to the central laboratory HOST computer for manipulation and storage. The transmission can be made via a number of serial RS-232 communication ports attached to various microcomputers at the test stations. A set of data manipulation, reduction, and plotting routines are maintained on the HOST computer (PDP 11/24) for general use. In addition, cartridge tape and removable hard disk media archival facilities are available for all users. All critical data and software, including the system software, are backed up on both tape and disk.

#### **5.2 MLLS BRANCH TEST SUPPORT ACTIVITIES**

Various tests were conducted in the laboratory to provide basic mechanical property data on existing and developmental materials. The procedures set forth in the ASTM Standard Test Methods were followed for these tests unless otherwise specified by the engineer/scientist.

The types of tests that have been performed during the past year are fatigue crack growth at room temperature, axial fatigue at room temperature, fracture toughness at room temperature, and tensile tests from room temperature to 316°C. These tests were performed on numerous alloys of aluminum and titanium. After

each test, the data were analyzed, documented, and reported to the respective project engineer.

### **5.3 ELECTRONICS FABRICATION AND REPAIR**

The nature of the material tests performed within the laboratory periodically requires the development and implementation of electronic equipment and interfaces which are not generally available through commercial vendors. Laboratory electronics personnel are encouraged to maintain a current knowledge of their field to provide new or innovative solutions to electronic measurement or control problems as required. Several electronics packages have been developed in house, including:

- Linear Array Interface Electronics
- Linear Array Power Supplies
- VIC-20 Instron Major/Minor Interlocks
- VIC-20 C20 Interfaces

The primary objective of the contract electronics repair operation was to identify the specific symptoms and if possible, the malfunctioning component. Complicated repair operations were referred to the Base PME section for completion. This arrangement proved to be efficient for the contract personnel and the PME section.

## APPENDIX A

### IBM AT SYSTEM

A block diagram of the control system is illustrated in Figure A1. The functions of the equipment which is connected on the IEEE-488 bus and parallel bus are described below.

- Printer - Prints the data samples.
- Cycle Counter - Counts the number of cycles by monitoring the load or function generator signal.
- Nicolet Digital Oscilloscope - Digitizes and displays load and displacement amplifier signals. The disk drive in the oscilloscope is used to store the load displacement waveform when high speed data acquisition is required. Compliance of the test specimen is computed from the digitized load displacement data. The ability to trigger at a given point of waveform reduces the software development time for complicated waveforms.
- HP Voltmeter - Acquires mean values of electric potential of the cracked specimen.
- HP Power Supply - Supplies a constant current of 9.5A across the cracked specimen. The power supply is switched off by the computer in acquisition of thermal EMF.
- Wavetek Function Generator - Provides the reference load signal to the hydraulic machine. By mixing the four programmed RAM waveforms and clock with interruptable capability, very complicated engine spectra can be created. A trigger signal can be obtained at predetermined positions of the waveforms.

The following capabilities are available from a card that is connected to the IBM internal bus:

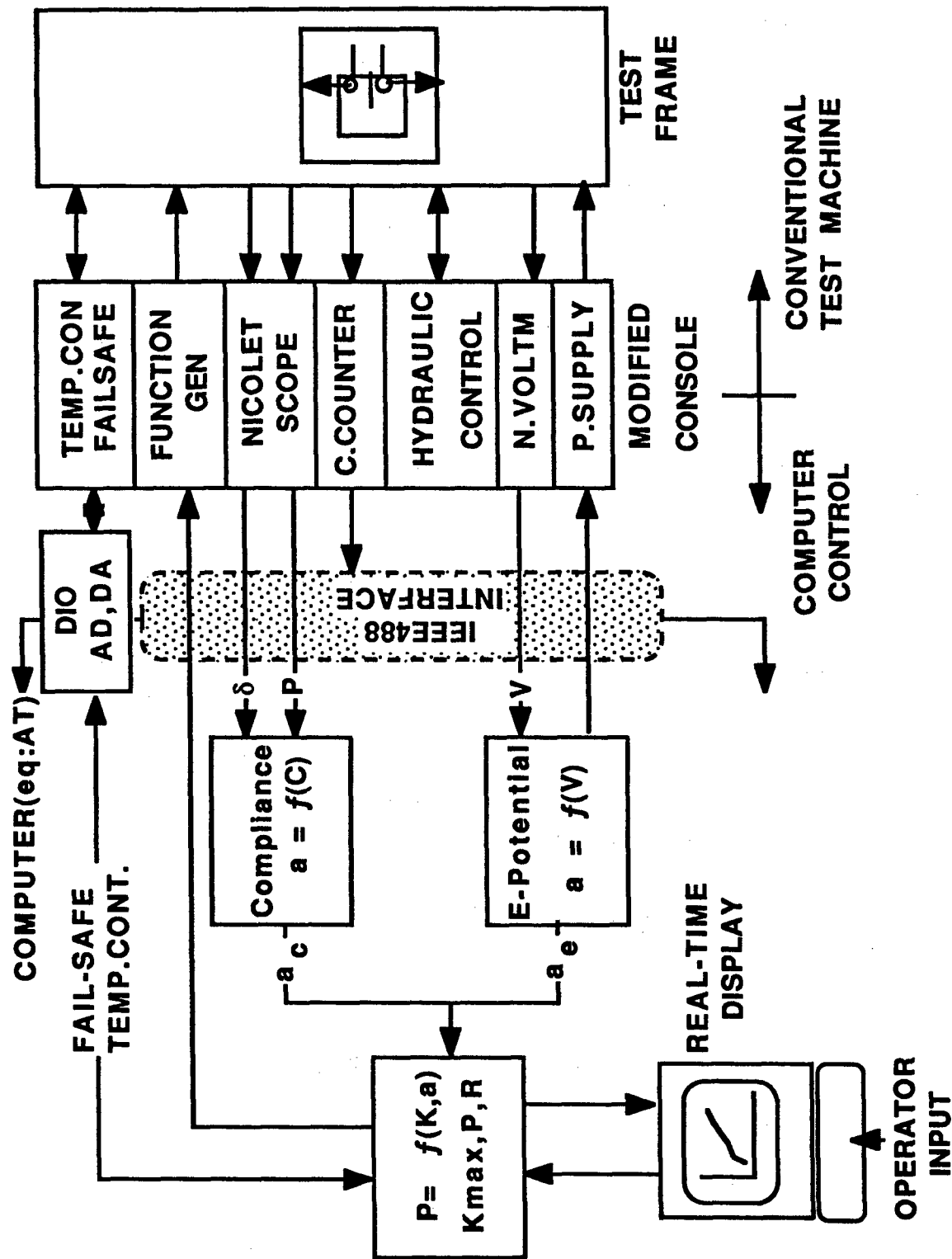


Figure A1. Block Diagram of the Automated Test Station.

- Eight Bit DIO Module - Can be used to switch on/off relays.
- Eight Channel A/D - Monitors the furnace temperature and status of the hydraulic machine. Monitoring of the cooling system will be added in the near future.
- Two Channel D/A Module - Provides set point information for the furnace controller unit.

A five channel multiport controller which uses switchable software is connected to the RS-232 port of the IBM AT computer. The software provides control of the following: (a) HOST PDP 11/24 - Data transfer, reduction, and report quality graphics, and mass storage, (b) Modem Connected to a Phone Line - CDC or home monitoring and control of long term tests, and (c) Terminal - Monitoring of tests from office or any other desired place in the laboratory.

In addition, the IBM AT is equipped with a high resolution 16 color EGA graphics monitor. High resolution color graphics display is used in monitoring real-time crack growth and growth rates graphically.

Software that has been developed is used for the following types of crack growth testing and modes of monitoring the tests:

- Decreasing stress intensity precracking (ASTM E399).
- Decreasing stress intensity threshold (exponential).
- Constant stress intensity testing.
- Constant load testing.
- Complicated waveform testing.
- Frequency shedding tests.
- Temperature shedding tests.

- Compliance and/or electric potential crack length monitoring based on the frequency condition.
- Test monitoring via phone/modem.
- Real-time data analysis and graphical display.
- Crack closure monitoring and display.
- Alarm shutdown.

## REFERENCES

1. Sharpe, W. N., Jr., "Interferometric Surface Strain Measurement," Int. Journal of Nondestructive Testing, Vol. 3, 1971, pp. 59-76.
2. Johnson, H. H., "Calibrating the Electric Potential Method for Studying Slow Crack Growth," Materials Research and Standards, Vol. 5, No. 9, 1965.
3. Quinn, G. D., "Guide to the Construction of a Simple 1500°C Test Furnace - II," Technical Note AMMRC TN 82-1, Ceramics Research Division, Army Materials and Mechanics Research Center, Watertown, Massachusetts, March 1982.
4. Ashbaugh, N. E., "Crack Length Expression as a Function of Compliance for Center-Crack Tension Specimen," ASTM Research Report RR-E24-1012, June 1986.
5. Weerasooriya, T. and Nicholas, T., "Hold-Time Effects in Elevated Temperature Fatigue Crack Propagation, AFWAL-TR-84-4184, Air Force Wright Aeronautical Laboratories, Wright-Patterson AFB, Ohio, March 1985.
6. Ashbaugh, N. E., Khobaib, M., Hartman, G. A., Weerasooriya, T., Rajendran, A. M., Maxwell, D. C., and Goodman, R. C., "Research on Mechanical Properties for Engine Life Prediction," AFWAL-TR-85-4154, Wright Aeronautical Laboratories, Air Force Materials Laboratory, Wright-Patterson Air Force Base, Ohio, May 1986.
7. Ashbaugh, N. E., "Effect of Load History and Specimen Geometry on Fatigue Crack Closure Measurements," Submitted for Review to ASTM STP of International Symposium on Fatigue Crack Closure, August 1986.
8. Jira, J. R., Weerasooriya, T., Nicholas, T., and Larsen, J. M., "Effects of Closure on the Fatigue Crack Growth of Small Surface Cracks in a High Strength Titanium Alloy," Presented at the International Conference on Closure, South Carolina, May 1986.
9. Pelloux, R. M., Faral, M., and McGee, W. M., Fatigue of Engineering Materials and Structures, Vol. 1, 1979, pp. 21-35.
10. Sunder, R. and Dash, P. K., Int. Journal of Fatigue 4, No. 2, April 1982, pp. 97-105.
11. Ashbaugh, N. E. and Goodman, R. C., "A Fatigue Evaluation of Hastalloy X Sheet Material," Technical Report UDR-TR-86-57, University of Dayton Research Institute, Dayton, Ohio, June 1986.

12. Weerasooriya, T. and Venkataraman, S., Proceedings of Effects of Load and Thermal Histories on Mechanical Behavior of Materials Symposium, TMS/AIME, Denver, Colorado, February 1987.
13. Nicholas, T. and Ashbaugh, N. E., "Fatigue Crack Growth at High Load Ratios in the Time-Dependent Regime," Submitted for Review to ASTM STP of Proceedings of the 19th National Symposium on Fracture Mechanics, September 1986.
14. Weerasooriya, T., "Effect of Frequency on Fatigue Crack Growth Rate of Inconel 718 at High Temperature," ASTM STP 969, American Society for Testing and Materials, Philadelphia, 1987.
15. Ashbaugh, N. E., "Time-Dependent and Cycle-Dependent Threshold Evaluation in a Nickel-Base Superalloy," Presented at the 18th National Symposium on Fracture Mechanics, Boulder, Colorado, 24-27 June 1985.
16. Weerasooriya, T. and Nicholas, T., "Overload Effects in Sustained Load Crack Growth in Inconel 718," ASTM STP 945, American Society for Testing and Materials, Philadelphia, 1987.
17. Weerasooriya, T. and Heil, M. L., "Micro-Mechanisms of Crack Growth Under Mechanical and Thermal Cycling in Inconel 718," Presentation Given at TMS/AIME Annual Meeting, Denver, Colorado, February 1987.
18. Venkataraman, S., Nicholas, T., and Khobaib, M., "An Investigation of Creep Crack Growth of Rene' N4 Advanced Ni-Base Superalloy," Presented at TMS/AIME Fall Meeting, Toronto, Canada, 13-17 October 1985.
19. Venkataraman, S., Nicholas, T., and Khobaib, M., "Creep and Fatigue Crack Growth Behavior of Single Crystal Rene' N4 Advanced Nickel-Base Superalloy," Presentation Given at TMS/AIME Fall Meeting, Toronto, Canada, October 1985.
20. Khobaib, M., Nicholas, T., and Venkataraman, S., "The Role of Environment in Elevated Temperature Crack Growth Behavior of Rene' N4 Single Crystal," Presentation Given at International Symposium on Environmentally Assisted Cracking, Bal Harbour, Florida, 8-13 November 1987.
21. Ashbaugh, N. E., Khobaib, M., Hartman, G. A., Weerasooriya, T., Maxwell, D. C., and Goodman, R. C., "Research on Mechanical Properties for Engine Life Prediction," AFWAL-TR-87-4011, Air Force Wright Aeronautical Laboratories, Air Force Materials Laboratory, Wright-Patterson AFB, Ohio, May 1987.

22. Balsone, S. J., Nicholas, T., and Khobaib, M., "The Effect of Stress on the Environmental Attack of Rene' 80," Presented at the TMS/AIME Fall Meeting, Orlando, Florida, October 1986.
23. Balsone, S. J., Khobaib, M., and Nicholas, T., "The Effects of Stress and Stress History on Environmental Attack in Rene' 80," Presentation Given at International Symposium on Environmentally Assisted Cracking, Bal Harbour, Florida, 8-13 November 1987.
24. Balsone, S. J. and Khobaib, M., "Hot Corrosion of Nickel-Base Superalloys," Presentation Given at AIAA Mini-Symposium, Air Force Institute of Technology, Wright-Patterson AFB, Ohio, 26 March 1986.
25. Ahmad, J., "Two Dimensional Linear Elastic Analysis of Fracture Specimens: User's Manual of a Finite Element Computer Program," AFWAL-TR-80-4008, Air Force Wright Aeronautical Laboratories, Wright-Patterson AFB, Ohio, February 1980.
26. Brockman, R. A., "SNAP: A Simple Nonlinear Analysis Program for Education and Research," UDR-TM-82-06, University of Dayton Research Institute, February 1982.
27. Smith, F. D. and Kullgren, T. K., "Theoretical and Experimental Analysis of Surface Crack Emanating from Fastener Holes," AFFDL-TR-76-104, Air Force Flight Dynamics Laboratory, Wright-Patterson AFB, Ohio, February 1977.
28. Bodner, S. R., "Representation of Time-Dependent Mechanical Behavior of Rene' 95 by Constitutive Equations," AFML-TR-79-4116, Air Force Materials Laboratory, Wright-Patterson AFB, Ohio, August 1979.
29. Enderle, P. R. and Ashbaugh, N. E., "Two Compliance Expressions for Arbitrary Locations Across a Crack in a CT Specimen," AFWAL-TR-85-4074, Air Force Wright Aeronautical Laboratories, Wright-Patterson AFB, Ohio, June 1985.